

A Review of Aeronautical Fatigue Investigations in Sweden During the Period May 2009 to March 2011



Edited by HANS ANSELL
Saab AB
Sweden

ICAF Doc. No. 2426
Saab Doc. No. TDL-2011-0091



SAAB



Statens haverikommission
Swedish Accident Investigation Board

swerea | SICOMP



CONTENTS

3.1	INTRODUCTION	3
3.2	INVESTIGATIONS ON OPERATIONAL EVENTS	4
3.2.1	Accident with a CASA C-212 aircraft during maritime patrol operation	4
3.2.2	Field experience - Saab 340 Bottom Panel STC antenna installation	7
3.2.3	Field experience - Saab 2000 Horizontal Stabiliser Corrosion Upper Spar cap	9
3.3	STRUCTURAL EVALUATION.....	11
3.3.1	The Saab 2000 Full Scale Fatigue Test and Damage tolerance Test - General.....	11
3.3.2	Wing/fuselage fatigue test.....	11
3.3.3	Saab 340 Tear Down Inspection.....	17
3.3.4	JAS39 Gripen Fatigue Testing.....	22
3.3.5	Tear down inspection of the single seater (Gripen A-version)	22
3.3.6	Full scale fatigue testing of the twin seater (Gripen D-version).....	24
3.3.7	Fatigue Life Verification of Gripen A/C Pylon #1	26
3.3.8	Fatigue Life Verification of Gripen A/C Swedish Standard Pylon #3	30
3.3.9	Fatigue and damage tolerance aspects of hybrid metal-composite wing structures.....	34
3.4	FATIGUE CRACK INITIATION AND PROPAGATION.....	38
3.4.1	A Computational Strategy for Multiple-Site Fatigue Analysis.....	38
3.4.2	Fatigue Crack Growth Model for Multiple Site Fatigue Damage Evaluation of Complex Structures.....	41
3.4.3	Verification of Calculated Stress Intensity Data for DB1-DB4.....	45
3.4.4	Validation of Multiple-site Fatigue Crack Growth Analysis Method	60
3.4.5	Multiple Site Fatigue Crack Growth Analysis of a few Sample Domains	65
3.4.6	Fatigue Modeling of Materials at High Temperature.....	70
3.4.7	Fatigue crack growth behaviour of Inconel 718 with high temperature hold times.....	73
3.5	COMPOSITE MATERIALS.....	77
3.5.1	Mechanical Testing of Battle-damaged Wing Boxes.....	77
3.5.2	Shear Test of Impact Damaged Composite	80
3.5.3	More effective composite structures through improved sizing methodology	81
3.5.4	Residual stresses and 3D failure criteria for NCF-materials.....	82
3.6	NDT TECHNOLOGY.....	84
3.6.1	Evaluation of Nonlinear Ultrasonics for early detection of fatigue damage and structural degradation in aerospace structure.....	84
3.7	SERVICE LOADS MONITORING	88
3.7.1	Service life monitoring of Gripen weapon pylons	88
	REFERENCES	90
	ACKNOWLEDGEMENTS	91

3.1 INTRODUCTION

In this paper a review is given of the work carried out in Sweden in the area of aeronautical fatigue and structural integrity during the period May 2009 to March 2011. The review includes basic studies and industrial applications of fatigue development in metals and composites, stress analysis and fracture mechanics, studies of crack initiation and propagation and residual strength, service loads monitoring, testing of full-scale structures, non destructive inspection techniques and fatigue life predictions. A reference list of relevant papers issued during the period covered by the review is included.

Contributions to the present review are from the following bodies:

- The Swedish Defence Research Agency (FOI)
Sections 3.4.1, 3.4.2, 3.4.3, 3.4.4, 3.4.5, 3.4.6, 3.5.1, 3.5.2
- SAAB AB
Sections 3.2.2, 3.2.3, 3.3.1, 3.3.2, 3.3.3, 3.3.4, 3.3.5, 3.3.6, 3.3.7, 3.3.8, 3.3.9, 3.5.1, 3.5.2, 3.7.1
- Exova AB
Sections 3.6.1
- The Swedish Accident Investigation Board (SHK)
Sections 3.2.1
- Swerea SICOMP
Sections 3.5.3, 3.5.4
- Linköping University (LiU)
Sections 3.4.7

3.2 INVESTIGATIONS ON OPERATIONAL EVENTS

3.2.1 Accident with a CASA C-212 aircraft during maritime patrol operation

One of the Swedish Coastguard aircraft, of type CASA C-212 with call sign KBV 585, took off 26 October 2006 at 11:09 from Ronneby airport for a routine maritime surveillance flight. The crew consisted of two pilots and two system operators.

During the flight the crew received a message from the co-ordination centre concerning a request that had been received for a fly by over the Falsterbo canal, where the Swedish Coastguard has a base. The pilots accepted this and revised the final part of their flight plan so that a demonstration of the aircraft could be performed.

At 13:23 KBV 585 came in over the coast at Falsterbonäset on a north-northwesterly course along the canal. The aircraft then continued out over the sea and after a left turn returned to approach the base. The aircraft then performed another fly by at low speed over the base and along the canal in the opposite direction. Beyond the end of the canal the aircraft turned back to the left and flew for the last time towards the base.

As the aircraft neared the base once more it made some wing tipping. After tipping its wings two or three times a loud bang was heard and the entire left wing separated from the aircraft. The aircraft then rolled over on to its back and fell, along with the left wing, into the harbour basin, where it disintegrated on impact. All on board were killed.



Figure 1. CASA-212-CE aircraft in maritime patrol operation

At the time of the accident, the aircraft had accumulated 17,000 flight hours and 7,300 flight cycles. A full investigation, conducted by the Swedish Accident Investigation Board, was immediately initiated.

After initial examination of the evidences, cracks, suspected to be caused by fatigue, were found in the centre wing lower skin at STA Y=1030. The lower wing skin at this station has an external doubler riveted to wing skin consisting of 6 rivet rows. The cracks were confined to the first rivet row in the skin where the external doubler ends. The cracking was wide spread extending over a large portion of the wing chord, figure 2. Cracks were also found in the same area of the right hand side wing. Information regarding the investigation work has also been reported in previous Swedish ICAF reviews [1, 2].

The development of the fatigue crack along rivet row # 1, that finally led to the wing fracture, can be described in five phases:

Phase I A great number (thousands) of micro-cracks, less than 50 microns deep, developed in the Alclad layer.

Phase II Some hundreds of those micro-cracks grew as fatigue cracks into macro-cracks.

Phase III A number of macro-cracks coalesced into continuous fatigue cracks that penetrated the lower wing skin.

Phase IV In a zipper opening effect the joining of the continuous crack with individual fatigue cracks created a major crack along the rivet row. Along the same row fatigue cracks of different size were developed on all the longerons.

Phase V When the major fatigue crack had reach a length of about 840 mm the wing ruptured. Figure 2.

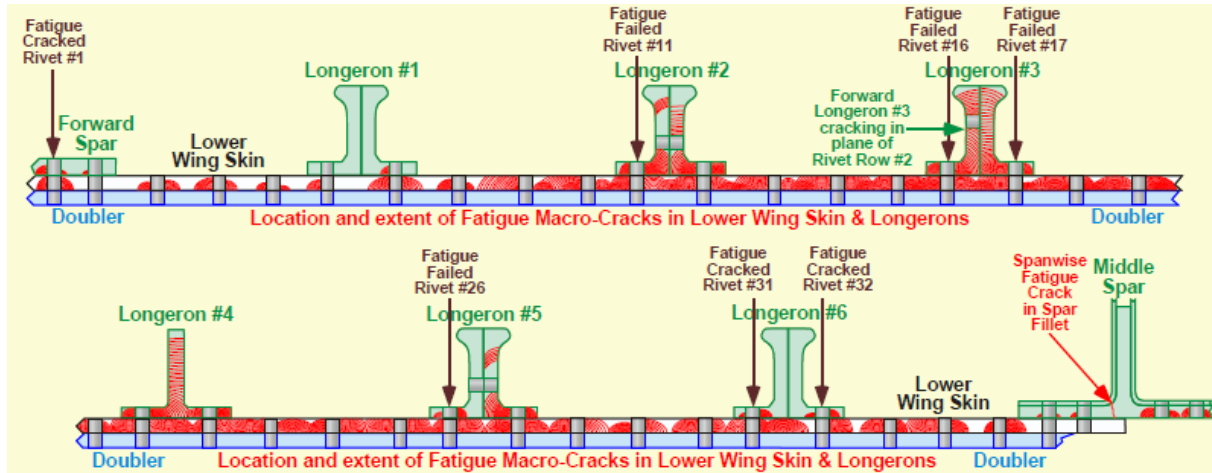


Figure 2 Schematic fatigue crack pattern in the left wing skin at STA Y=1030.

The cracks initiated both from the edges of the rivet holes and from microcracks in the underside of the skin along the rivet rows # 1.

In a band that extends about 4 mm inside to 12 mm outside the centre line of the rivet row, hundreds of micro-cracks were found on the underside of the skin. Some of these were only 0.1 mm deep and 1 mm long, and could not be seen by the bare eye or with any of the usual NDT methods. Such cracks only become apparent during visual inspection with magnifying glass (x 10) or when the sheet is bent.



Figure 3. Example of micro-cracks in the finishing and SEM photo of crack surface

The investigation of the cause of the accident has now been closed and the final report been released by the Swedish Accident Investigation Board regarding the probable cause of the accident, [3]. The following summary of findings and conclusion is reported:

- The technical examination showed that the cause of the wing separation was a fatigue fracture, about 84 cm long, which was present in the wing lower skin, where the wing was attached to the aircraft fuselage. The crack in the wing lower skin, which forms part of the wing's load-bearing structure, meant that the strength of the wing was severely compromised.
- In connection with the wing tipping that was performed, momentary lift and mass forces were applied to the wing, which resulted in a final fracture in the left wing that bent upwards and separated from the aircraft fuselage.
- The same type of fatigue crack was found in a similar location in the right wing, but this was far less developed. The initiation and development of these left and right wing cracks were similar. The metallurgical examination showed that they had been initiated at an early stage, and that the fatigue cracks had grown for a long time without having been detected. The location of the cracks under doublers meant that they were not visible from the outside of the wing.
- SHK considers that the design of the wing attachment to the aircraft fuselage was unsuitable, since the fairings between the aircraft fuselage and wing can transmit vertical loads for which they are not intended. The design means that a considerable proportion of such loads can, in certain circumstances, be transferred to the lower wing skin in a band at right angles to the primary load path of the skin.
- The characteristics of the fatigue cracks that in the left wing resulted in wing separation are typical of Multiple Site Damage.
- The fatigue cracks could have come about as the result of residual stress in the wing lower skin, that could have existed since the wing was manufactured or that arose due to some momentary overload while in service. Nothing in the investigation indicates so, although this possibility cannot be excluded.
- SHK considers, however, that it is more likely that the fatigue cracks arose during normal flight operations in combination with some form of additional vibration and/or oscillating loads at some period of time in the history of the accident aircraft. The damage sequence had progressed over a long time, and some form of combination of the above factors cannot be excluded.
- It is the assessment of SHK that the manufacturer underestimated the material stress and the risk of crack formation in that particular area, and thereby overestimated the fatigue strength of the wings.
- The maintenance system that the manufacturer has prepared for this type of aircraft, and that SHK understands was complied by the maintenance organisation, was not able to detect and prescribe relevant measures to prevent the growth of these particular fatigue cracks.
- Nor did the manufacturer utilise the possibility of using the accident aircraft, which was the operating time leader in respect of coastguard flying operations, for crack growth inspection, as a sample, with the intention of identifying possibly critical areas concerning fatigue cracks.
- After this accident, the manufacturer and authorities prescribed special inspections of the affected areas in the wings, in respect of fatigue cracks. About 1/3 of the aircraft of this type in service have so far been reported as inspected, without finding any similar cracks.
- The operations of the Swedish Coastguard have sometimes subjected the flight equipment to high loads, but the operations have, in the opinion of SHK, taken place within the permitted limits for this type of aircraft.
- The demonstration flight along the Falsterbo canal took place with a deviation from the applicable internal rules and without operational instructions.

The accident was caused by an inadequate maintenance system in respect of inspections for fatigue cracks. Contributory to the crack formation has been an unsuitable design of the attachment of the wings to the aircraft fuselage.

3.2.2 Field experience - Saab 340 Bottom Panel STC antenna installation

Field experiences have revealed that some Saab 340 aircraft have cracking issues in the bottom fuselage panels due to improper installation of antenna devices.

The retroactive antenna modification originates from a world wide STC (Supplemental Type Certificate) design of antenna installation. It should be pointed that that this is not design or approved design from the original manufacturer.

Consequently, figure 4 details the area of fuselage hull subjected to the cracking, in the bottom panel where the antenna provisions have been installed

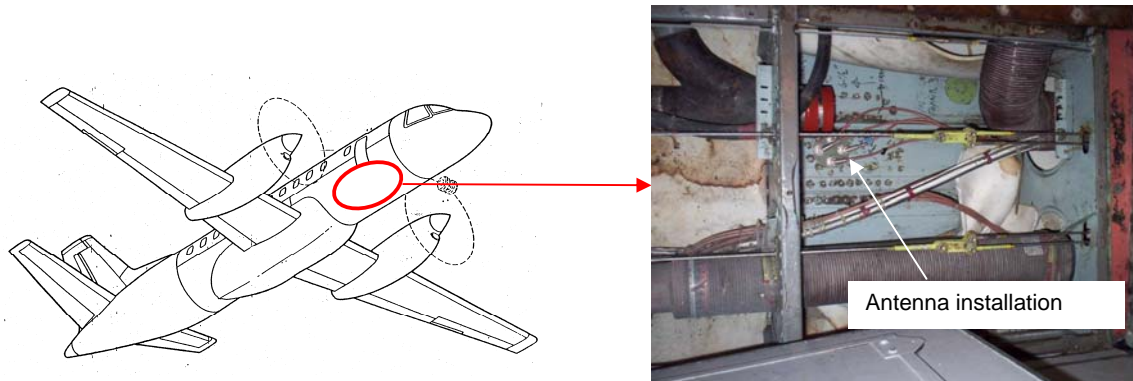


Figure 4. Location of the area subjected to cracking

During a scheduled inspection severe longitudinal cracking was discovered in the bottom panel as outlined figure 5. Severe cracking in terms of multiple cracks and cracks measuring 6-7 inches was detected in the panels. In addition to this, environmental degradation such as corrosion was discovered in the area of the antenna installation. The skin panels and the structural provisions for the antenna were afflicted with severe corrosion.

The Saab 340 aircraft has adopted the damage tolerance concept according to regulations FAR/FAR 25.571. Primary structural elements such pressurized hulls have been subjected to damage tolerance analysis and test verifying the overall requirements. Subsequent MSG-3 analyses have resulted in an inspection program to cover all significant load carrying structural members.

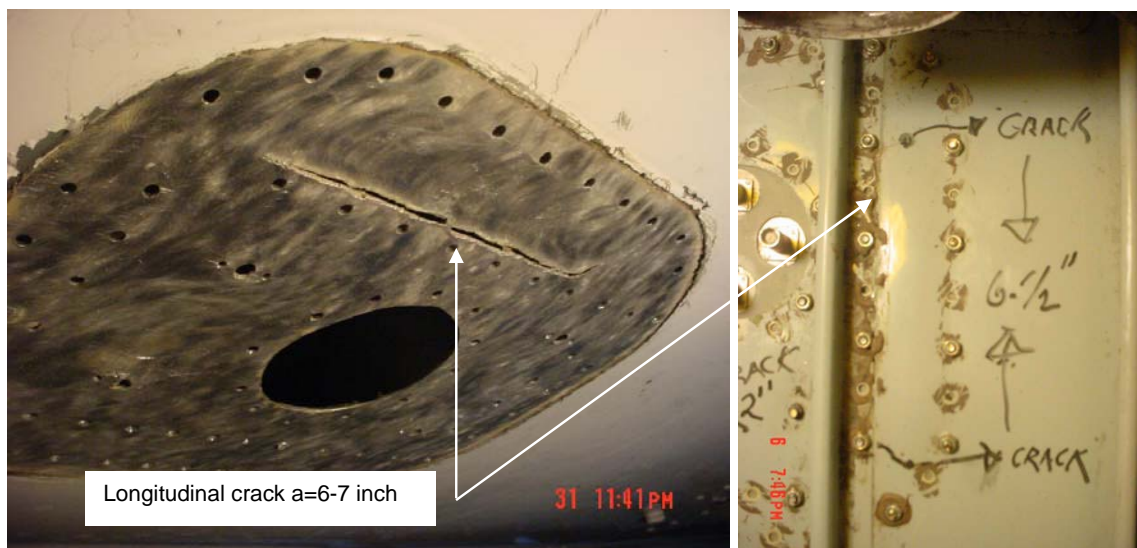


Figure 5. Longitudinal cracking of the fuselage panel.

A comprehensive investigation was carried out to find the cause for the cracking and possible consequences for the aircraft having this Supplemental Type Certificate design implemented.

From the justification of the long term characteristics it is concluded that the observed cracking is not promptly critical for the continuing airworthiness. Detailed damage tolerance analysis supported by test confirms the rationale that the detected cracks are less severe than the certification results from analysis and tests. Having reviewed it is concluded that the following results are valid for longitudinal crack considering hard points or splices.

Longitudinal Crack

Crack Growth Life $T_{crit} > 2,500,000$ Flights

Critical Crack Length $A_{crit} \geq 500$ mm

The complete crack growth curve is attached as figure 6.

Primary structural elements such as circumferential /longitudinal fuselage splices, has subjected to full scale testing up to limit load level. Figure 7 depicts a typical and successful test of the residual strength capability considering artificial cracks.

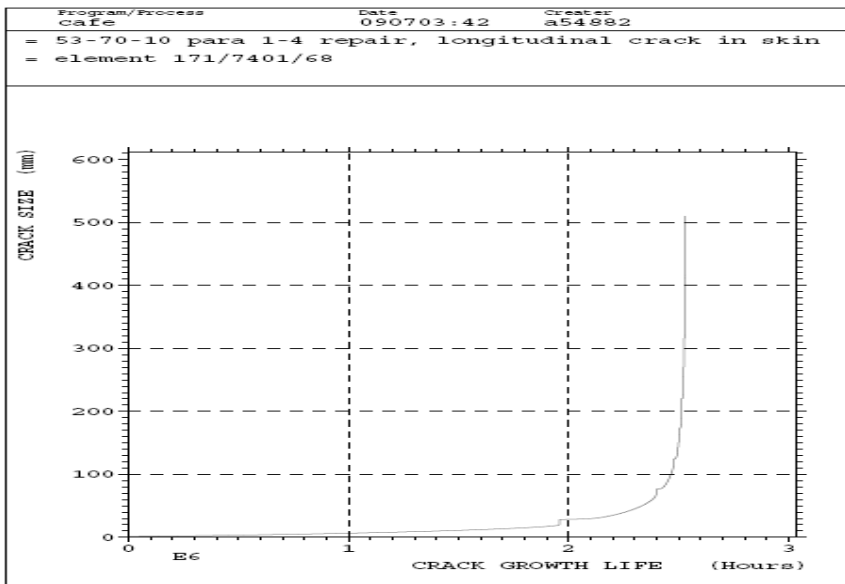


Figure 6. Crack growth curve – longitudinal crack considering hard point/splices

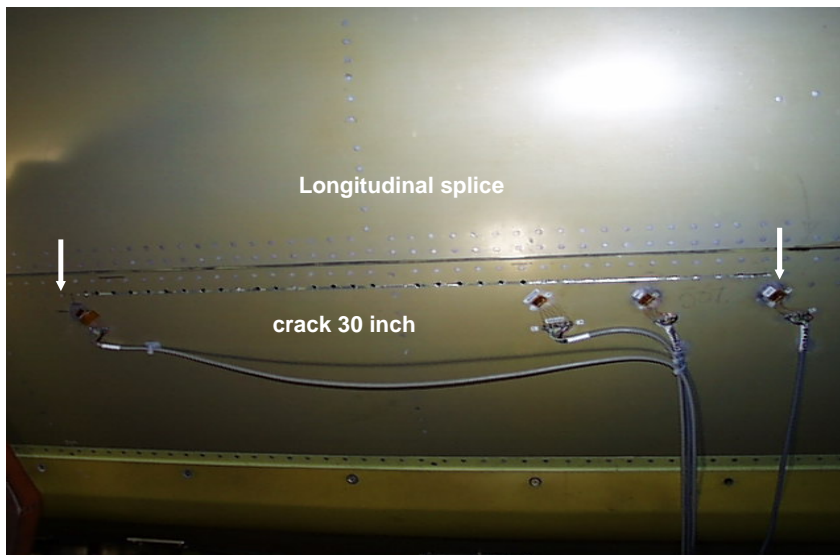


Figure 7. Saab 340 Fuselage- Residual Strength test of longitudinal splice

On the basis of the aforementioned investigation and rationale it is concluded that the antenna installation do not follow general procedures for mounting antennas in pressure hull. There are several uncertainties regarding the installation of the antenna causing compromised long term characteristics:

- Severe hardpoint (i.e large portion of load transfer) between antenna baseplate and fuselage skin
- Anchor nuts installed directly in the skin without any anchor nut plates
- Acceptance of improper edge distances
- Compromised surface protection on skin and modification items
- Improper structural reinforcement

However, using the results from the damage tolerance concept it is deemed that there is no directly unsafe condition operating the aircraft. Grace periods or deferrals are acceptable in order to define inspections and corrective actions. This is carried out by releasing Airworthiness Directives from the authorities covering the aircraft with subject antenna STC implemented.

3.2.3 Field experience - Saab 2000 Horizontal Stabiliser Corrosion Upper Spar cap

Corrosion to structural members may be regarded as crack initiation points and subsequent cracking may occur as a result of this defect. Therefore it is required inspect aircraft structure with respect to corrosion and other environmental degradation. At one occasion, it was experienced that the Saab 2000 aircraft was confined to have corrosion to the upper spar cap of the horizontal stabilizer as detailed figure 8.

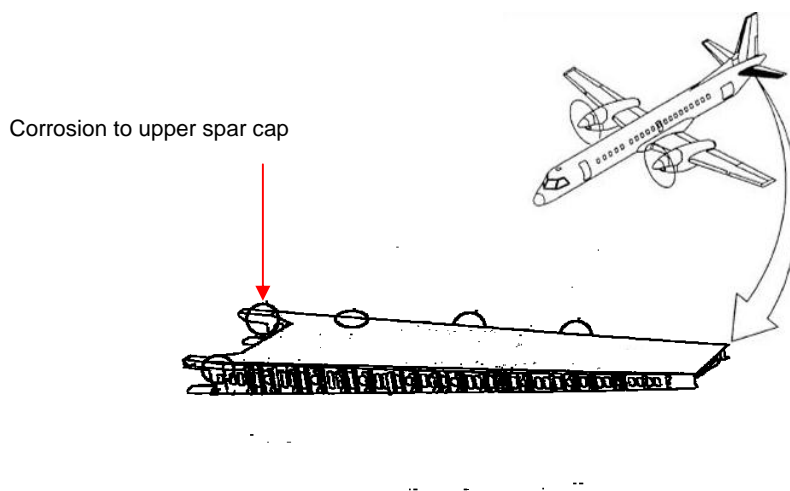


Figure 8. Saab 2000 Horizontal Stabilizer-Location of corrosion to upper rear spar cap

The corrosion is classified as severe exfoliation as shown in figure 9. The corrosion is caused by interference between the aluminium spar cap and electrical harness to the elevator control system. Galvanic corrosion to aluminium results in quick degradation of structural elements as shown.



Figure 9. Saab 2000 Horizontal Stabilizer-Location of corrosion to upper rear spar cap

The upper rear spar cap is designated as principal structural element implying that damage tolerance philosophy has been used to fulfil the requirements according to FAR/JAR 25.571. Detailed analysis followed by tests has been used to justify the structural capability in terms of crack growth and residual strength.

The results from analysis is given by figure 10 and 11, from the results it is concluded that the analysis is conservative compared to what was revealed during the test. Subsequently, the residual strength test with broken spar cap element sustained the criteria to withstand the most extreme limit load condition.

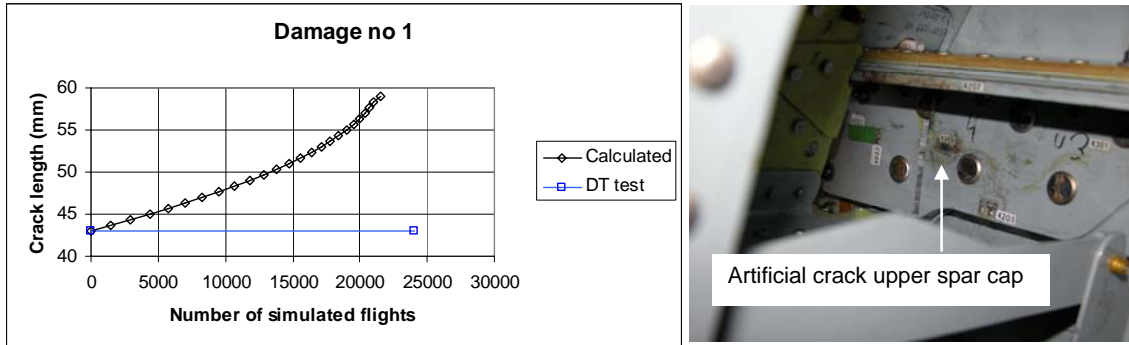


Figure 10. Saab 2000 Horizontal Stabilizer-Damage Tolerance analysis versus test result

Tested In FSFT → 24000 FI –No propagation

Tested In FSFT → Residual Strength Test OK 178%LL

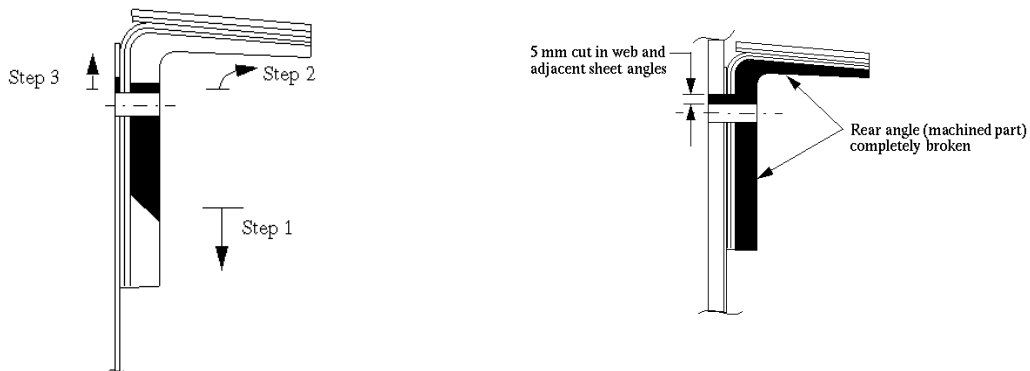


Figure 11. Saab 2000 Horizontal Stabilizer-Damage Tolerance test

The aforementioned data has been used to validate the severity of the corrosion issue. From The justification above concludes the fact that damage tolerance concept is applicable to address the severity of in-service related problem such as the corrosion. Mandatory service bulletins calling out inspections and terminating actions has been released allowing some deferrals. Hence, the aircraft operators may have the opportunity to plan for the necessary actions without any grounded aircraft.

3.3 STRUCTURAL EVALUATION

3.3.1 The Saab 2000 Full Scale Fatigue Test and Damage tolerance Test - General

The Design Service Goal (DSG) for Saab 2000 is presently 75000 flights or 60000 flight hours whichever occurs first. For the Saab 2000, no complete airframe will be tested due to the commonality with the Saab 340. Consequently, a number of full scale component tests are used to justify the long term characteristics.

3.3.2 Wing/fuselage fatigue test

The subject test includes the centre and the rear part of the fuselage, the complete wing torque box and the rear part of the engine nacelles.



Figure 12. Saab 2000 Wing/Fuselage Fatigue and damage tolerance test

The wing detail design is changed compared to the Saab 340 (machined spars with integral spar caps), and the wing/fuselage interface also. Furthermore the cabin pressurisation spectrum is more severe, more exactly twice as severe as the spectra for the Saab 340 aircraft. The flight and landing loads on the fuselage is also more severe due to the slender fuselage of Saab 2000.

The first part of Wing/Fuselage Fatigue test up to 150000 flights with fatigue loads is finalised. The second part, the damage tolerance testing has been completed in terms of testing up to reach 2*24000 flights with artificial notches. Twenty six different types of damages have been introduced reflecting the damage tolerance characteristics of various principal structural elements of the Saab 2000 airframe. The third and the last part of testing include testing for verification of the residual strength capability of the airframe. Major artificial cracks representing critical crack length are embodied and subsequently tested for the most critical limit load condition. This part of the test is ongoing.

In conformity with other tests, the wing/fuselage structure has been tested to demonstrate the damage tolerance characteristics in accordance with airworthiness requirements specified in FAA/EASA regulations. This also includes residual strength tests up to limit load condition for selected and critical load cases.

The test sequence used in the damage tolerance phase is the identical to sequence used in the fatigue phase. Thus, this sequence is truncated in terms of reduction of load cycles with small ranges. For damage tolerance testing is also crucial to consider load cycles with small amplitudes or ranges due to the contribution to the total crack propagation. Instead of using a revised test sequence it has been verified that the existing sequence can be adapted with the addition of more test cycles to the previous defined test sequence.

Since a limited no of damages shall represent damage tolerance characteristics of all critical parts, a careful selection has been carried out.

The criteria for selecting which damages to test have been:

- Damages with impact on flight safety
- Damages with short calculated total crack growth life
- Damages in fail safe structure, for which the calculated crack growth life after failure of one load path is short
- Damages for which it is desirable to improve the in-service inspections

The selected damages cover different types of structural parts, such as wing panels, wing spars, fuselage panels, reinforced fuselage cut-outs, wing and fuselage splices. They also cover different types of crack origins, such as for example free edges, open holes and holes with pin load.

Figure 13a and b on the following pages summarizes the location the artificial cracks introduced on the Saab 2000 airframe. Figure 14 (damage 19) outlines an artificial crack in the forward lower spar cap including a similar damage to the outer wing skin. Figure 15 (damage 16) outlines an example of introduced artificial cracks on the lower wing panel, the internal located stringer is also simulated to be broken (through cutting of the entire stringer)

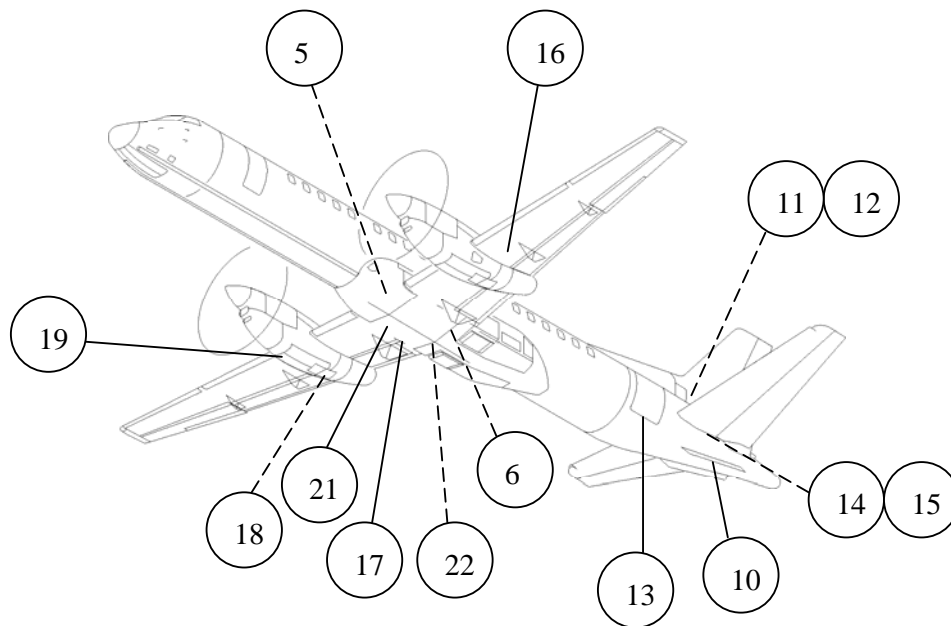


Figure 13a. Saab 2000 Overview of artificial cracks in test article

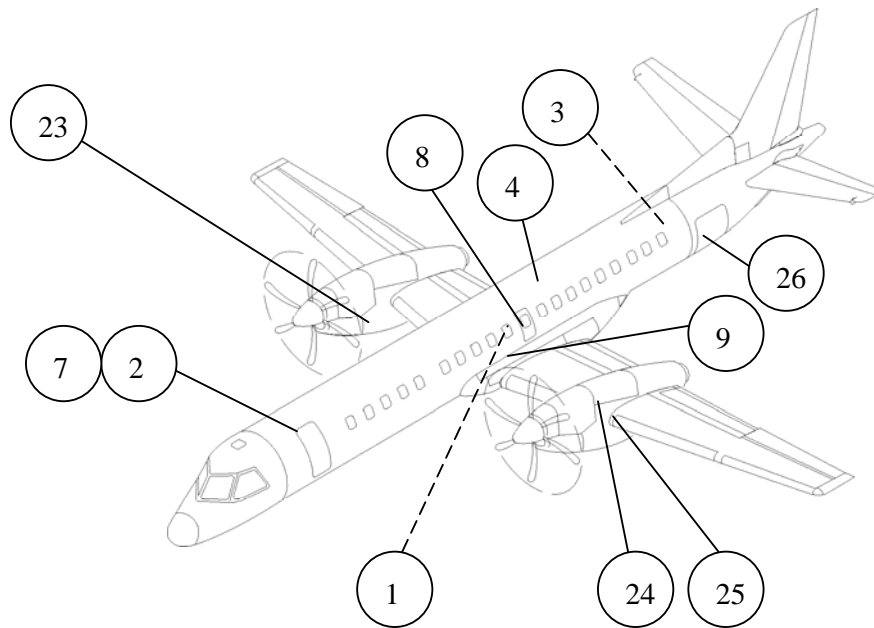


Figure 13b. Saab 2000 Overview of artificial cracks in test article



Figure 14. Saab 2000 Artificial crack in lower forward wing spar cap and in skin

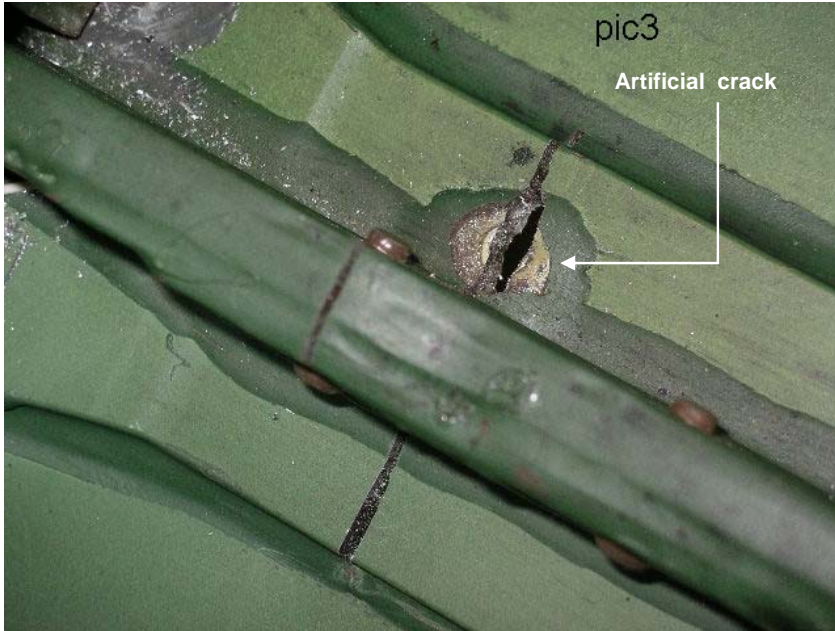


Figure 15. Saab 2000 Artificial crack in lower wing skin with an broken stringer

In general, it is observed that it is hard have a natural crack growth from an artificial damage. Theoretical crack growth analysis appears to be afflicted some conservatism. Analytical damage tolerance models are mostly limited in geometry and redistribution of internal loading to adjacent members are not always considered. Consequently, analytical prediction using classical fracture mechanics is deemed to be slightly conservative compared to the results obtained from full scale damage tolerance testing.

However, the artificial crack in the lower wing skin in figure 16 and 17 (damage 16) has been propagated towards the adjacent stringers and crack arrest has been noted at the bonded stringers. The initial crack was 55 mm including a broken stringer, the crack has been propagated 280 mm under 48000 flights of testing. The two-bay crack philosophy has thereby been verified for a predefined inspection interval. By comparison the results from the analysis and the test (see figure 18) it is concluded for this specific artificial damage that the crack growth rate in the theoretical analysis is slightly slower than the observed characteristics from the test article.

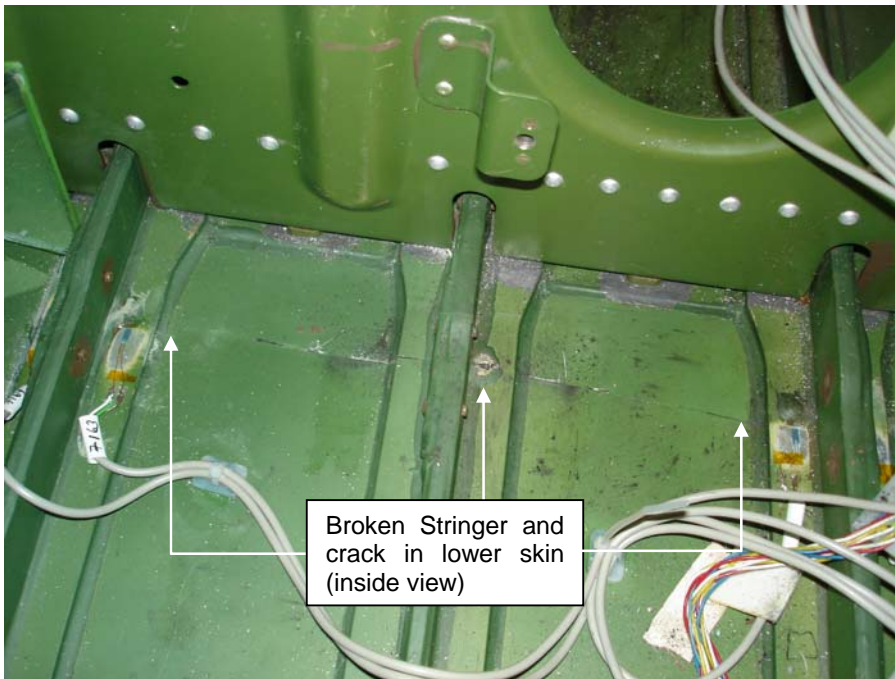


Figure 16. Saab 2000 Artificial crack in lower wing skin and stringer -inside view

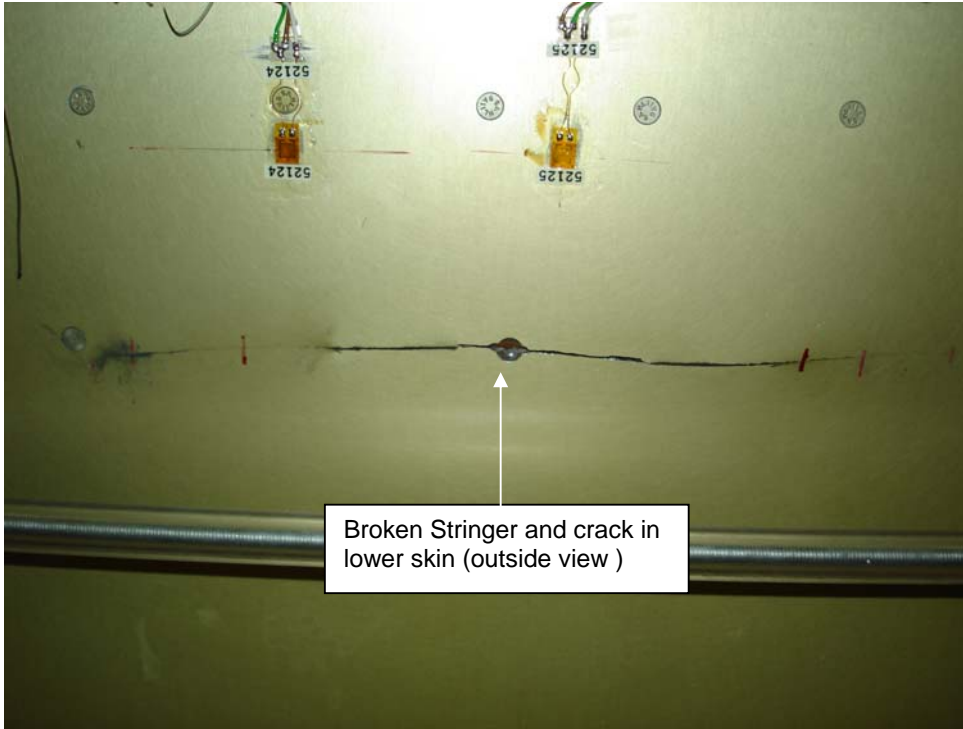


Figure 17. Saab 2000 Artificial crack in lower wing skin and stringer -outside view

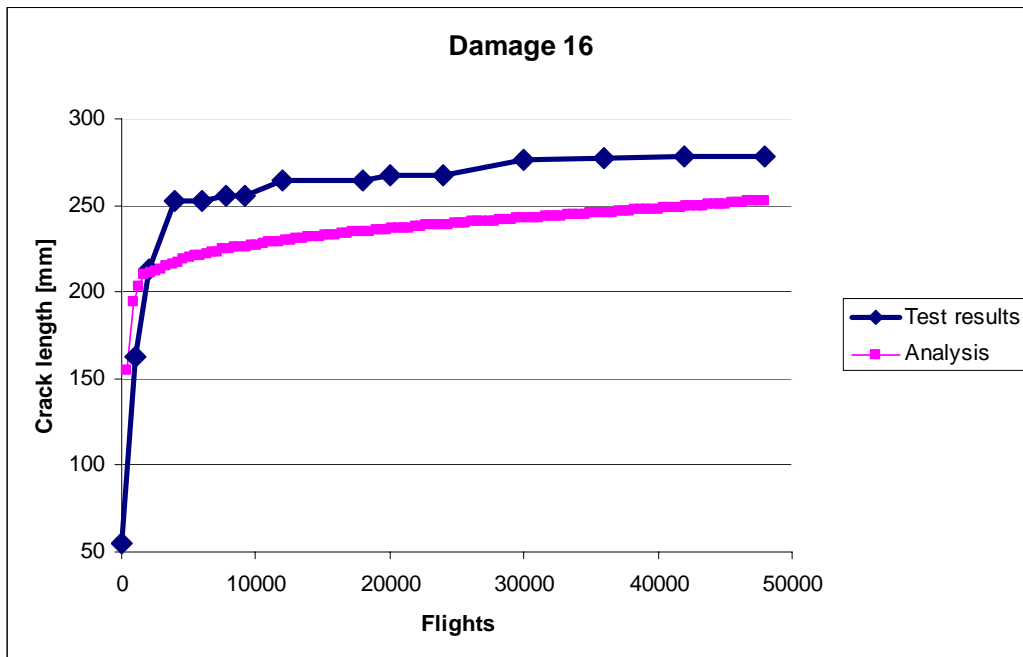


Figure 18. Saab 2000 Artificial crack in lower wing skin and stringer comparison of results

As was mentioned previously, the static residual strength test program has been commenced implying that the entire airframe will be tested covering approximately 20 static limit load cases in order to verify the structure for predetermined critical crack length conditions. Primary structural elements such as circumferential /longitudinal fuselage splices, wing spars and pressure decks will accordingly be subjected to the most critical load case up to limit load level.

Figure 19 to 21 outlines some examples of the location and nature of the artificial cracks in pressurized structural members exposed to the residual strength test.

The following figure, figure 19 details the artificial crack for the residual test of the mid fuselage pressure deck, the saw cut is approximately 560 mm.

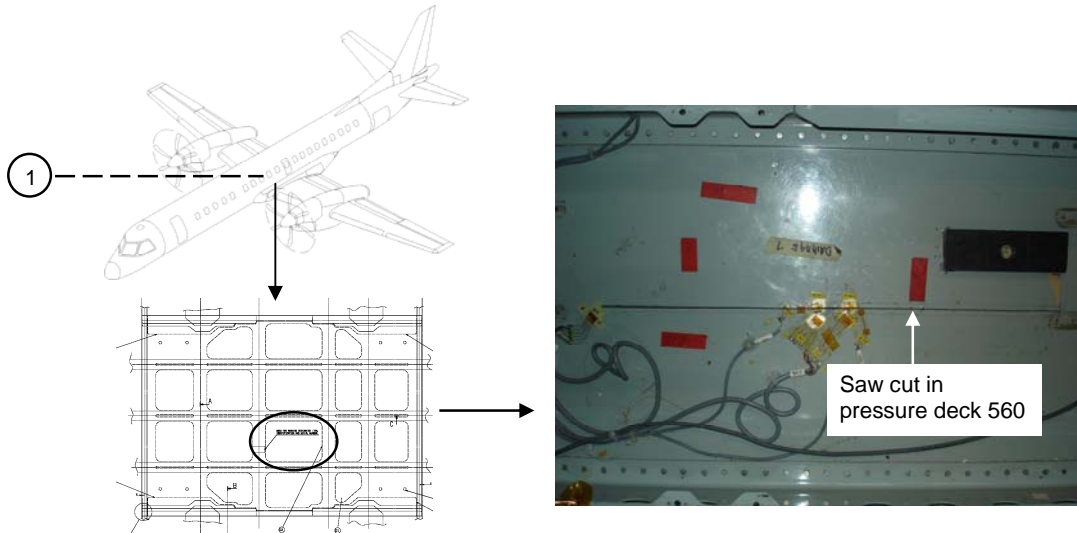


Figure 19. Saab 2000 Artificial crack (saw cut) for testing the residual strength capability in the mid pressure deck

The aft pressure bulkhead will also be subjected to residual strength testing with an associated artificial crack as shown in figure 20. The stiffener including the bulkhead has been provided with artificial of 570 mm.

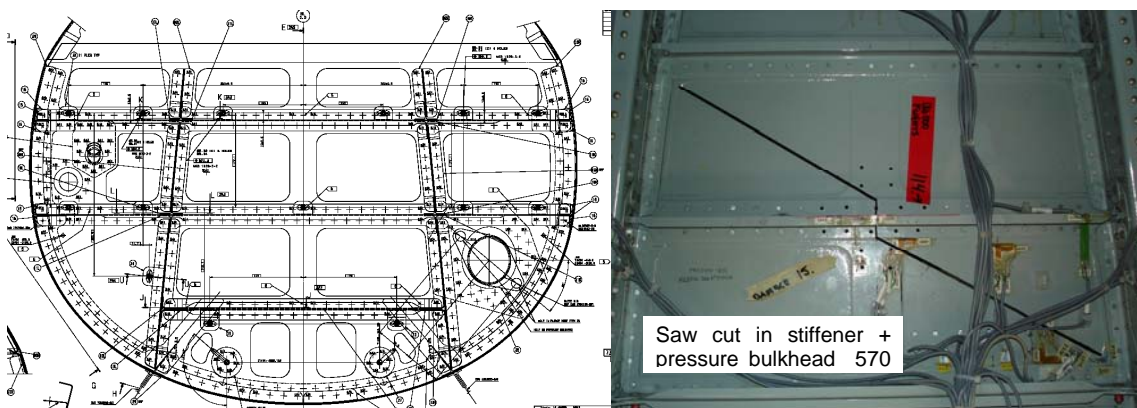


Figure 20. Saab 2000 Artificial crack (saw cut) for testing the residual strength capability in the aft pressure bulkhead

The rear wing spar and the adjacent lower skin will be subjected to residual strength test where the major portion of the rear wing spar and the lower wing skin has been inflicted with saw cuts. This test is carried out in order to verify the wing structure can withstand all limit load condition considering a major damage to the primary structural elements. Figure 10 provides the prerequisites for the testing.

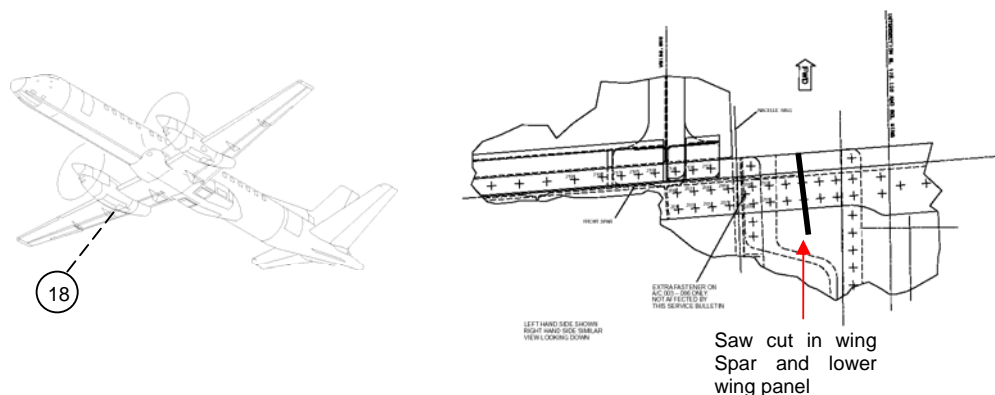


Figure 21. Saab 2000 Artificial crack (saw cut) for testing the residual strength capability of wing spar and skin structure

3.3.3 Saab 340 Tear Down Inspection

After completion of the full-scale fatigue and damage tolerance testing a tear down inspection was carried out on some significant primary structural elements. The test article has been subjected to fatigue testing/damage tolerance testing of 204000 flights.

The aim with this tear down inspection is to full fill the airworthiness requirement and to investigate possible crack propagation not visually detectable or detectable with non destructive inspection methods on a complete airframe.

The following notes represent a list of structural items which have been subjected to some tear down inspection procedure.

- Horizontal Stabilizer – Interface to the fuselage frames – Attachment holes
- Empennage frames horizontal stabilizers attachment holes
- Cargo door cut out in fuselage skin – Bonded laminated multi layer parts
- Longitudinal Splices
- Front and rear wing spar lower part of web and lower spar cap
- Wing attachment frame
- Wing/fuselage links, fittings and bolts
- Wing center splice
- Forward Pressure bulkhead –structural members
- Mid fuselage pressure bulkhead , significant structural items
- Windshield and side window attachment lugs

Cargo door cut out in fuselage skin

The subject is characterised by a high a stressed area, and this structure in this corner consists of outer skin and multi layer reinforcement doublers. The area was also subjected to damage tolerance testing g with an artificial crack in the corner.

Figure 22 details the corner and a dedicated area for the tear down inspection and the following figure (figure 23a, b and c) shows the dismantled parts with some extended cracking in the embedded layers. However, they were detected on the airframe using X-ray equipment in which part was difficult to conclude. Part 1 and Part 2 were revealed to have some extended cracking due fatigue loading.

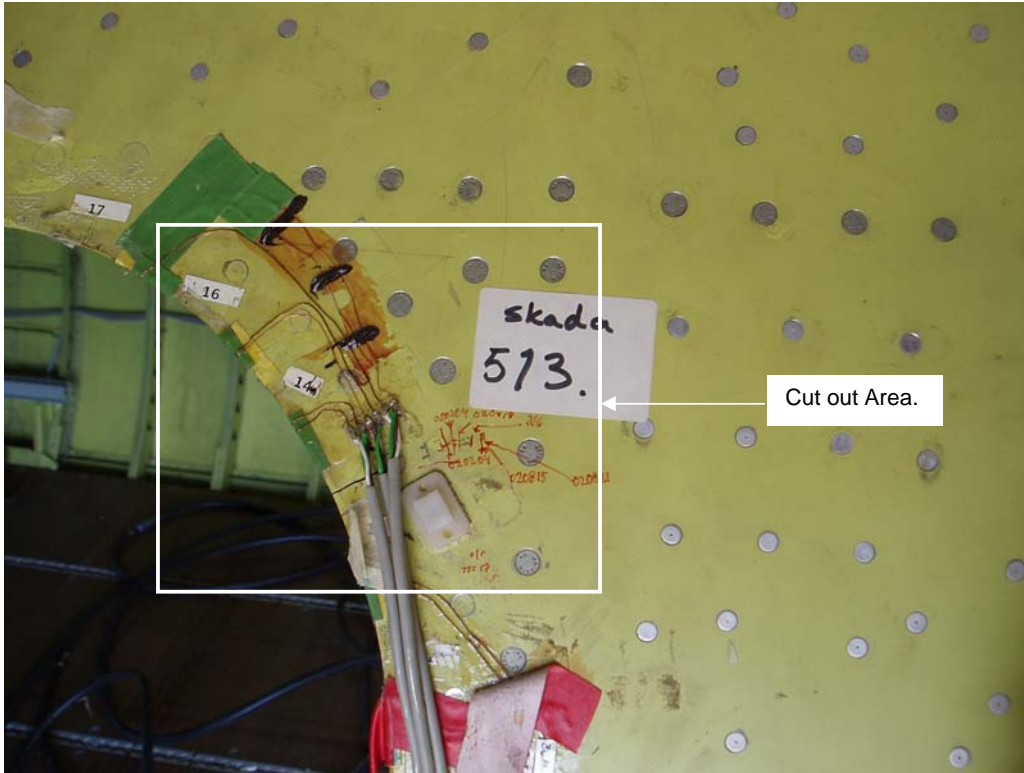


Figure 22. Cargo door cut out in fuselage skin with area subjected to tear down inspection

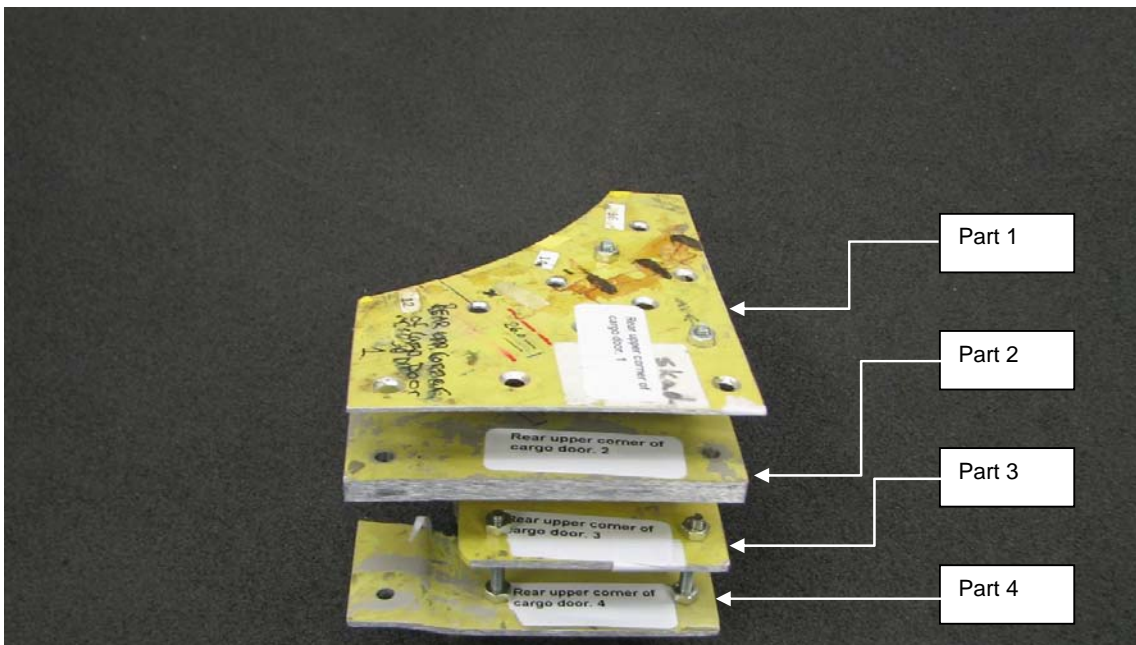


Figure 23a. Parts 1-4 of rear upper corner of cargo door



Figure 23b. Part 1 of rear upper corner of cargo door



Figure 23c Parts 2 of rear upper corner of cargo door

Longitudinal splices in the fuselage skin

Some local longitudinal splices were disassembled and the structural members were inspected using NDT (Eddy Current and Penetrant Inspection) Once the presence of a crack had been established, the size of the crack was measured visually and using microscope.

Figure 24 gives a typical longitudinal splice part subjected to tear down inspection. At some local and few places there were crack indications and subsequent measuring reported surface crack lengths between 0.1 mm to 2 mm. The residual strength test carried out in final phase was successfully and the small indications do not compromise the overall structural integrity of the splices.

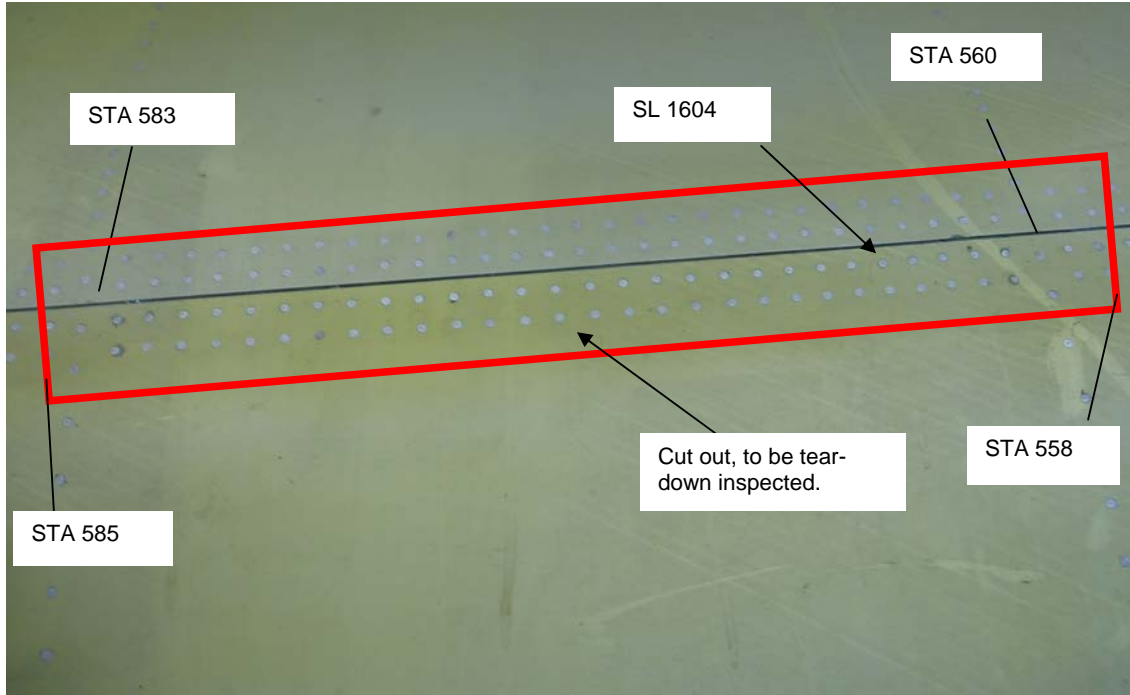


Figure 24. Longitudinal Splicet between top and side panel

Wing attachment frames

The primary wing attachment frames have been subjected to damage tolerance testing. Small notches were introduced in these high stressed frames in order to verify the crack growth characteristics, see figure 25 for the frame design and the location of the notch. After the damage tolerance testing no visual or NDT detected cracks were present at the notch.

However, a comprehensive microscope inspection was carried out within the tear down inspection program and the results indicated that a very minor crack propagation was noticed from the notch.

Examination of the produced fracture surface showed that there was a thin fatigue zone along the bottom of the artificial crack, this according to figure 26.

The fatigue zone was deepest, approx. 0.05-0.06 mm, in the middle between the ends of the artificial crack. Towards the ends of the artificial crack the fatigue zone faded out to almost no depth.

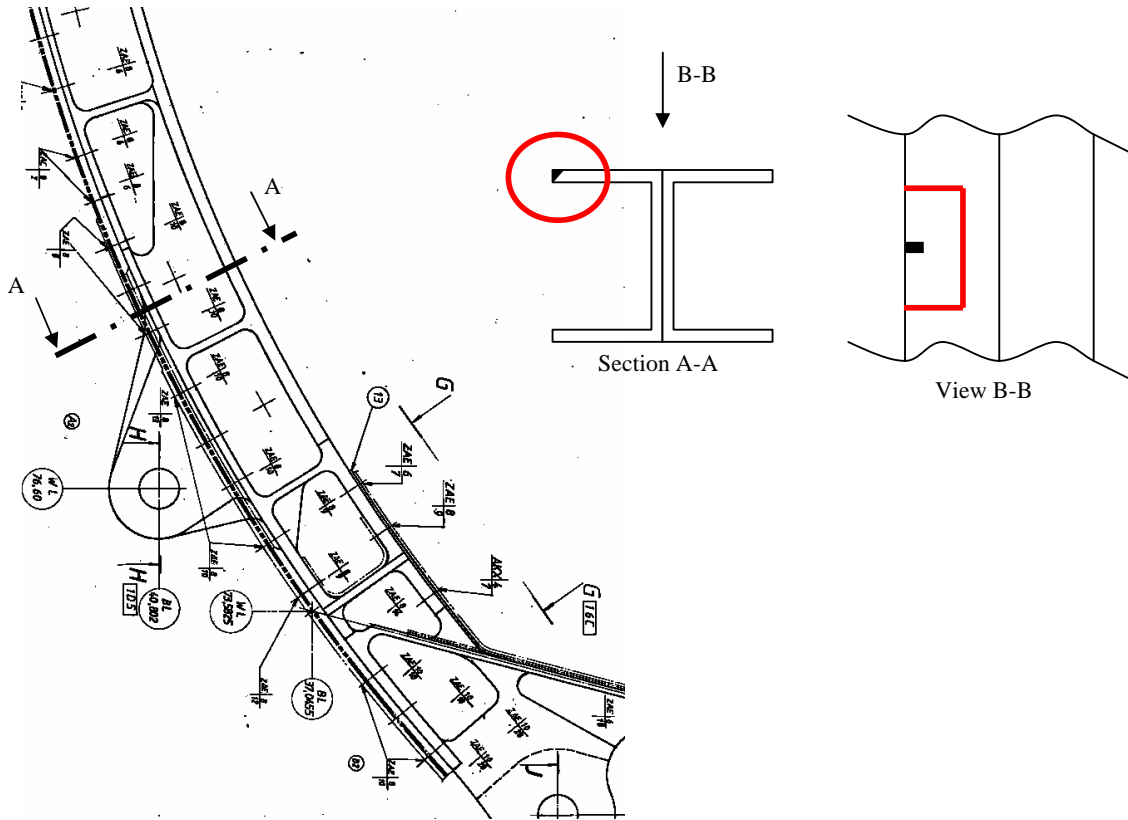


Figure 25. Wing attachment frame

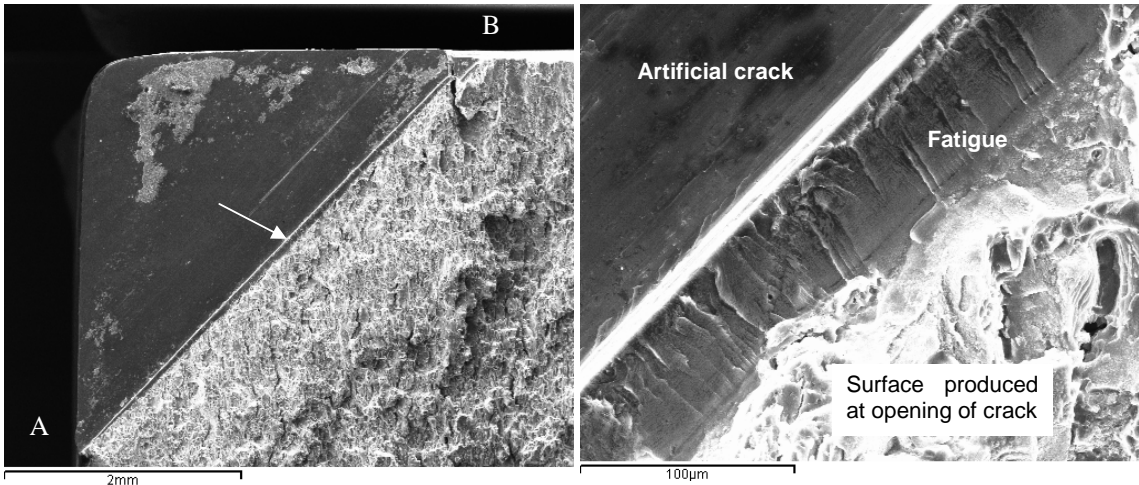


Figure 26. Fracture surface after opening of artificial crack. Dark marked zone is fatigue.

3.3.4 JAS39 Gripen Fatigue Testing

The strength verification programme with large components was completed during 1994. The full scale fatigue test of the twin seater, 39B, was completed in 2000. The full scale fatigue test of the single seater, 39A, was tested much further in order to verify an extended life of the wing and fin of the C/D versions and was completed in 2007. The full scale fatigue test of a twin seater export version, 39D was completed 2008.

3.3.5 Tear down inspection of the single seater (Gripen A-version)

Details about the test and results found during testing to 32,000 flight hours and additional testing of weapon pylon attachment areas can be found in previous Swedish ICAF reviews [1, 2].

During fall 2010 the tear-down inspection has been started. The main focus is on wing and fin structure since these parts are essentially the same as on C and D versions of the aircraft. Selected primary parts on the fuselage, which are similar for the A and C version, will also be included in the tear-down inspection.

Before the disassembly took place, the test article was used for additional testing of the wing mounted weapon pylon stations. The aim of the testing was to pave-the-way for the airframe for extended flight time with external stores and for future integration of new weapons presently not known, [2].

In figure 27 is the fuselage shown after removal of certain main structure such as wings and fin. The fuselage is inspected for fatigue cracks in this position before specific parts are disassembled for detail laboratory inspections.



Figure 27. The full-scale fatigue test article(A-version) after partly disassembly.

The tear down inspection has just recently started and only a very few cracks have been found during the inspections before disassembly. Cracks have been found in:

- In the fin attachment frames in an area close to where the attachment bolts are mounted.
- In the fitting attaching the servo actuator for the canard wing to the fuselage

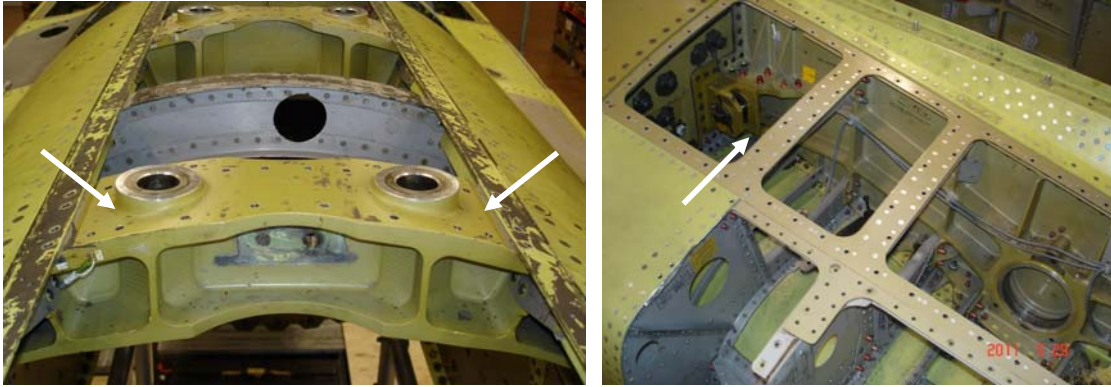


Figure 28. Cracks in fin attachment frame Figure 29. Crack in the actuator fitting for the canard wing

The tear down inspection will continue during 2011. The disassembled parts of the fuselage will undergo detail laboratory inspections. The wing with carbon composite skin are disassembled before a general ultra sonic inspection is done with additional inspections of local areas depending on discovered defects. After disassembly, inspections of inner structure will continue. In figure 30 is as an example the inner structure of the wing and some selected parts that will be further disambled and examined shown. Already disassembled are the wing attachment fittings and bolts which presently are under detailed examination. The fin with carbon composite skin is ultra sonic inspected completely and additionally inspected in local areas where defects are indicated.

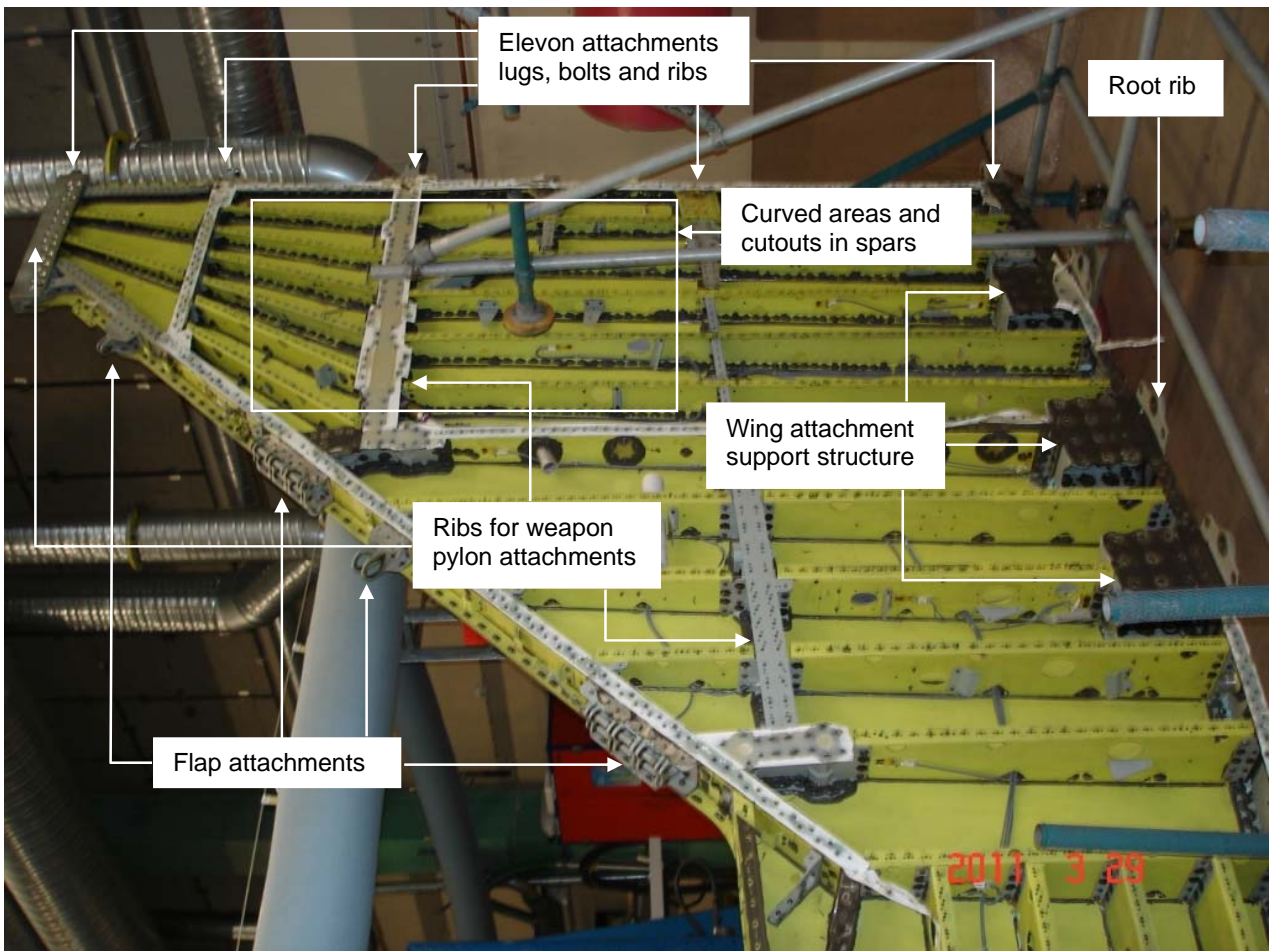


Figure 30. Examples of parts in the wing to be inspected and examined in detail.

No more information about findings are in hand at this moment but will be reported in coming Swedish reviews.

3.3.6 Full scale fatigue testing of the twin seater (Gripen D-version)

The test object is a complete fuselage. Attachment loads from the wings, fin, foreplanes, landing gears etc. are applied via dummies. The fatigue testing was started in January 2004 and reached the target life 32,000 hours in December 2008. Major inspections were done at 8,000, 16,000, 24,000 and 32,000 hours. No fatigue cracks have been found in primary structure but a very few have occurred in secondary structure. Details about the test, testing aims and crack findings can be found in previous Swedish ICAF review [1, 2].

During 2012 the tear-down inspection will start. Before the disassembly takes place, the test article is presently used for additional testing in order to pave-the-way for more service life for certain parts. Additional testing has been completed for the attachments for the fuselage mounted weapon pylons 4 and 5. Next to be tested is the attachments for the main and nose landing gear in order to verify extended life for roll-over of emergency landing wires. In figure 31 are the hydraulic jacks for introducing loads in the main landing gears shown (and partly jacks for weapon pylon 5). In figure 32 is the hydraulic jacks for introducing loads in the nose landing gear.

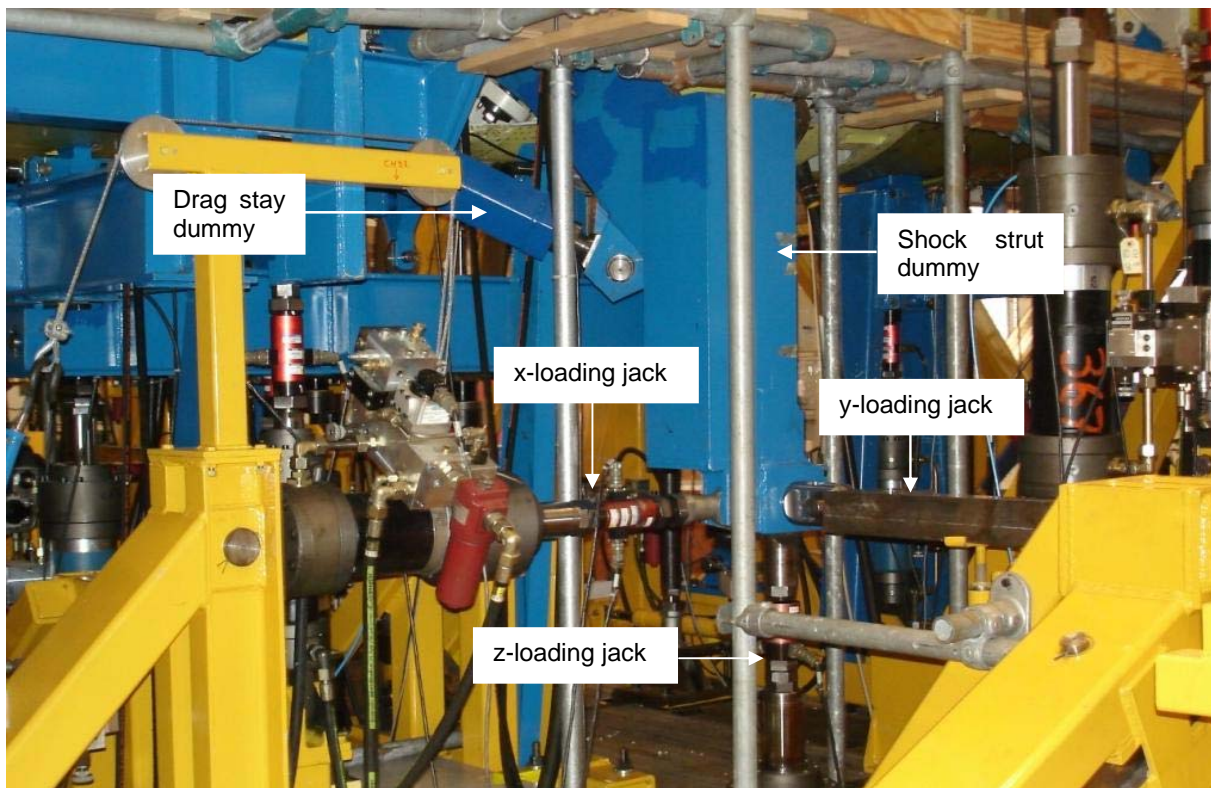


Figure 31. Photo showing hydraulic jacks and load introducing devices for the main landing gear.

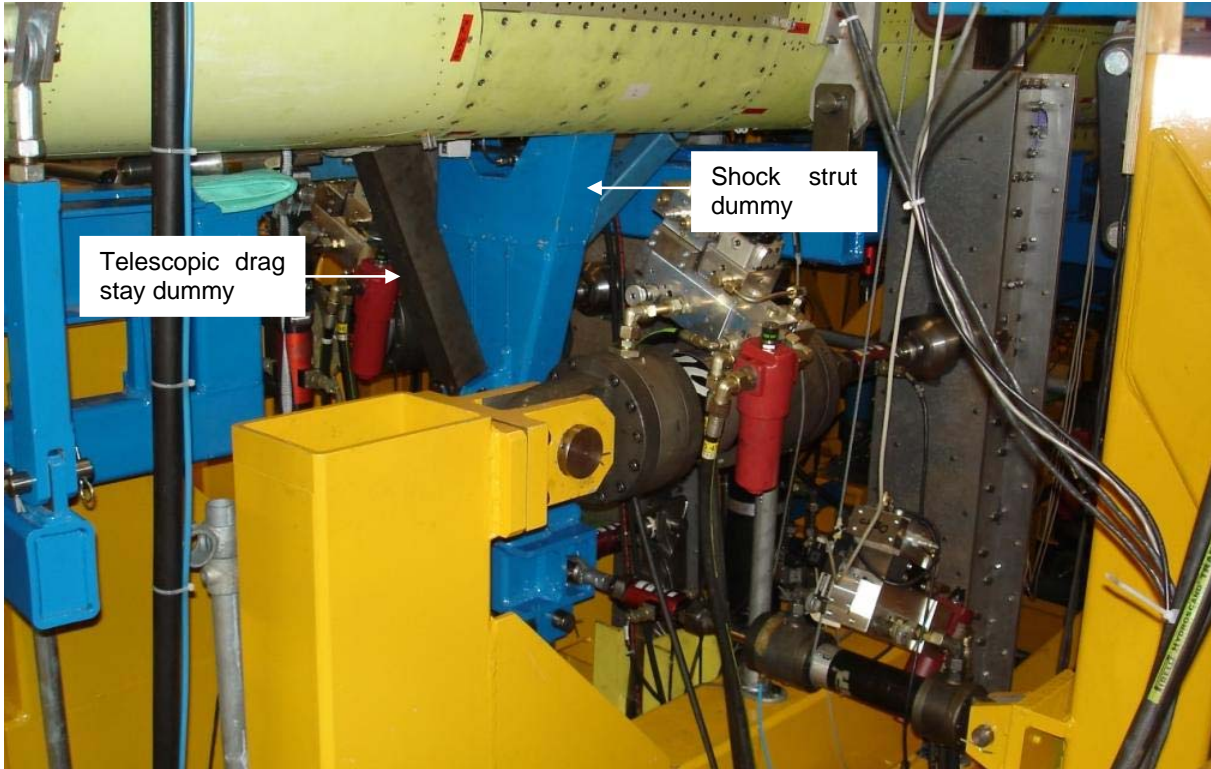


Figure 32. Photo showing hydraulic jacks and load introducing devices for the nose landing gear

After the additional testing of the landing gears shall the structure supporting the air-to-air refueling probe be further tested in order to pave-the-way and verify for more refueling operations. The dummy for introducing air-to-air refueling loads is shown in figure 33.



Figure 33. Photograph of the of the forward fuselage with the air-to-air refuelling probe dummy.

3.3.7 Fatigue Life Verification of Gripen A/C Pylon #1

Weapon pylon #1 on the Gripen A/C is an IR-missile rail launcher, figure 34, mounted to the wing tip spar with three bolts and two shear pins.



Figure 34. Pylon #1 with IR-missile.

The pylon center section is an aluminum alloy extrusion with a hollow cross section and with an outboard wall rail profile, figure 35. End housings, wing tip units, are fitted to both ends of the centre section via bolted joints. Besides electronics, the hollow centre section contains a missile locking mechanism.

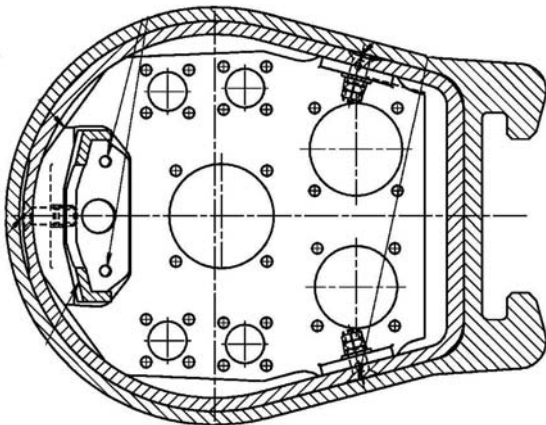


Figure 35. Pylon #1 cross section.

Missile to pylon loads are transferred to the pylon rail by three T-shaped missile hangers. The forward hanger transfers axial-, side- and vertical forces and roll moments to the pylon rail and locking mechanism, the mid hanger transfer vertical forces to the pylon rail and the aft hanger transfers side- and vertical forces and roll moments to the pylon rail.

Previous pylon #1 fatigue life verification was performed, through test, using a load sequence corresponding to a now outdated user profile. Following fatigue verification the test specimen was used in a static strength verification test.

With an updated user profile the aim is to, by fatigue test, verify the potential of pylon #1 with focus on missile carriage flight hours.

Test setup

The test is aiming on verification of the pylon #1 primary load paths at the forward and aft hanger areas. Mid hanger is not considered due to low load levels and similarity with aft hanger area. The pylon to wing joint is correctly loaded throughout the test.

The test rig, figure 36, consists of a pylon #1 test specimen bolted to a backing structure. To stabilize the loading of the forward and aft missile hangers a simple missile dummy was used connecting the hangers, see figure 37.

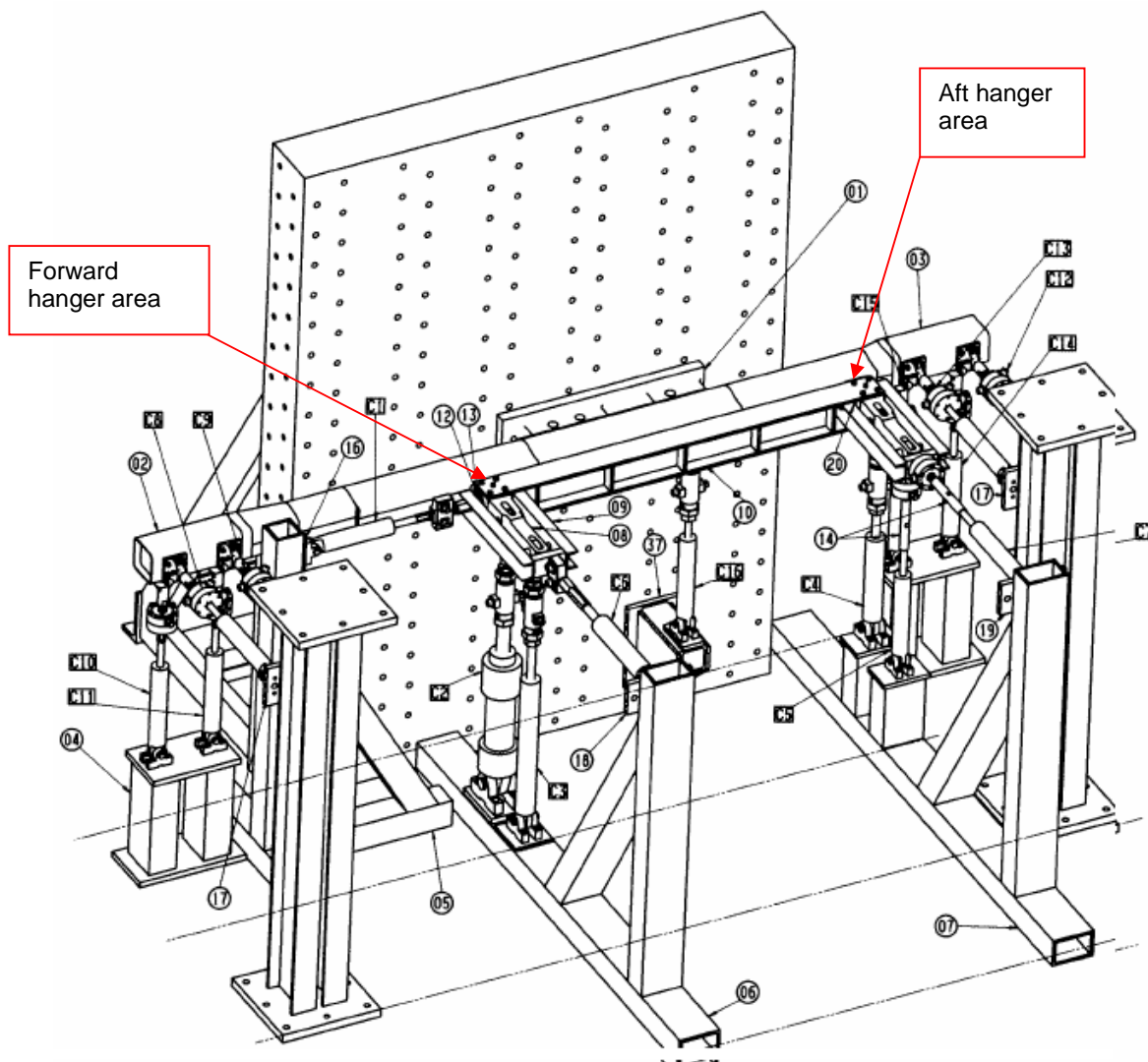


Figure 36. Test rig arrangement.

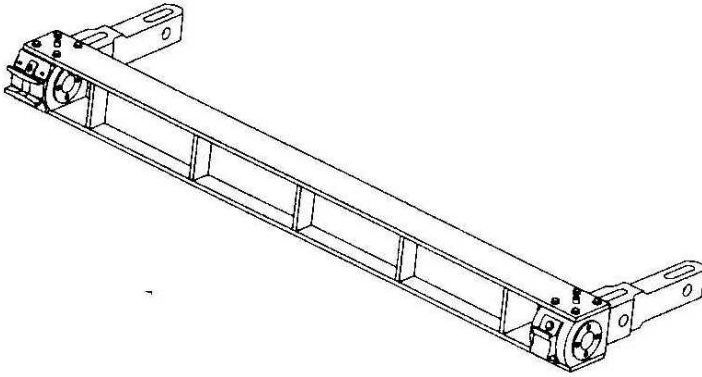


Figure 37. Missile dummy connecting forward and aft hanger.

The basic rig setup uses 16 load actuators with load cells where four channels are used for loading the forward hanger and three for the aft hanger. Wing tip units to centre section joint is loaded by four actuators each. Correct roll moment in the pylon to wing joint is controlled by a single vertical actuator.

The initial testing comprised of two test specimens #1 and #2 followed by an additional test specimen #3. All test specimens have been taken from A/C in-service.

The vertical position of the hanger in the rail was controlled by shimming, figure 38. For test specimen #1 and #3 a more severe position was chosen compared to test specimen #2.

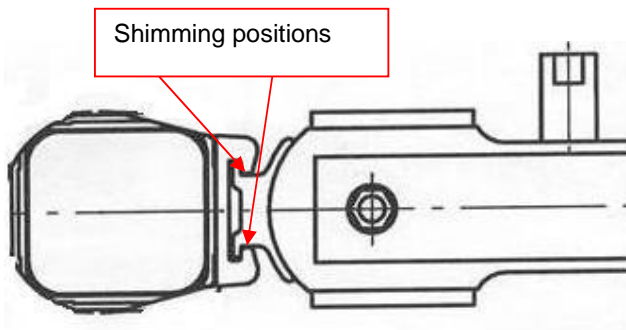


Figure 38. Hanger vertical position in rail controlled by shimming.

Test procedure

The test load sequence, used for test specimen #1 and #2 consists of missions with pylon #1 missile carriage corresponding to the updated user profile.

Revision of the method used to consider buffeting loads resulted in a mitigation of the test load sequence, hence an additional test using test specimen #3 was performed to confirm the gain in fatigue life compared to the more severe buffeting loads in load sequence used for test specimen #1 and #2.

The test load sequence is repeated during testing. NDT-inspection (Eddy Current) was scheduled at specific simulated flight hours.

Test results Centre section – forward hanger area

Test specimen #1 - indicated a crack of length 42 mm and depth 1 mm after 9 LSR (Load Sequence Repetitions). At 21 LSR the crack length was 61 mm and depth >1 mm (NDT limitation reached), failure followed directly at loading after 21 LSR. See figure 39.

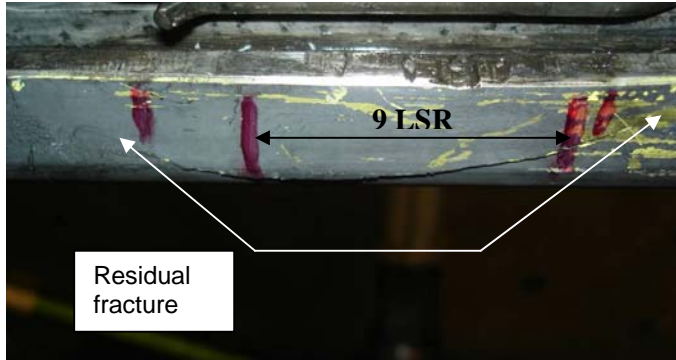
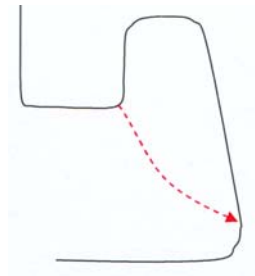


Figure 39. Test specimen #1 crack length after 9 LSR and final residual fracture.

Post test DT results gave:

- The fatigue crack had a length of 51 mm at the rail radius and a depth of 7.5 mm. Crack angle was 45 degrees from radius and outboard – downwards, see figure.



- The fatigue had several starting points initiated along the rail radius. Most of the starting points were due to pitting corrosion.
- The crack surface, figure 40, was inspected for periodicity in beach marks without success.



Figure 40. Test specimen #1 fracture surface.

Test specimen #2 - indicated a crack length of 36 mm and depth >1 mm after 16 LSR.

The testing was terminated and followed by a residual strength test which met the 150 % limit load requirement.

Post test DT results gave:

- The fatigue crack had a length of 35 mm at the rail radius and a depth of 2.8 mm. Crack angle (45 deg) and shape was the same as for test specimen #1.
- The fatigue crack had several starting points initiated along the rail radius. Most of the starting points were due to pitting corrosion.
- It is confirmed that the corrosion is not caused by fretting between hanger and rail but by pitting.

Test specimen #3 (revised load sequence) - indicated a crack length of 18 mm and depth 0.2 mm after 48 LSR. At 96 LSR the crack length was 42 mm and depth > 1mm. The testing was terminated and followed by a residual strength test which met the 150 % limit load requirement.

Post test DT results gave:

- The fatigue crack had a length of 42 mm at the rail radius and a depth of 4.5 mm. Crack angle (45 deg) and shape was the same as for test specimen #1.
- The fatigue crack had several starting points initiated along the rail radius. Most of the starting points were due to pitting corrosion although shallower compared to test specimen #1.
- The crack surface was inspected for periodicity in beach marks without success.

Test results Centre section – aft hanger area

The test results of the aft hanger area are consistent with the results of the forward hanger area although with a lower degree of cracking due to the lower load levels in this area. Hence the forward hanger area is the more critical point of the pylon.

Test results other areas

Other areas verified, although not as critical as the forward hanger area, are

- Wing tip unit to center section joints.
- Missile locking mechanism.
- Pylon to wing joint bolts.

Conclusion

Verified allowable flight hours for the pylon #1 structure are set by the forward hanger area. The verified allowable flight hours are finally based on the test specimen #3 results, tested with the mitigated load sequence. The verified allowable flight hours are determined by evaluation of the test by

- a safe life approach applying a fatigue test scatter factor of 4 on the tested flight hours, here in combination with the residual strength test which met the 150 % limit load requirement.
- the safe life results of the evaluation can also be supported by a damage tolerance approach applying a scatter factor of 2 on the tested flight hours showing stable crack growth together with the residual strength test.

One outcome of the testing is that it has been observed that all three of the test specimens are affected by corrosion. The interaction between corrosion damage and the initiation points of the fatigue cracks is confirmed by the testing, although the influence on the fatigue life is not quantified. The presence of corrosion is not a part of the design requirements thus the verified allowable flight hours are set with conservatism.

The pylon #1 is having a chromic acid anodisation as corrosion protection on the outside surfaces and in the rail area also an anti-friction coating of Acheson Dag 580. Subsequent investigations on the root cause of the corrosion damage points on the usage of Dag 580 having a carbon content which gives accelerated corrosion on aluminum. Measures are now taken to improve the corrosion protection.

3.3.8 Fatigue Life Verification of Gripen A/C Swedish Standard Pylon #3

Customer request for increased allowable flight hours for Swedish Standard Pylon #3 with drop tank have initiated extended verification, in this case by fatigue testing.

The Swedish Standard Pylon #3, hereafter denoted pylon #3, is an aluminum box structure with pylon to aircraft forward fitting in titanium and aft fitting in aluminum. The pylon to store forward and aft fittings is made of titanium.

The fatigue test verification has been performed using a load sequence representing missions with pylon #3 carrying drop tank.

General test rig arrangement with load actuators and test specimen are shown in figure 41.

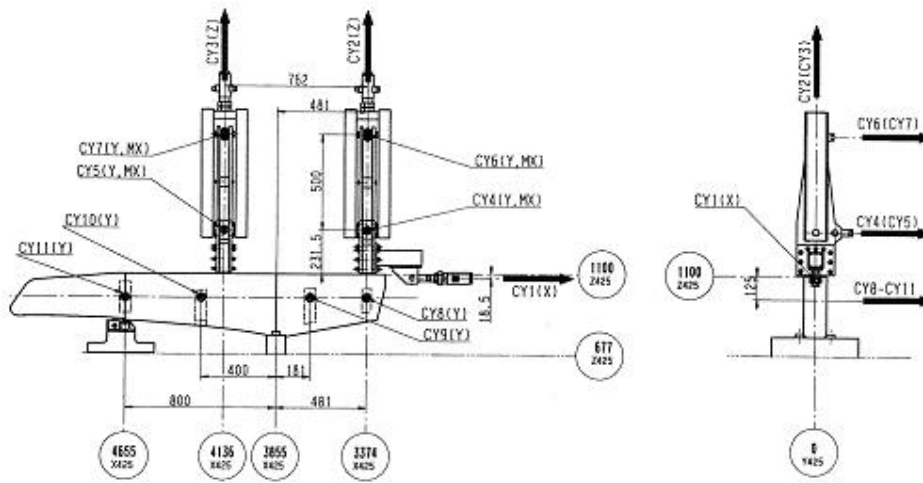


Figure 41. Pylon #3 test rig arrangement.

Two test specimens have been used.

The first specimen #1 was tested to 6000 test flight hours with an additional 6000 test flight hours with increased load level by 50 %. Static measure load cases was applied at specific intervals and strain gauge values were assessed to determine if the structure was still stable and load carrying. Also visual checks were performed at these intervals. After dismantling of the test specimen NDT inspections found fatigue cracks in cut outs in the lower aluminum spar of the pylon box structure, se figure 42, 43 and 44.

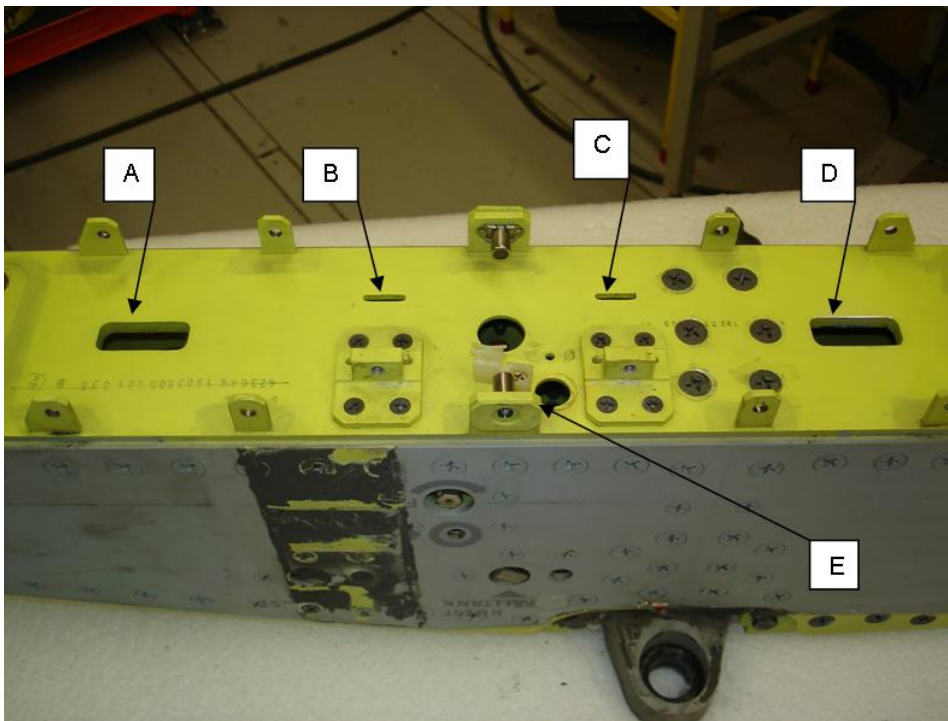


Figure 42. Test specimen #1 - Bottom spar with locations A-D where fatigue cracks have been found.

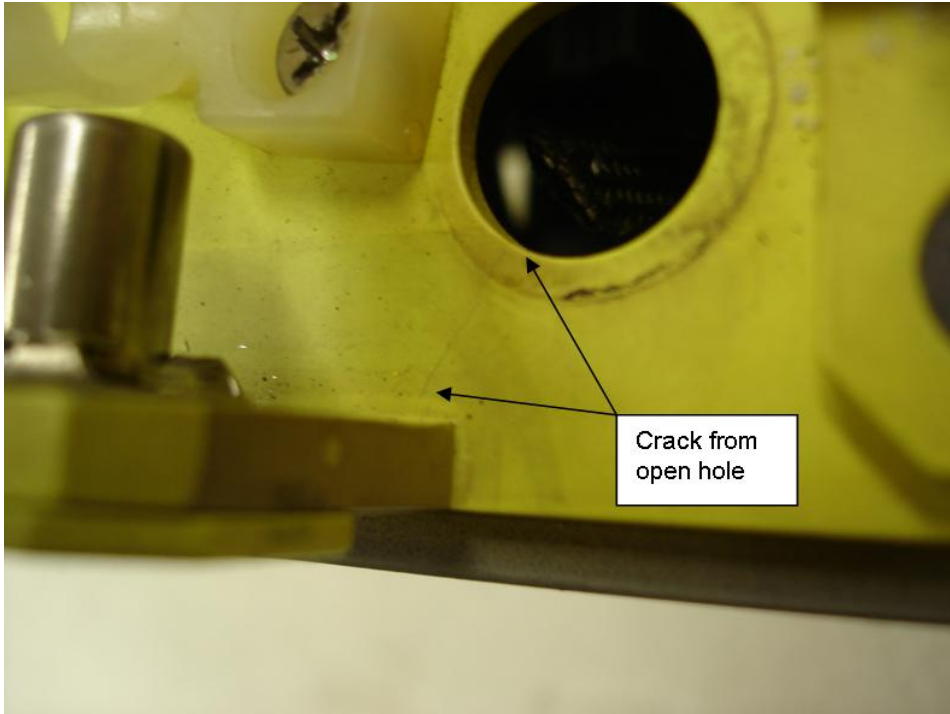


Figure 43. Test specimen #1 - Fatigue crack at hole E.

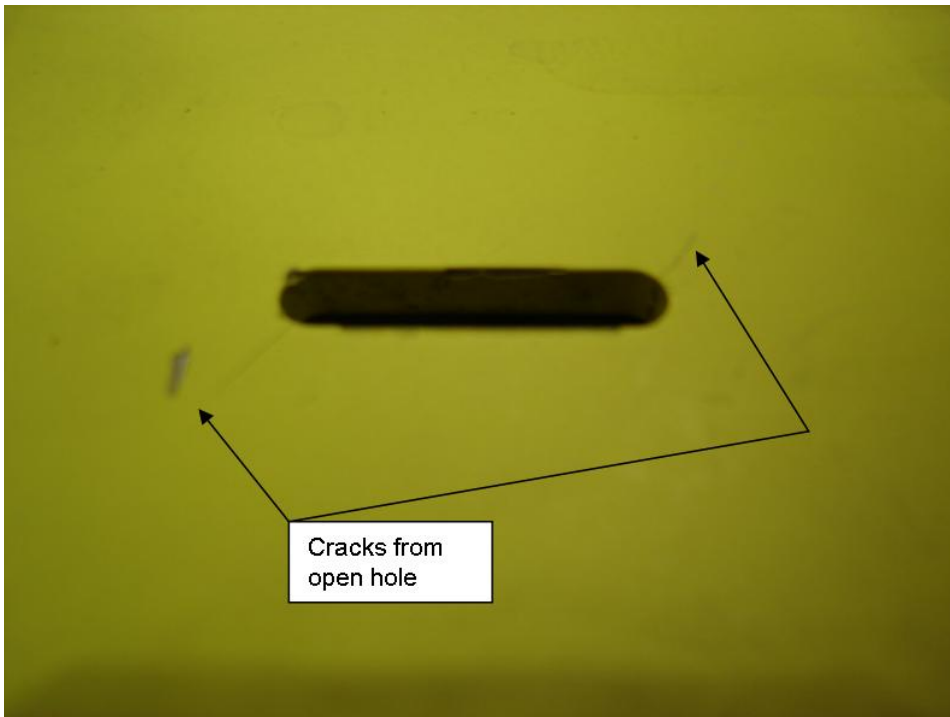


Figure 44. Test specimen #1 - Fatigue crack at hole B.

Test specimen #2 had artificial surface cracks applied by EDM (Electrical Discharge Machining) in the main bolts connecting the forward fitting of the pylon to the aircraft. As for specimen #1 testing was conducted to 6000 test flight hours with an additional 6000 test flight hours with increased load level by 50 %. NDT inspection followed and no crack growth could be observed in the bolts. As a final test the main bolts were replaced with specimen #1 bolts, without defects, and the fatigue test was continued with a severe constant amplitude spectrum. The fatigue test was terminated due to extensive cracks in the bottom spar and side plates, see figure 45 and 46.

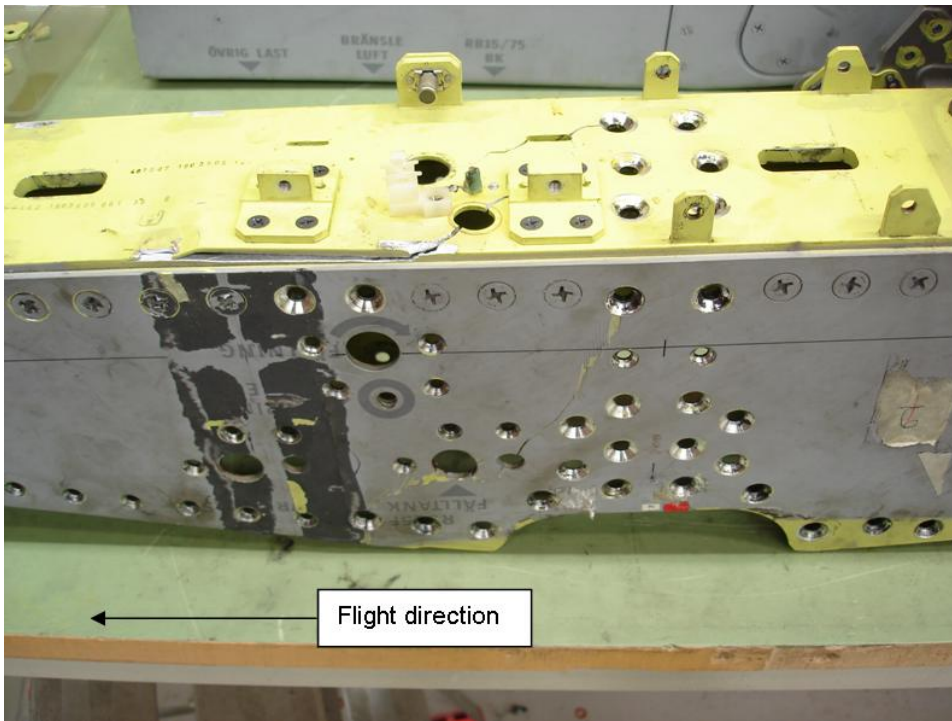


Figure 45. Test specimen #2 – Extensive cracks in bottom spar and sideplate.

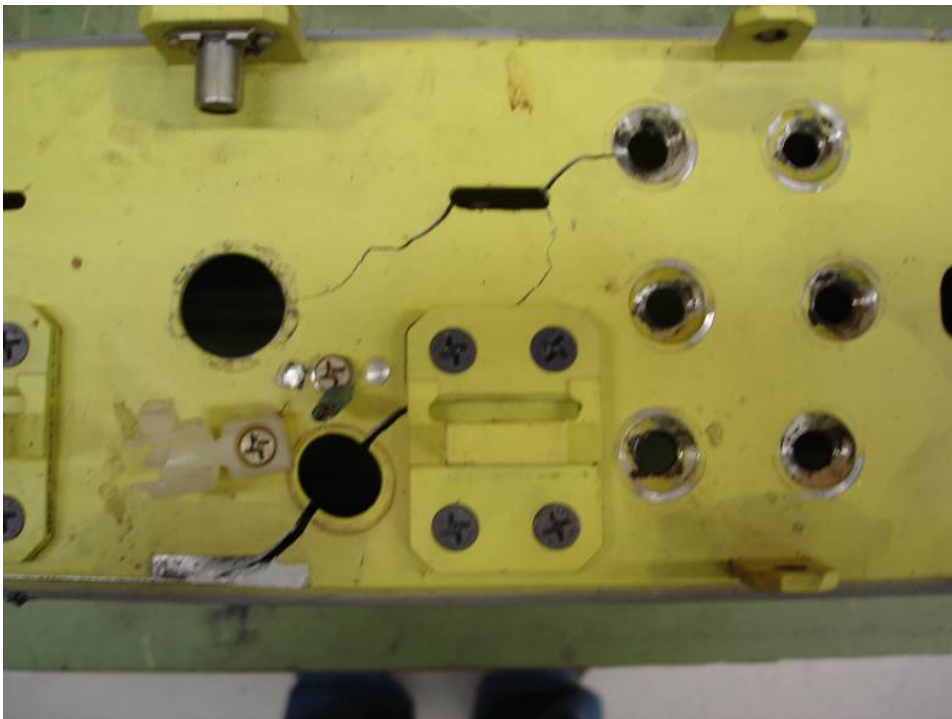


Figure 46. Test specimen #2 – Extensive cracks in bottom spar.

From figure 44 and 46 it can be concluded that the cracks in the bottom spar are caused by shear stresses (due to side load) with several cracks 45 degrees to the flight direction. Cracks in the side plates of specimen # 2 are probably a consequence of the extensive cracks in the bottom spar. No crack where observed in the main fittings. Although damage tolerance was not the main object of the verification, the no growth of the artificial defects in the main bolts give additional confidence when assessing the test results. As a result of the testing a very favorable allowable flight time of pylon #3 with drop tank can be recommended.

3.3.9 Fatigue and damage tolerance aspects of hybrid metal-composite wing structures

The current trend in aircraft design is to increase the proportion of fibre composite structure. As structural parts, the fibre composite materials have several advantages over metal materials. These are: low weight, high strength, high stiffness-to-weight-ratio, good fatigue resistance and low thermal expansion. There are also some drawbacks with using fibre composites, such as sensitivity to compression loading, poor transverse strength, sensitivity to moisture and high temperatures, sensitivity to impact and lack of ability of plastic yielding. Metals, on the other hand, have good plastic yielding properties but are sensitive to fatigue loads and have higher density than composites. Since many primary structures still require to be constructed using metals, the number of interfaces between metals and composites increases. The structures containing both fibre composites and metals are referred to as *hybrid structures*. In the design process of aircrafts, such mixed structures have traditionally often been disregarded as an alternative because of the lack of methodology to handle the mismatch of material properties mentioned above. From fatigue and damage tolerance point of view, the composite-metal interfaces are a challenge and there is a need of new technology to address these problem areas.

Some common areas containing these hybrid structures are found in particular in aircraft wing structures. Junction areas are usually composed of the outer shell of composite and the internal structures (spars, stringers and ribs) of metal. Air friction on the wing and the temperature of the surroundings will create a temperature distribution in the wing and affect the structure components differently depending on their thermal properties. This in turn will cause thermal loads and affect the way the outer mechanical loads are transferred in the structure.

In this project a new design and verification philosophy is developed, with the objective to challenge the current requirements placed on composites as a part of hybrid structures of the aircraft. The goal is to simultaneously reduce the weight and improve the fatigue and damage characteristics of the structure. It will result in a demonstrator object, a simplified wing-like hybrid structure that will be tested and compared to the current all-composite wing on Gripen C/D. The requirements that are challenged involve allowed strain levels, damage tolerance, impact damage, battle damage, fatigue and damage growth, post-buckling behavior and thermal loads. Furthermore, nano coal fibre reinforced composites will be used locally to improve the transversal strength of the conventionally used composite.

Currently, the project is in the pre-study conceptual phase where several possible hybrid structure solutions of the demonstrator box are studied and compared. The idea is to optimize the weight of the demonstrator but also to identify and highlight the issues that arise in connection with different hybrid solutions. This is done in the context of both existing and new requirements mentioned above.

Concept studies

Initial studies are performed on a generic 9-cell box consisting of skins, spars and ribs bolted together as shown in figure 47.

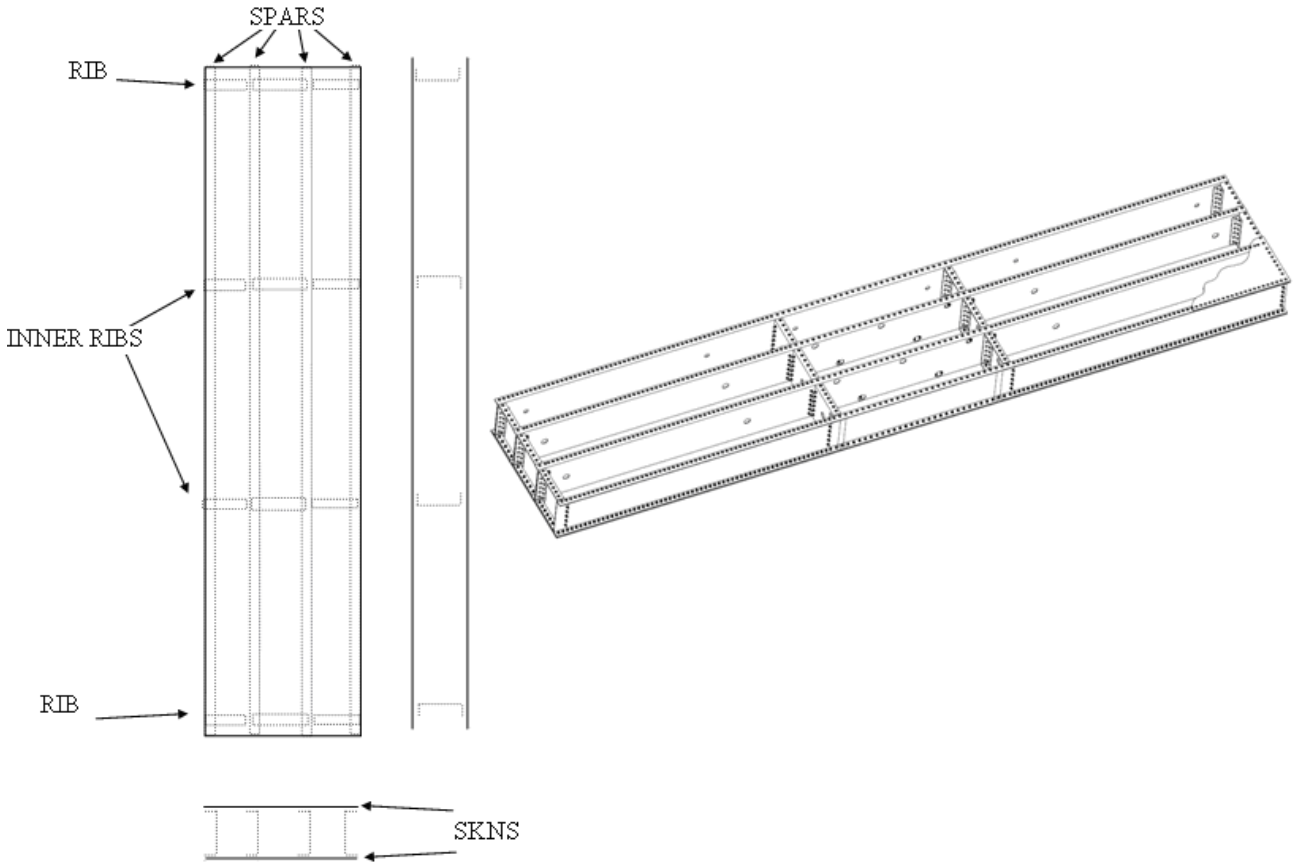


Figure 47. Generic box structure.

Three different concepts are studied and their cross sections showing a spar and skins are viewed in figure 48.

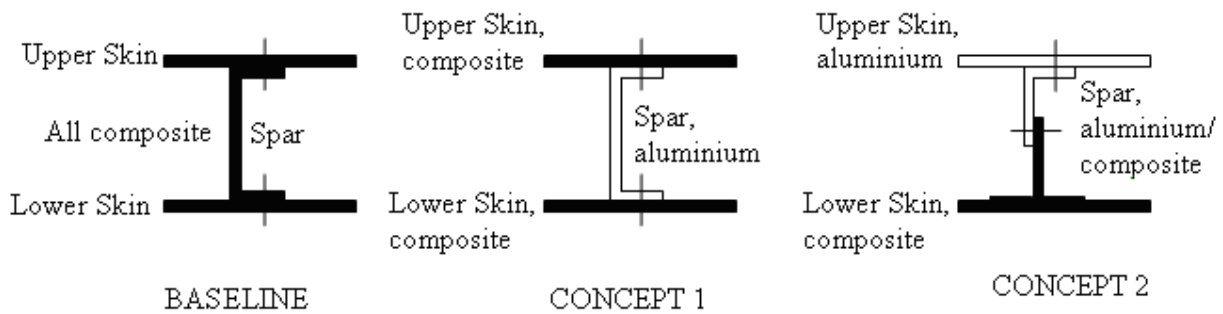


Figure 48. Studied box structure concepts

The loads applied on the box in this study are typical wing loads, a bending and a twisting moment, together with an evenly distributed temperature load. To determine the amount of the mechanical load, the baseline concept (existing Gripen C/D design) is optimized against zero margin for some typical skin thickness in the real wing. Criteria for determining the zero margin in the composite are fibre failure, buckling, bearing failure or net-section failure, whichever is most critical. Then, the same loads are applied on the other two concepts which also are optimized against zero margin. For metal parts of the box, fatigue calculations are performed for some typical wing load spectra scaled with loads determined from the baseline.

The resulting weights of the boxes are then compared. This is done for the existing requirements and the new requirements determined in the project. The calculation methods used for optimizations are conventional in-house Saab methods, but also the finite element method using commercial software's. An example of a result from a post-buckling analysis of middle section of concept 1 using finite elements is shown in figure 49.

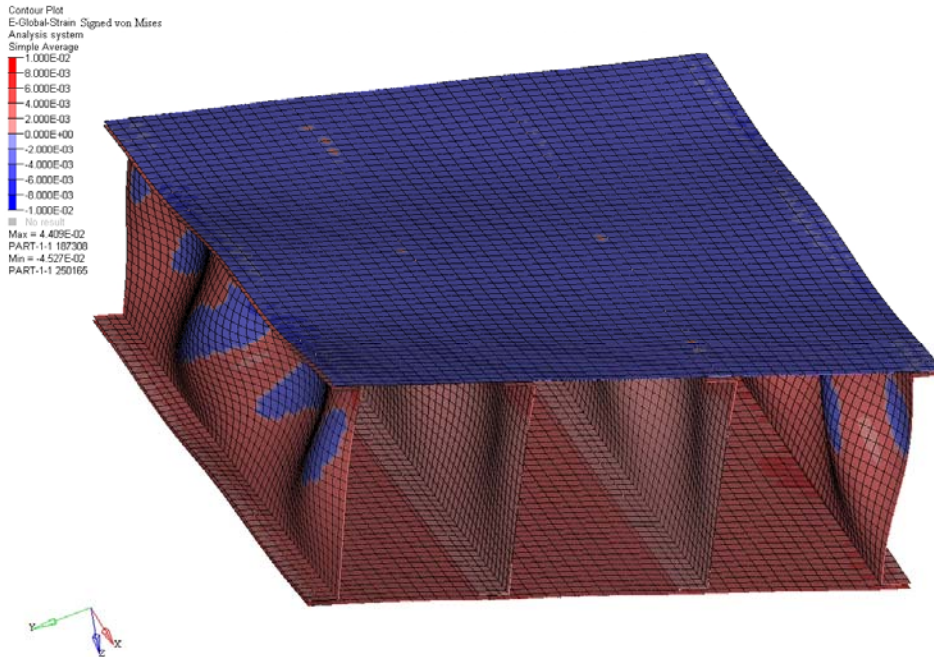


Figure 49. results from post buckling analysis of concept #1.

Utilizing the concept study is expected to indicate the structural concept that is most suitable to be used in the testing. Also, the understanding of the influence of the temperature on the hybrid assembly will be increased as well as the signification of requirement changes.

Significant problem areas that are still relatively little explored within the frame of hybrid structures and require further research are:

- **Global structural level**
On a global structural level the fundamental problem is that the metals and composites have different coefficients of thermal expansion which induces thermal stresses and deformations in all coupling surfaces when the temperature state varies from the assembly temperature. The problem can be properly analyzed by numerical calculation methods like FEM, but the cyclic tests at different temperatures has not yet been studied in detail.
- **Local joint level**
Joints are primary structural features that are affected by a variety of significant parameters such as load transfer and secondary bending, types of fasteners, preload, hole shapes, cyclic friction and more. Design of the joints is mainly based on the testing experience. In the case of hybrid metal-composite joints, problems can arise that have not yet been studied in detail. First, the thermal loads affect the deformation and stress levels, but also the composites and metals are sensitive to different types of loads, typically pressure versus tensile loads. Composites inability to deform plastically also restricts the use of traditional techniques to optimize the metallic joints. Furthermore, the cyclic loading can change local friction which may lead to gaps with local bolt bending and high bearing pressures as a result.
- **Load case related problems**
Metals and composites respond totally different on different kinds and magnitudes of loads and their frequency of occurrence. The question regarding truncation and elimination of the loads is therefore crucial for confidence in the test results. The design load spectra are normally exposed to both truncation and elimination before certification testing is performed. Elimination of low load levels is

performed to accelerate the test. More elimination can usually be performed on the composites than for metals. For the hybrid structure the levels of elimination are therefore based on the experience with metals. Truncation of high loading levels is normally performed for metals, where the highest levels expected over a lifetime have a positive effect on the lifetime because of the plastic deformation and retardation of subsequent crack growth. For the composites, this phenomenon does not exist, instead it is the maximum loads that occur during the aircraft's service life that are usually crucial to the design. Thus, for hybrid structures, there exists a problem and it is important to study this phenomenon in detail.

- **Threshold for delamination growth**
Low velocity impact on composites often causes damages that are barely visible and delaminations that can grow when exposed to cyclical compressive loading. The growth is due to the out-of-plane loading that is present and composites low interlaminar strength. This is accounted for in the design of the composite by dimensioning it so that the residual strength of the material is sufficient, i.e the extent of delamination is below the critical value. For most composite lay-ups this means that the operational loads are well below the values of growth threshold and that there is a certain conservatism built in into the design. There is a need to further study and understand the residual and threshold behavior of the out-of-plane loaded composite structures with impact damages.

3.4 FATIGUE CRACK INITIATION AND PROPAGATION

3.4.1 A Computational Strategy for Multiple-Site Fatigue Analysis

In [4] a computational strategy for multiple-site fatigue crack growth analysis of complex structures was described. The work described here is a continued development of this strategy for fast multiple-site fatigue crack growth analysis of real-life aircraft structural components. Real-life structural parts were singled out for a demonstration (Figure 50). An analysis of the I-beam structure, Figure 50 was initiated in [4] and continues below. For each of the critical regions in the five structures a database (labelled DB1-DB5) has been developed with which accurate stress intensity factor data for over 10^{35} crack scenarios can be derived. Database DB5 is presently not verified and will not be reviewed in detail below. The summary describes the creation of the data bases, the verification work to ensure that K -data that can be derived from data bases are accurate. A fatigue analysis computational strategy has also been developed where new fatigue models for considering load interaction effects has been developed. The fatigue analysis tool uses data from the databases. In the summary below many examples of MSD analysis of the parts shown in Figure 50 is given. The data bases and the tools described below need further verification and validation before being applied to real aircraft structures.

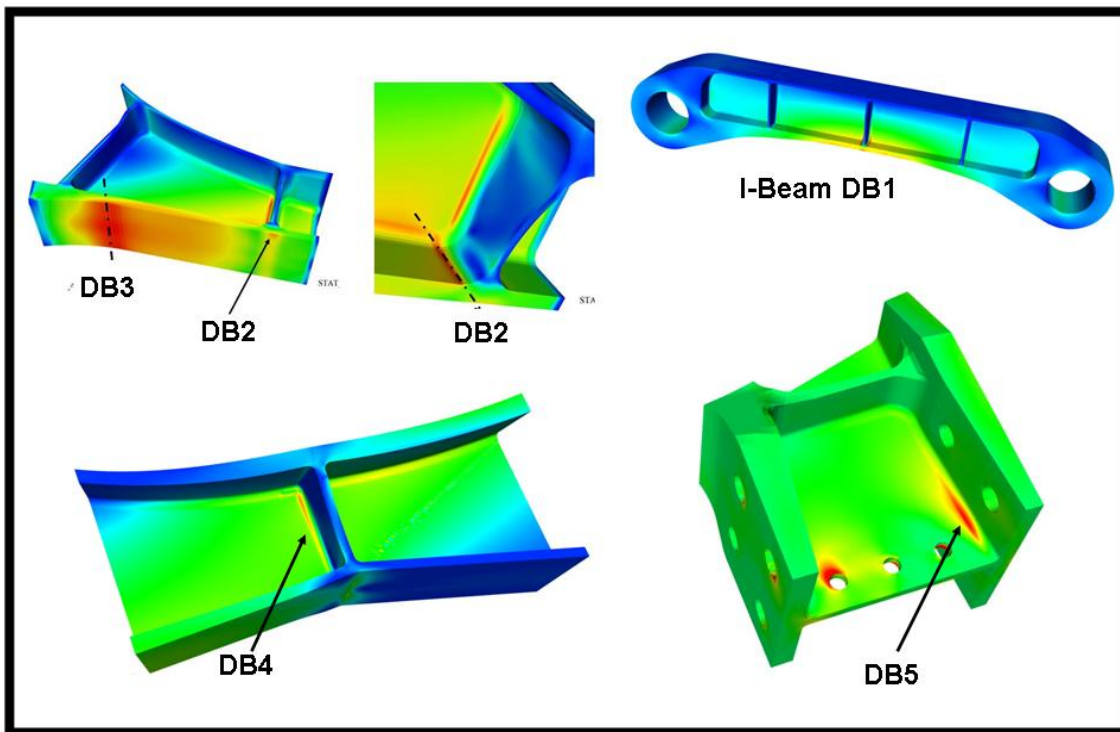


Figure 50 Five structural parts singled out for a demonstration of a new computational mechanics strategy for fast fracture-mechanics based fatigue analysis of complex components

Consider first the I-BEAM structure discussed in [4]. The methods, the theory, the computer implementation and the computational efforts needed to create the stress intensity factor data bases called DB1 are described in detail in [4]. Figure 51 sketch the mathematical principle behind deriving over 10^{35} accurate 3D fracture mechanics solutions in short time.

For fatigue crack growth calculations, the cycle-by-cycle computation method was used in the project such that the method can be applied for the multi-channel arbitrary spectrum loading condition. If crack front shapes are approximated with semi-ellipses or quarter-ellipses, two crack parameters, along with the crack centre location, are enough to describe the shape of each crack.

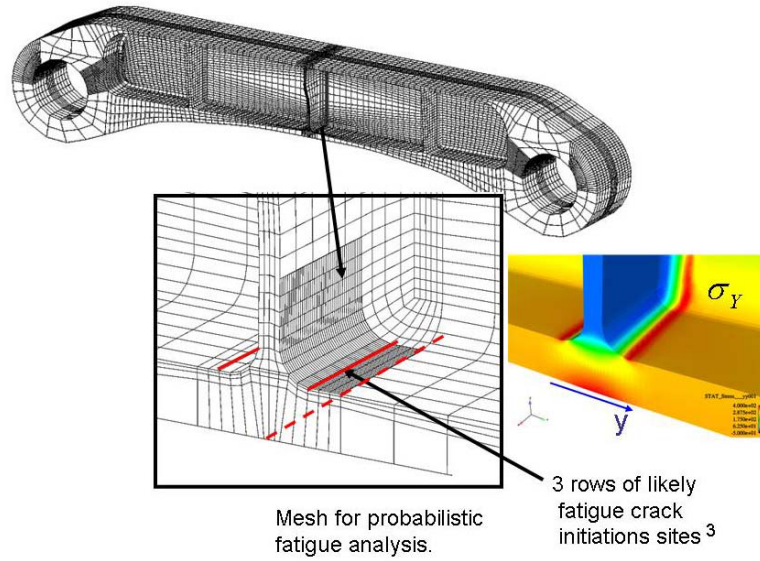


Figure 51: Three crack rows in I-beam. Data for the three crack rows are stored in a data base labeled DB1.

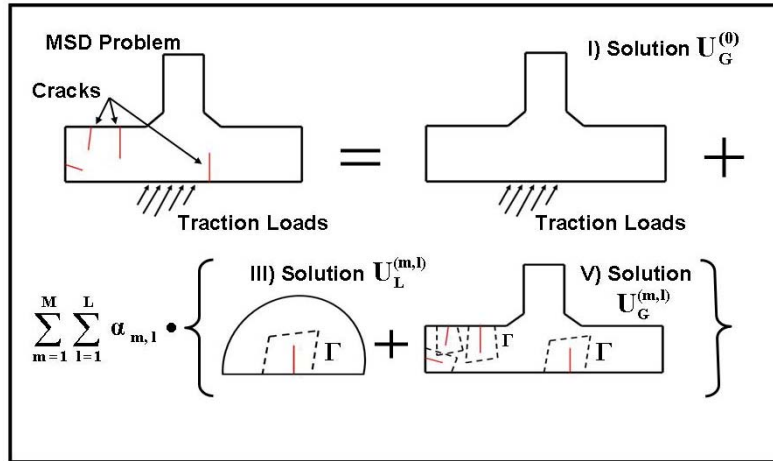


Figure 52. Schematic description (in a 2D setting) of the splitting method

The cracks that were analysed are placed arbitrarily in several critical sections, and at critical locations in the substructures shown in Figure 50. At each crack location, the stress intensity factor is affected by all the crack sizes and locations x involved in the model, i.e.

$$K_I = K_I(a_1, c_1, x_1, a_2, c_2, x_2, \dots) \quad (1)$$

The change of size for each individual crack dimension of any crack will affect the value for K at all the other cracks. If M simultaneous cracks are considered, an accurate approximation \tilde{K} to the stress intensity function (1) is needed for each crack in the MSD-scenario where the stress intensity factor for each crack is a function of $3M$ variables. i.e. crack size (a , c) and the locations x of the M cracks. No stress intensity factor handbook exists that provide stress intensity data even for small values of M . In the present work, the number of interacting cracks M ranges between 5 and 18 in the four databases discussed in more detail below. The largest database (DB1) contains $M=18$ possible cracks. Hence the data base DB1 contains data for $(2^{18} - 1)$ crack scenario where for each scenario more than hundred different crack sizes are available that is $> 10^{30}$ accurate \tilde{K} -approximations are available in DB1.

Clearly, fatigue analysis of complex multiple-site cracking behaviour in complex parts (Figure 50) is not practically feasible unless specially designed numerical procedures are applied. A method with the desired generality and efficiency has been available for sometime, i.e. a mathematical foundation for existence, uniqueness, and convergence of a solution with which a vast number of stress intensity factor solutions can be derived fast and to acceptable computational costs, see figure 52.

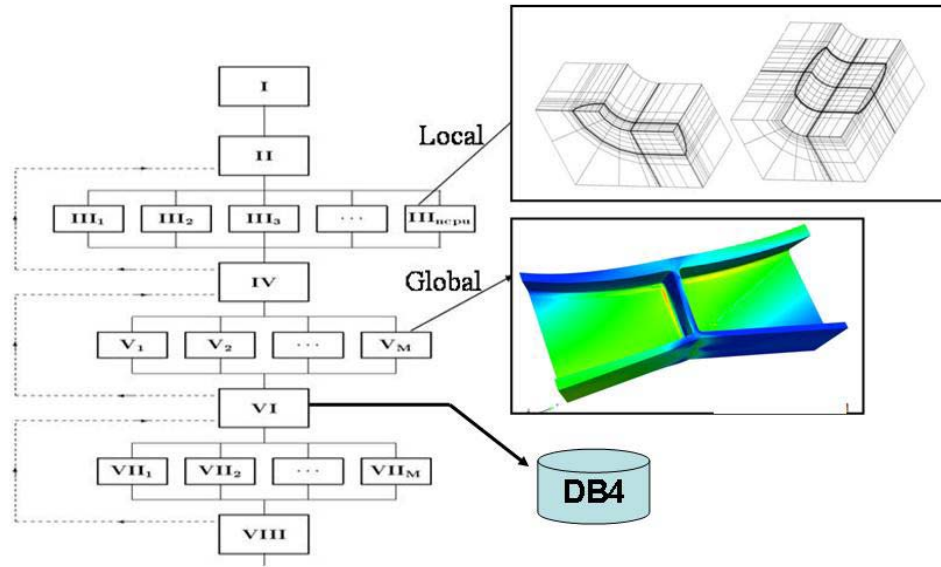


Figure 53. Schematic picture of computer implementation of splitting scheme, and an example of a large level V structure are shown.

Up to now, this theory/method has never been practically implemented on the present scale, that is for analysis of complex aircraft components with up to $M=5-18$ interacting three-dimensional cracks in aircraft substructures.

The work described in [4] contains a description of the five databases and software with which stress intensity function approximation for each crack in over multiple-crack scenarios can be calculated. A software 'PROG' attached to the general fatigue analysis user interface can be used to derive stress intensity approximations from the five data bases for each crack in the MSD-scenario at any of the five critical locations. The software for K -calculation is also used in the module for fatigue crack growth analysis. Figure 53, left part exemplify crack sizes (a,c) for semi-elliptical cracks for which stress intensity functions are available in the data bases. The right part exemplify calculated stress intensity factor variation along the crack front for different (a,c) for a corner crack. Note the complex K -behaviour near vertices where the crack front intersects with the free surface ($\varphi = 0, \varphi = \pi/2$).

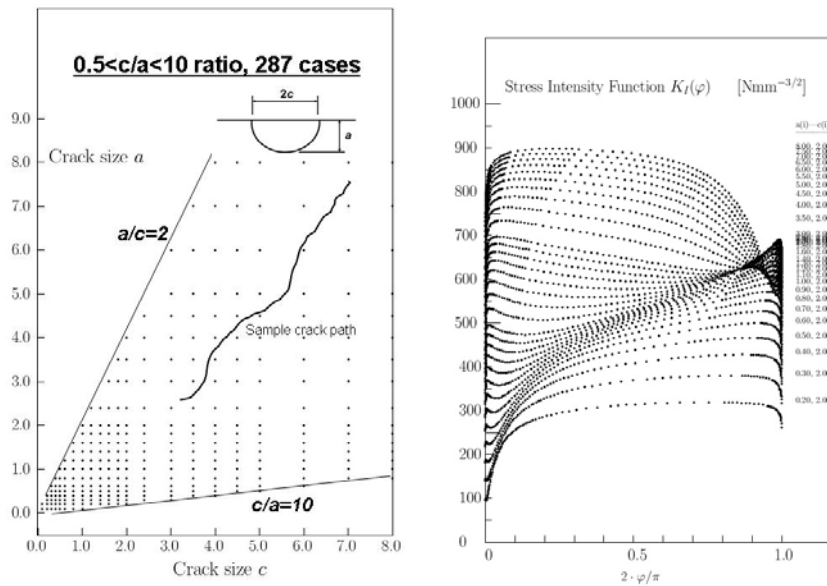


Figure 54: Graphical presentation of all (a, c) (unless global geometry prevents cracks of actual size) values contained in the five databases for all locations x .

The scientific techniques used for deriving the four data bases were in [4] mainly given in a two-dimensional setting in order to avoid the very complex mathematical notation otherwise needed. The local and global FE-meshes used for data base creation for multiple-site statistical fatigue analysis were shown and the system setup to handle the about ten thousand input data files sketched. The vast amount of computer resources in form of CPU-time and hardware (temporary disk, memory) needed to create the data bases was summarized. The computer time for each of the 10^{30} solutions requires just a fraction of a second computer time. Access to the five databases for fatigue analysis and stress intensity factor calculation (program "PROG") is made via the graphical interface. The graphical interface is used to define the (initial) multiple-site crack scenario (via the variables (a, c, x) and crack rows) and the desired type of analysis.

3.4.2 Fatigue Crack Growth Model for Multiple Site Fatigue Damage Evaluation of Complex Structures

This fatigue analysis package used is based on the latest development in both the fatigue crack growth prediction methods, and the fast high accuracy methods discussed above for solving multiple crack problems in complex structure details. The fatigue crack growth model is based on the strip yield crack closure model for the lead crack of the multiple crack problems. The package is capable of accounting for the small crack growth and the load interaction behaviour, so long as the plasticity induced fatigue crack growth mechanism is dominant. With the extension of its capability to the leading crack of multiple crack problems, it is shown that a rather robust platform may be created to evaluate fatigue crack initiation and propagation in complex structure details.

Together with high accuracy numerical solutions for the structural details in the form of discrete data base for stress intensity factors, this method will start from some basic intrinsic material parameters to provide predictions of fatigue crack growth in complex structural detail even when the multiple site damage occurs. The solution makes it possible for a probabilistic evaluation [9] of the fleet when variations in material initial condition and the application loads are considered. Such analyses might provide useful guidelines to develop an efficient life management strategy for fleet management.

For the fatigue crack growth evaluation, several databases will be needed based on high accuracy finite element solutions. These databases consist of discrete stress intensity factors for all the possible combination of crack patterns at critical locations of the structures.

For the fatigue crack growth evaluation, the cracks are considered to be placed arbitrarily in several critical section of the critical detail considered (Figure 50). At each crack location, the stress intensity factor is affected by all the other cracks involved in the database. For each crack, the stress intensity factor is determined from (1).

Clearly, K is a function of the size, aspect ratio, and location of all the cracks. For the fatigue crack growth calculation of each crack under arbitrary fatigue loading condition, a cycle-by-cycle computation is preferred so that the method can be applied for the multi-channel arbitrary spectrum loading condition. Obvious, the stress intensity factor should be determined from the stress intensity data base that consists of discrete solution of stress intensity factors.

For an arbitrary increment in crack size and location, the stress intensity factor will be determined by:

$$K = K_0 + \Delta K \quad (2)$$

where K_0 is the initial state and ΔK is the change of stress intensity due to the crack growth. The increment in the stress intensity factor can be written as

$$\Delta K(a_1, c_1, x_1, a_2, c_2, x_2, \dots) = \sum_{i=1}^N \left(\frac{\partial K}{\partial a_i} \Delta a_i + \frac{\partial K}{\partial c_i} \Delta c_i + \frac{\partial K}{\partial x_i} \Delta x_i \right) + 0(\dots) \quad (3)$$

By omitting the high order terms in the above relation, the first order approximation the stress intensity factor may be calculated according to the crack increment using

$$\Delta K(a_1, c_1, x_1, a_2, c_2, x_2, \dots) = \sum_{i=1}^N \left(\frac{\partial K}{\partial a_i} \Delta a_i + \frac{\partial K}{\partial c_i} \Delta c_i + \frac{\partial K}{\partial x_i} \Delta x_i \right) \quad (4)$$

The partial derivatives can for example be estimated from difference quotes (compare figure 54 for the case when K is known at each point (a, c) shown).

For the three dimensional multiple site fatigue crack, it is adequate to approximate the fatigue crack with part elliptical shape with the growth potentials along the axial direction and the central locations. Two types of cracks are considered, the surface crack and the corner crack. For the corner crack, it is needed to be considered only the crack growth along the axial direction of the ellipse while for the surface cracks, the growth along the axial directions as well as the centre of ellipse should be considered. Under fatigue loading condition, the crack growth da and dc are considered for the corner crack. For the surface crack on the other hand, the central movement dx .

For two-dimensional cracks, a uniform virtual growth is considered when computing the strain energy release rate. The same methodology is considered here for three dimensional cracks with considering a virtual crack growth at each degree of freedom for the virtual crack growth at each side of an elliptical crack, see Figure 55. These virtual crack growths give three strain energy release rate, corresponding to the left side, right side of the crack, and the depth of the crack. By using the strain energy release rate of these virtual crack growth patterns, three distinguish equivalent stress intensity factors can be computed to characterize the virtual crack growth capability along three directions.

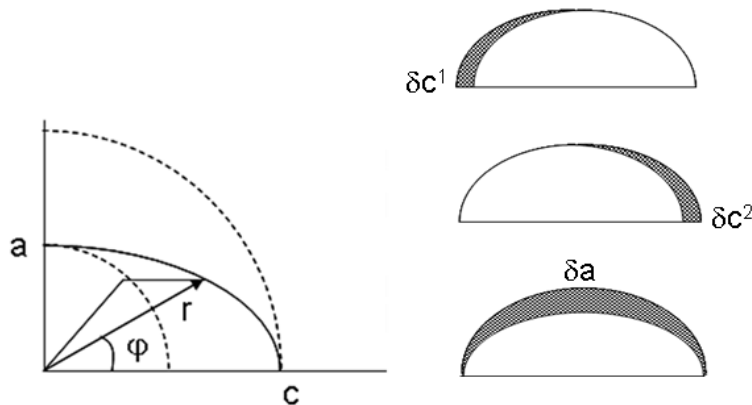


Figure 55: Geometrical quantities and schematic of the virtual crack growths

Two alternatives for the linkup of cracks are considered, depending on severity of crack size on the surface or in the depth, for the computation efficiency and algorithm stability, see Figure 56. For both solutions, the area of new crack is assumed to be the sum of the old crack areas so that the loss of the load carrying capability of the material is maintained.

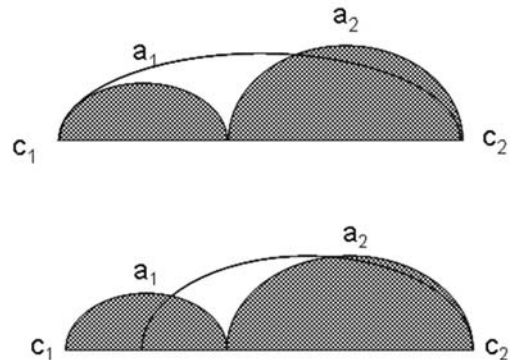


Figure 56: Linkup assumptions for MSD

Figure 57 shows a flow diagram of the procedure. Start with the global usage of the aircraft like the information recorded in the central accelerometer, the recording from the onboard health monitoring system is used to construct strain spectrum for each critical structural detail. The stress result from the global finite element analysis is used to create boundary condition for the local model for MSD crack pattern. The MSD solutions are saved as various databases in the crack growth prediction program which provide the stress intensity factors for various load cases and crack patterns.

Together with the material parameters stored in the material database, the simplified crack closure model is applied as the linear computation for MSD and multiple channel load conditions. This computation will provide the first iteration results for the pattern of MSD and approximately, the growth of crack as a function of the applied load cycles.

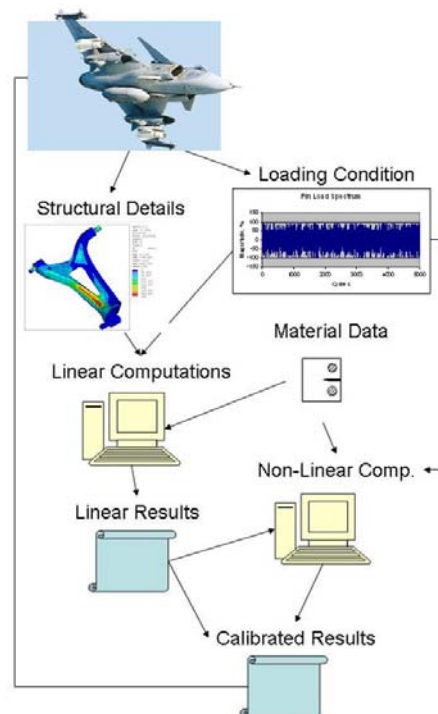


Figure 57: Program flow of the MSD fatigue crack growth analysis program

One comparison with NASGRO prediction of fatigue crack growth is shown in Figure 58 for a given maximum stress level with various stress ratios for the different constant amplitude loading conditions for a standard fatigue test specimen (CCT). In this figure, the symbols represent predictions from the strip yield model and the curves represent predictions from NASGRO. Despite the significant difference in the basic solutions, both methods have good agreement in the regime of high stress ratios. With reduced stress ratio, the strip yield model indicates stronger stress ratio effect than NASGRO model even though the agreement between them is still considered to be adequate. In these comparisons, the crack is started from a rather large size ($a=1$ mm) so that the application range of NASGRO is not violated.

Compared to NASGRO in this case, the predictions using the strip yield model uses much less material data. In addition to the basic material properties like Young's modulus, yield and ultimate stress, Poisson's ratio, there are just four fatigue data used. The parameters include the slope of the crack growth rate, the intrinsic threshold values for stress intensity and the corresponding crack growth rate, and the parameter to characterize quasi-static crack growth rate acceleration. Naturally, the reduced dependency on the experimental data will increase significantly the robustness of the prediction method.

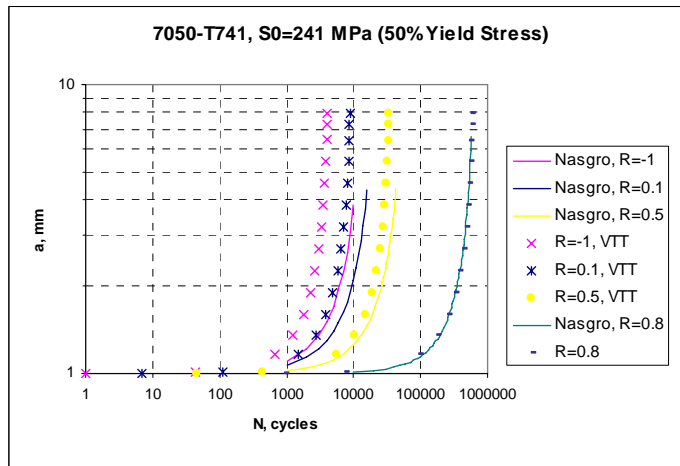


Figure 58: Comparison for fatigue crack growth predictions between NASGRO and the single crack strip yield model used in present work

Similarly, for example, the fatigue life for various initial leading crack sizes and different load levels may be computed with the Monte-Carlo generated initial cracks. The results for the case of I-Beam are shown in figure 58 for the fatigue life, in the terms of spectrum blocks, as function of the cracks sizes and the load levels. Such results are rather helpful for determining a strategy for the fatigue management of the structures when the initial surface conditions are changed and the structure may be used more or less severe than the initial design target. Clearly shown in this result, the change in initial crack size in an order of magnitude will change the fatigue life in nearly an order of magnitude. A 15% rise in the stress level will lead to about 100% reduction in fatigue life.

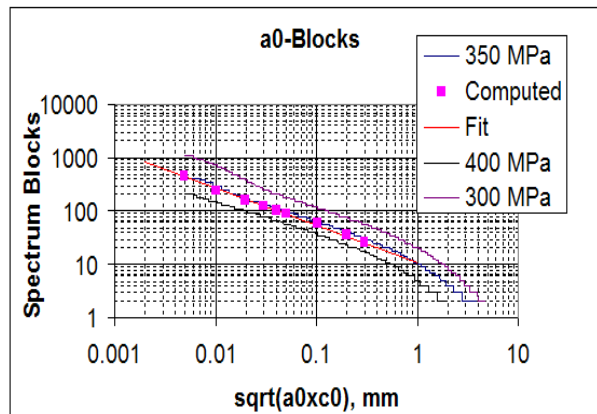


Figure 59: Fatigue life as functions of the initial leading crack size and the load levels

For the multiple site fatigue initiation in a fleet of aircraft used in various missions, the initial condition of each individual aircraft may differ and the usage may be different due to the mission requirement. There will be an uncertainty about how fatigue crack may be initiated and propagated. With some basic information about the variation in the initial conditions, the materials, and the load conditions, a probabilistic analysis may provide valuable indication about how the fatigue status may become. In a fleet wise management of the multiple site fatigue damage, it is often necessary to identify how the leading damage in the multiple site fatigue, or the leading fatigue damage in a fleet, may become after a period of usage. In such a situation, it is often necessary to consider the order statistics of the fatigue damage.

The order statistics takes care of the effect of sample size [9]. For example for a fleet size of n , each object is subjected to a random initial condition and a random fatigue loading condition with a probable fatigue damage after a period of usage. For the fatigue management of the fleet, it is a question to determine whether or not to accept the health of the whole fleet without a single failure. In this case, the leading damage in the fleet will be an important reference for the fatigue management of the fleet.

With the solution for the fatigue crack growth as a function of the initial defects sizes and the load spectra, it is possible to make Monte-Carlo simulations according to the size of fleet, the initial probabilistic defects, and the variation in the load. For an example, I-Beam case is considered. In this case, the initial defects are in a range of 10-100 micrometers. Two fleet sizes are considered. One is for a size of 50 airframes. Another is for a size of 100 airframes. Suppose the variation in the stress is between 304 MPa and 350 MPa, the Monte-Carlo simulations give the probability of failure as a function of fatigue time (load blocks) as in figure 59 shows. It is shown in the results that larger fleet size (100 in the example) will have shorter fatigue life for the leading member of fleet. This means a shorter inspection threshold for a larger fleet. In plain words, the more frames in a fleet, the short inspection interval will be to uncover the leading fatigue damage in the fleet since it is more likely to have severe damage among a larger fleet.

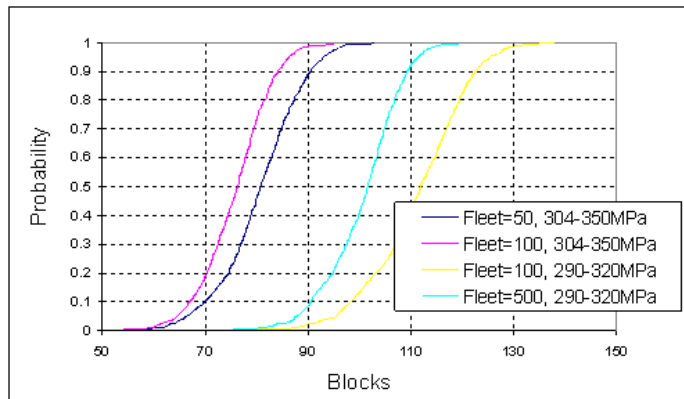


Figure 60: Probability of failure as a function of the spectrum fatigue blocks for different fleet sizes and stress levels.

Reducing the stress level will increase fatigue life of the frames. For the example as shown in Fig. 59 with a reduction in the stress level between 5 to 8 %, there will be a more than 40% increase in the fatigue life.

3.4.3 Verification of Calculated Stress Intensity Data for DB1-DB4

A scheme was developed that with reasonable probability guarantees that all computed stress intensity functions are accurately calculated. The strategy selected for verification is based on the fact that the about 10^{35} possible crack scenario are built up by $>10^4$ unique surface cracks of quarter- or semi-elliptical shape located at discrete locations in five structural details (Figure 50).

The hp -version of the finite element method and so called advanced methods for K -evaluation has been used [5]. This is the basis for the verification work, i.e. that unique FOI-methods for accurate and reliable stress intensity factor calculation have been used. In order to derive the 10^{35} solutions in reasonable computer time a unique FOI technique for multi-scale analysis (splitting scheme) was adopted [4,6].

By using the high-accuracy methods mentioned, the greatest risk for database errors hence are due to human handling errors. The total CPU time used to create the databases is of the order 10 years on a single processor computer system. Tenth of thousands of jobs have been submitted so human handling errors happened and were discovered thanks to the strict verification scheme developed which is briefly described below. The results summarised in the present report are derived from the databases in their final stage.

For verification purposes we will here use data from the large compilation of stress intensity factors [8]. The accuracy of the solutions in [8] is generally unknown and is often claimed to be of the order 1-3, % (relative accuracy). However, earlier work [7] has shown that errors might sometime be an order of magnitude larger! The differences in geometry between idealized geometries in [8] and the actual geometries analysed here, different load systems cause additional and unknown errors.

The accuracy of solutions reported in [8] was in some cases checked by re-computing basic data in order to verify the solution accuracy in [8]. Hence, a set of critical data were calculated using the *hp*-version of FEM. In some cases where there are too few data points in accurate reference solutions are derived by direct simulation using a block-shaped domain having a corner crack or a half-elliptical surface crack. The reference solutions were also analysed with the multi-scale scheme as to demonstrate that the splitting method provide stress intensity factor data that are typically an order of magnitude more accurate than data in [8].

It was of course not computationally and manually possible to verify that $K_I(\varphi)$ for each crack in each of the 10^{35} crack scenarios, for each loading case are correct without any reasonable doubt. The approach taken in the verification work consists of six major steps.

Step 1 For the about 10^4 cracks which are small, relative to structural dimensions and appearing stress variations, the calculated stress intensity factors can be compared with existing data in the reference text [8]. The work in this step consisted of detailed stress analysis (available from database generation) and estimation of linear stress gradients in order to compare with solutions from [8].

Step 2 For multiple-site crack scenario, the checking is significantly more difficult since there are no solutions available in the literature for the complex geometrical details investigated in the present work (Figure 50).

A few solutions for twin cracks in semi-infinite domains are available from [8] but only for Poisson's ratio $\nu = 0.0$. In order to be able to compare data for $\nu = 0.3$ a set of accurate solutions were calculated using direct simulation and the *hp*-version of FEM.

For small crack sizes (see page 854 in [8]) interaction effects are small so many formal system checks can be made by analysing multiple crack scenario with 2-18 simultaneous small cracks (of size 0.1-1.0mm) with minimum spacing of about 3 mm. A test module is created with which about 10^5 randomly selected MSD-scenario and crack sizes (of size <1 mm) were analysed. The numerous $K_I(\varphi)$ -distributions calculated in this way were compared with the corresponding single crack solutions.

The criterion used in this step 2 type of check is that the maxim relative error in K_{\max} in the millions of K -solutions analyzed must be less than 1% for each and every K -distribution tested.

The type of tests performed in this step is not so much focused on accurate K -calculation for MSD-scenario, the test is more a test of the correctness of the software used to extract MSD-solutions. The random generation of MSD-patterns and crack sizes, respectively will address various parts of the five databases DB1-DB5 quite randomly which is a good test of the data bases and the software used (but only for crack sizes $a < 1$ mm).

Step 3 In this step interaction effects between 2-6 nearly touching cracks are verified. The calculated stress intensity functions for using data bases are compared with handbook solutions for twin cracks and an infinitely long row of cracks. For larger crack size a , there are no handbook solutions available.

Hence, for the purpose of testing the multi-level scheme used to derive data bases DB1-DB5 a block-shaped domain with two nearly touching cracks were analysed using the methods described above. The solutions obtained were verified against [8] and detailed FE-solutions obtained with the *hp*-version obtained by explicit modelling of the twin cracks.

Step 4 In this step, interaction effects between crack rows are verified, hence only two data bases, DB1 and DB2 are of interest. It is found that interaction effects between crack rows are small except for larger cracks ($a, c > 4-5$ mms, say).

The interaction effects can only be verified by direct simulation using global domains with cracks *explicitly meshed* in the global FE-mesh. A simple mesh generator was written which adds cracks of rectangular shape in order to quantify interaction effects for large cracks. In the verification, quarter- and semi-elliptical cracks are replaced by rectangular-shaped cracks of same (crack) area.

The procedure in step 4 then is the following: calculate stresses in crack rows due to large (rectangular) cracks in a separate crack row, use [8] to estimate stress intensity functions $K_I(\varphi)$ and compare these with data obtained from databases DB1 and DB2 for multiple-site crack scenario.

Step 5 This step is less scientific, i.e. it consists of just plotting K -distributions as function of increasing $a, c, c/a, x$ etc and to monitor any anomaly between the K -functions (compare right part of figure 54). The K -distributions must change continuously with continuously changing parameters and any non-smooth change in K -curves is most likely the result of an error in computed data.

Step 6 This final check of K -values, is performed inside the fatigue analysis module. Only the principles are mentioned here. Based on the initial crack scenario the K -values initially normally increases with roughly square-root behaviour. Based on the work under steps 1-3 approximate expressions for the increase in K at least for cracks < 3 mm have been derived and is used in the fatigue module to check that the evolution of K during the fatigue life is within the bounds estimated in steps 1-3.

Verification: A few results from the verification testing are given below. Stress intensity functions for $1/4$ - and $1/2$ -elliptical cracks are first compared with reference solutions. For quarter- or semi-elliptical cracks with elliptical fronts of a size characterised by the half-axes (a, c), the angles θ and φ are defined by the equations 1 and 2, respectively.

$$\begin{aligned} x_{local} &= a \cdot \cos(\varphi) \\ y_{local} &= c \cdot \sin(\varphi) \end{aligned} \quad (5)$$

and,

$$\tan(\theta) = y_{local} / x_{local} \quad (6)$$

The mode I stress intensity function K_I , is in [8] expressed as a function of the angle θ while graphs shown below are plotted in a $K_I - \varphi$ coordinate system. The “ x -coordinate” shown in figure 80 is the x -coordinate used to define the crack centre locations when stress intensity factors for the data bases are verified. Note that the definition of the θ -angle is the same for $1/4$ -elliptical and $1/2$ -elliptical cracks independently if cracks are located on the inner or outer flanges. Hence, points on a crack front with the smallest ‘ x -coordinate’ has the smallest θ -values independent of crack location and type of crack.

The behaviour of the stress intensity functions near the two crack vertices, i.e. where the crack front intersects with the free surface is very complex and non-uniform (see right part of Figure 54). Special care has to be taken in order to accurately calculate the local peak-values of K_I . The *hp*-version of finite element method used in the present analyses uses a very strong mesh grading towards the crack front and toward the two vertices in order to capture the strong gradients in stress intensity function K_I . Generally the stress intensity function has its maximum value near the two vertices for semi-circular cracks. For cracks with a slightly larger than c , the maximum value of the stress intensity factor is located at a distance from the flange surface. We will use a result from database DB3 to exemplify the general trends. The K -distribution shown in Figure 61 was obtained for a $1/2$ -elliptical crack of size $a=6.0, c=6.0$ and with centre at $x=6.14$ in database DB3. The functions are plotted with about 10 points per finite element along the crack front that is about 130 points for $1/4$ -cracks and 260 points for $1/2$ -cracks which gives rather smooth and continuous curves. The figure 61 shows that peak values of K_I are located very close to the crack vertices for $\nu = 0.3$. At the vertices $K_I = 0$ for Poisson’s ratio $\nu \geq 0.0$. The

high-accuracy numerical solutions derived here capture this vertex behaviour well. This is not the case for any three-dimensional solution (for $\nu > 0$) given in the handbook [8].

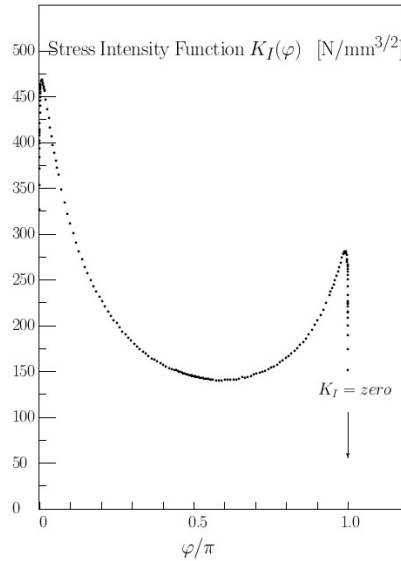


Figure 61 Calculated K_I -distribution along crack front for $1/2$ -elliptical crack in database DB1. Close to the two vertices the stress intensity function drops sharply to 0 (zero).

The accuracy of solutions available in handbooks [8] has often been questioned. For example, the classical K -solutions for two cracks at a cylindrical hole derived by Newman-Rajau were recently discussed in [7]. Surprisingly, relative errors of the order 20-30% were sometimes found.

We finally note that weighted values of the stress intensity factor $K_I(\varphi)$ equations 7-9 are used in the fatigue analysis that is, the sometimes very strong K_I -variations are partly smeared out when using the averaged values.

$$\bar{K}_c = \sqrt{\frac{2}{\pi} \int_0^{\pi} K_I^2(\varphi) \sin^2 \varphi d\varphi} \quad (7)$$

and

$$\bar{K}_{a1} = \sqrt{\frac{4}{\pi} \int_0^{\pi/2} K_I^2(\varphi) \cos^2 \varphi d\varphi} \quad (8)$$

and

$$\bar{K}_{a2} = \sqrt{\frac{4}{\pi} \int_{\pi/2}^{\pi} K_I^2(\varphi) \cos^2 \varphi d\varphi} \quad (9)$$

Accurate integration, equations 7-9 are straightforward ones having access to smooth functions of the type shown in Figure 61.

Table 1 summarizes six of the most frequently used reference solutions from [8] in the present verification work.

Crack	\mathcal{G}	Load	Pages in [8]
Single $1/2$ -Elliptical Surface Crack	0.3	Tension	692-697
$1/4$ Corner Crack	0.3	Tension+Bending	728-730
Single $1/2$ -Elliptical Surface Crack	0.3	Tension+Bending	725-727
Single $1/2$ -Elliptical Surface Crack Near Corner	0.3	Tension	742-743
Two $1/2$ -Elliptical Surface Cracks	0.0	Tension	848-854
Two Semi-Circular Surface Cracks	0.3	Tension	855

Table 1 Solutions from [8] used in verification work.

Stress intensity factors for cracks in simple block-shaped domains. In the verification work of databases DB1-DB4 the influence of differences in aircraft geometries and the handbook geometries on K_I will remain an uncertainty since stress intensity factors for three-dimensional cracks given in hand books apply only to idealised geometries.

Hence it is of interest to compare results obtained with the splitting method for single- and multiple-crack scenarios with solutions in [8], i.e. when the domains are very close to be identical. A brief comparison of results from analysis of simple domains are given below and compared with solutions from [8].

The objectives this model study was:

- Derive stress intensity factors for single and multiple quarter- and semi-circular cracks in a $\frac{1}{2}$ infinite and $\frac{1}{4}$ infinite domains (i.e. very large domains) by using the splitting scheme
- Demonstrate that these solutions are accurate, *with respect to the exact mathematical solution* to 3-4 digits relative accuracy for the p -level used when deriving the databases DB1-DB4.
- Compare the calculated stress intensity factors for quarter- and semi-circular cracks with solutions in [8]
- Calculate stress intensity factors for quarter-elliptical surface cracks close to the vertex in a quarter infinite domain
- Compare these K -solutions to the few data in [8]
- Derive K -solutions for closely spaced twin cracks in a semi-infinite space for $\nu = 0.0$
- Compare these K -solutions to data in [8] where many solutions for $\nu = 0.0$ are available
- Derive solutions for $\nu = 0.3$, i.e. solutions that are not available in [8]. Use these solutions in the verification work (Steps 3,4 and 6)

Two block shaped domains with dimensions $(-24 \leq x \leq 0, -50 \leq y \leq 50, -10.4 \leq z \leq 0)$ and $(-100 \leq x \leq 0, -50 \leq y \leq 50, -15.3 \leq z \leq 0)$ were considered. The two different domain sizes analysed gives an estimate of the size of the domain on K_I . The domains are subject to uniform tension $\sigma_y = 1$ at $y = \pm 50$. A quarter-circular crack with centre at $(x = 0, y = 0, z = 0)$, a semi-circular crack with centre at $(x = -6.14, y = 0, z = 0)$ and at $(x = -12.36, y = 0, z = 0)$, respectively are analysed. Data for the quarter-circular crack are not given here but were used to verify data in databases DB1-DB4. The splitting scheme (used to create the five databases) is used in the analysis [1]. Crack dimensions for the eight semi-circular cracks considered are $a = c = 0.4, 0.9, 1.6, 2.5, 3.0, 4.0, 5.0$ and 6.0 respectively. Poisson's ratio $\nu = 0.0$ and $\nu = 0.3$ are considered since [8] provides many solutions for the case $\nu = 0.0$ but only one solution for $\nu = 0.3$. Polynomial orders $p=3-8$ are analysed in order to demonstrate that polynomial order $p=4$, used in the creation of the five databases is sufficient for a high accuracy in calculated K_I -solutions.

Tables 2-7 shows calculated values of the stress intensity factor $K_I(\varphi)$ for single cracks for polynomial order $p=4$ obtained using the splitting method for two different sizes of the global domain, different values of Poisson's ratio for single circular cracks at various locations $x=6.14$ and $x=12.36$. Right super index 'Left' denotes the point of local maximum K located most close to the vertex at $x = 0$, 'Middle' at the deepest point of the crack ($z = -c$) and 'Right' the point of local maximum K located most far away from the vertex $x = 0$.

Consider stress intensity factors for semi-circular cracks in a $\frac{1}{2}$ infinite and $\frac{1}{4}$ infinite domains. The Tables 4 and 5 shows that the stress intensity functions for a crack of size $a=c=0.4$ agrees with almost four digits irrespectively if the crack is located at $x=6.14$ or $x=12.36$. The same conclusion holds if we compares data for $a=c=0.4$ for the small and large domains. Hence we may conclude that the solution for $a=c=0.4$ is very close to the solution for a crack in the half-space.

With increasing value of a , the effect of the finite thickness and finite width on $K_I^{(Left)} / \sqrt{\pi \cdot a}$ is clearly visible. Note that the smallest domain analysed is only 24.0 wide and 10.4 thick wide so a semi-circular crack with $a=c=5$ means a significant reduction of the cross section area.

a=c	$K_I^{(Left)} / \sqrt{\pi \cdot a}$	$K_I^{(Middle)} / \sqrt{\pi \cdot a}$	$K_I^{(Right)} / \sqrt{\pi \cdot a}$
0.4	0.7666	0.6281	0.7666
0.9	0.7674	0.6286	0.7673
1.6	0.7712	0.6308	0.7703
2.5	0.7846	0.6371	0.7790
3.0	0.7978	0.6424	0.7851
4.0	0.8492	0.6580	0.8075
5.0	0.9688	0.6823	0.8416

Table 2 Calculated stress intensity values at three points at semi-circular crack front in the largest domain analysed (width 100.0, thickness 15.3) for $\nu = 0.0$, $p = 4$ and the crack centre located at $x=6.14$. The splitting scheme was used.

a=c	$K_I^{(Left)} / \sqrt{\pi \cdot a}$	$K_I^{(Middle)} / \sqrt{\pi \cdot a}$	$K_I^{(Right)} / \sqrt{\pi \cdot a}$
0.4	0.7665	0.6281	0.7665
0.9	0.7670	0.6284	0.7669
1.6	0.7687	0.6294	0.7686
2.5	0.7741	0.6324	0.7735
3.0	0.7776	0.6347	0.7763

Table 3 Calculated stress intensity values at three points at semi-circular crack front in the largest domain analysed (width 100.0, thickness 15.3) for $\nu = 0.0$, $p = 4$ and $x=12.36$. The splitting scheme is used.

A=c	$K_I^{(Left)} / \sqrt{\pi \cdot a}$	$K_I^{(Middle)} / \sqrt{\pi \cdot a}$	$K_I^{(Right)} / \sqrt{\pi \cdot a}$
0.4	0.7446	0.6519	0.7446
0.9	0.7454	0.6525	0.7453
1.6	0.7494	0.6550	0.7483
2.5	0.7628	0.6619	0.7565
3.0	0.7786	0.6681	0.7614
4.0	0.8309	0.6843	0.7821
5.0	0.9603	0.7114	0.8165

Table 4 Calculated stress intensity values at three points at semi-circular crack front in the largest domain analysed (width 100.0, thickness 15.3) for $\nu = 0.3$, $p = 4$ and the crack centre located at $x=6.14$. The splitting scheme was used.

a=c	$K_I^{(Left)} / \sqrt{\pi \cdot a}$	$K_I^{(Middle)} / \sqrt{\pi \cdot a}$	$K_I^{(Right)} / \sqrt{\pi \cdot a}$
0.4	0.7446	0.6518	0.7446
0.9	0.7449	0.6522	0.7449
1.6	0.7467	0.6535	0.7466
2.5	0.7517	0.6568	0.7511
3.0	0.7548	0.6596	0.7535

Table 5 Calculated stress intensity values at three points at semi-circular crack front in the largest domain analysed (width 100.0, thickness 15.3) for $\nu = 0.3$, $p = 4$ and $x=12.36$. The splitting scheme is used.

a=c	$K_I^{(Left)} / \sqrt{\pi \cdot a}$	$K_I^{(Middle)} / \sqrt{\pi \cdot a}$	$K_I^{(Right)} / \sqrt{\pi \cdot a}$
0.4	0.7448	0.6520	0.7448
0.9	0.7461	0.6529	0.7459
1.6	0.7529	0.6573	0.7516
2.5	0.7751	0.6685	0.7673
3.0	0.7991	0.6780	0.7790
4.0	0.8782	0.7017	0.8205
5.0	1.0618	0.7378	0.8830

Table 6 Calculated stress intensity values at three points at semi-circular crack front in the smallest domain analysed (width 24.0, thickness 10.4) for $\nu = 0.3$, $p = 4$ and the crack centre located at $x=6.14$. The splitting scheme was used.

$a=c$	$K_I^{(Left)} / \sqrt{\pi \cdot a}$	$K_I^{(Middle)} / \sqrt{\pi \cdot a}$	$K_I^{(Right)} / \sqrt{\pi \cdot a}$
0.4	0.7447	0.6519	0.7447
0.9	0.7456	0.6526	0.7456
1.6	0.7499	0.6556	0.7499
2.5	0.7618	0.6627	0.7620
3.0	0.7710	0.6684	0.7714

Table 7 Calculated stress intensity values at three points at semi-circular crack front in the smallest domain analysed (width 24.0, thickness 10.4) for $\nu = 0.3$, $p = 4$ and $x=12.36$. The splitting scheme was used.

Semi-circular crack close to a vertex: Data in Tables 4 and 6 shows that the stress intensity factors at the two vertices at the surface (vertex 'a') are identical, to 3-4 figures for $a=4$, while with increasing crack size a the stress intensity factor at the 'Left' surface vertex, closest to $x = 0$ increases faster than at the 'Right' vertex. The value of $K_I^{(Left)} / \sqrt{\pi \cdot a}$ increases slowly when c increases from 0.4 to 1.6 indicating that there is a slight dependence of nearby boundaries

Figure 62 shows $K_I(\varphi)$ for cracks of increasing size with centre at $x=6.14$ for $\nu = 0.3$. A comparison with data from [8] shows that data are conservative compared to data derived in the present work. This is especially pronounced near the two crack vertices where $K_I(\varphi)$ show very strong gradients. Figure 62 show that the high-accuracy methods used in the present work seems able to capture the near-vertex behaviour, including the fast decrease to $K_I = 0$ at the two vertices.

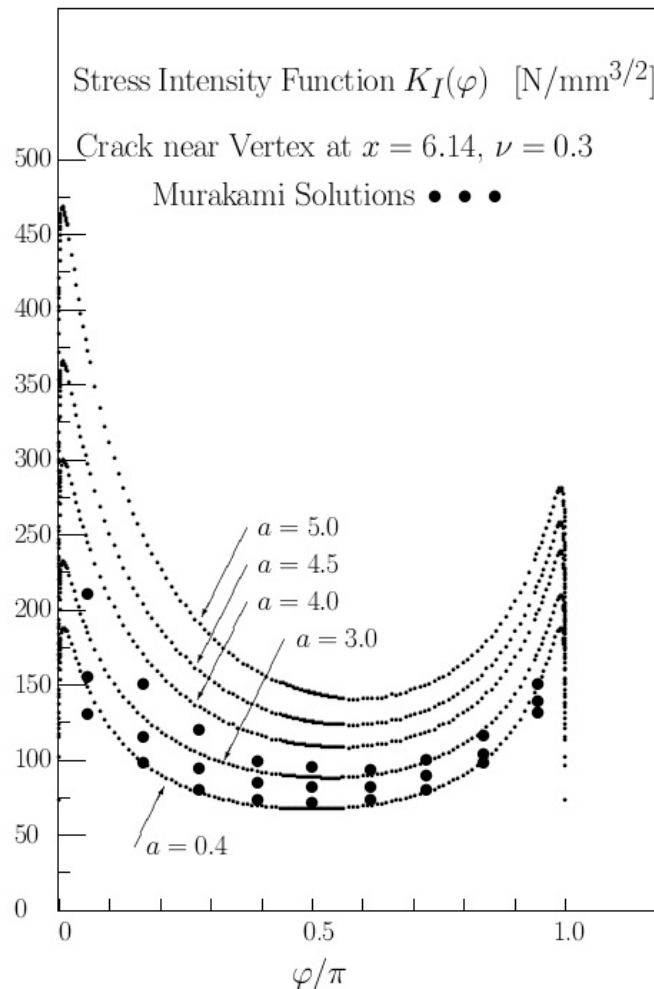


Figure 62 Stress intensity functions for cracks close to a free edge

Direct calculation of stress intensity factors using very accurate FE-solutions: The multi-scale method (splitting method) is used to derive the 10^{35} solutions. The accuracy of the splitting scheme has to be verified too. The basic definition of the mode I stress intensity factor K_I was used together with high-accuracy FE-solutions to verify that calculated stress intensity factors might be correct with 3-4 digits accuracy.

Again, consider a (small) block-shaped domain with a symmetrically located central surface crack. The computational domain has a circular surface crack with $a=c=100$. The dimensions of the domain are $544 \times 1088 \times 1223$ units (i.e. different than the two model domains used above). Poisson's ratio is 0.3. Boundary conditions correspond to uniform y -displacements on the two ends $y = \pm 544$ that corresponding to uniform tractions $\sigma_y = 5/2$ for the un-cracked domain. This displacement boundary condition corresponds approximately to a uniform stress also for the case when there is a crack in the domain (the stress σ_y at the surfaces $y = \pm 544$ varies with less than 1% from the value $5/2$). The mesh used in the analysis is of the same fineness as used in the analysis of the five databases.

Table 8 shows (for reference) calculated values of the stress intensity factors obtained with the splitting scheme close to the vertices (maximum values) and at the deepest point of the crack.

Polynomial order p	$K_I^{(a)}$	$K_I^{(c)}$
2	26.49	23.24
4	26.60	23.31

Table 8 Calculated stress intensity factors near vertex 'a', and at deepest point 'c' for a semi-circular surface crack with $a=c=100$.

The stress intensity factors K_I were, as mentioned calculated from its definition,

$$\tilde{K}_I = \lim_{\delta \rightarrow 0} \sigma_y \cdot \sqrt{2 \cdot \pi \cdot \delta} \quad (10)$$

In 10, δ is the distance to the crack front. In the set of finite element analyses performed finite elements with up to 192 nodes per element ($p = 8$) were used. Table 9 shows calculated values of \tilde{K}_I from (6) for various δ and polynomial orders p of the finite elements used at the deepest point of the crack (point 'c').

Distance δ	$\tilde{K}_I(\delta, p = 4)$	$\tilde{K}_I(\delta, p = 6)$	$\tilde{K}_I(\delta, p = 8)$
0.001	17.44	24.96	22.26
0.002	23.07	23.36	22.97
0.003	22.49	23.21	23.40
0.004	22.95	23.00	23.07
0.005	23.16	23.25	23.29
0.006	23.10	23.27	23.29
0.007	23.09	23.30	23.28
0.008	23.13	23.31	23.28
0.009	23.31	23.31	23.28
0.010	23.31	23.29	23.28
0.020	23.37	23.39	23.32
0.030	23.24	23.29	23.31
0.040	23.25	23.30	23.32
0.050	23.21	23.32	23.32
0.060	23.23	23.33	23.33
0.070	23.32	23.34	23.33
0.080	23.38	23.34	23.34
0.090	23.41	23.35	23.34
0.100	23.51	23.36	23.35

Table 9 Calculated stress intensity factor values from the definition of K_I (equation 10) using finite elements with 50, 105 and 192 nodes/element, respectively.

The conclusion is that the extracted stress intensity factor, $K_I = 23.31$ at point 'c' for $p=4$, Table 8 agree with 3-4 digits with data in Table 9.

Since finite element meshes of the fineness used in this example are always together with polynomial orders $p=4$ were always used to derive solutions for the five databases, it can be tentatively concluded that computed stress intensity factor data in the databases are very accurate.

Verification of K for small crack data for single $\frac{1}{2}$ -elliptical cracks: The five data databases contain K_I -data for a quite large number of crack size a - c combinations. Table 10 shows the number of crack dimensions in the data bases. In sections 6-8 stress intensity factors for all the a - c combinations for all crack locations x in all databases, totally 10384 cracks are in principle verified.

Database	x -loc. 1	x -loc. 2	x -loc. 3	x -loc. 4	x -loc. 5	x -loc. 6
DB1	287	147	255	287	271	202
DB2	313	166	268	313	313	252
DB3	287	165	255	287	287	255
DB4	162	245	274	260	180	-
DB5	266	164	240	266	266	240

Table 10 Number of unique a/c values considered at each x -location in the databases. Note that for DB1 there are three rows of cracks with the same number of cracks at each row.

Figure 54 shows the a - c combinations available in databases.

Figure 63 compares stress intensity factors for corner cracks from [8] with results from databases DB1 (crack row 0 and 1), DB2 (crack row 1 and 2) and DB3 respectively. The agreement is excellent for all small cracks ($a=c=0.1$ mm). The errors increase to 5-7% for larger cracks. The discrepancy is partly due to the accuracy of the solutions given in [8] and partly due to difference in geometries and stress distributions (Figure 50).

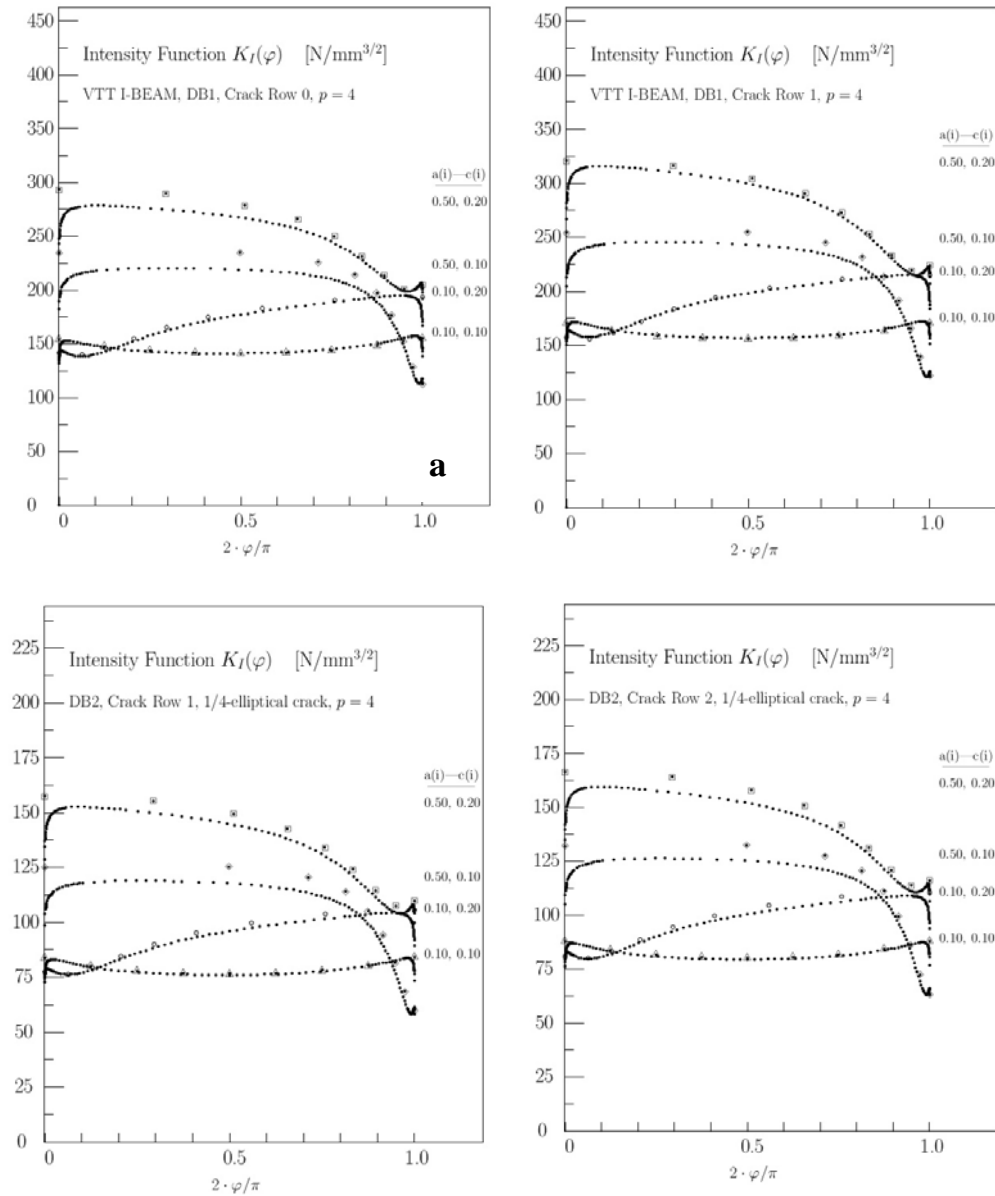


Figure 63 **a** Comparison of calculated $K_I(\varphi)$ with data in [8] for $1/4$ -crack in crack row 0 (Figure 67) in database DB1, **b** Comparison of calculated $K_I(\varphi)$ with data in [8] for $1/4$ -crack in crack row 1 (Figure 67) in database DB1, **c** Comparison of calculated $K_I(\varphi)$ with data in [8] for $1/4$ -crack in crack row 1 (the single corner crack) in database DB2, **d** Comparison of calculated $K_I(\varphi)$ with data in [8] for $1/4$ -crack in crack row 2 (containing 6 cracks) in database DB2

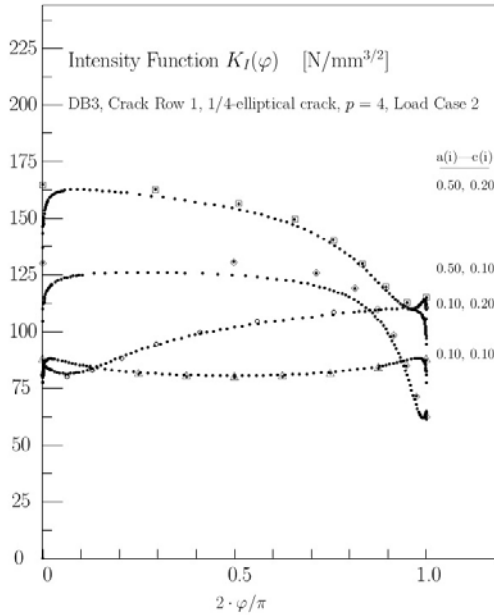


Figure 63e Comparison of calculated $K_I(\varphi)$ with data in [8] for $1/4$ -crack in database DB3

Verification of small crack data for single $1/2$ -elliptical cracks: Consider the stress intensity factor K_{IC} at the deepest point on a crack front for a semi-elliptical surface crack in a plate subject to tension and bending stresses σ_T and σ_B , respectively. For $a/c > 1.3-1.5$ roughly, the stress intensity function K_{IC} has its maximum value at this point.

An empirical formula based on numerical results from ([8], page 699), defined by equations 11-13, was used in the verification procedure.

$$K_{IC} = (\sigma_T \cdot F_C^{(T)} + \sigma_B \cdot F_C^{(B)}) \cdot \sqrt{\pi \cdot c} \quad (11)$$

$$\begin{aligned} F_C^{(T)} = & 1.1362 - 0.3927 \cdot \mu - 0.3450 \cdot \mu^2 + 0.2623 \cdot \mu^3 \\ & + \lambda \cdot (-0.2179 + 0.2354 \cdot \mu + 0.3773 \cdot \mu^2 - 0.4189 \cdot \mu^3) \\ & + \lambda^2 \cdot (5.0486 - 16.7973 \cdot \mu + 19.986 \cdot \mu^2 - 8.0212 \cdot \mu^3) \\ & + \lambda^3 \cdot (-2.6383 + 8.6007 \cdot \mu - 9.6332 \cdot \mu^2 + 3.5118 \cdot \mu^3) \end{aligned} \quad (12)$$

$$\begin{aligned} F_B^{(T)} = & 1.1359 - 0.3929 \cdot \mu - 0.3440 \cdot \mu^2 + 0.2613 \cdot \mu^3 \\ & + \lambda \cdot (-1.5184 + 0.4178 \cdot \mu + 0.7846 \cdot \mu^2 - 0.6329 \cdot \mu^3) \\ & + \lambda^2 \cdot (4.3721 - 13.9152 \cdot \mu + 16.2550 \cdot \mu^2 - 6.4894 \cdot \mu^3) \\ & + \lambda^3 \cdot (-3.9502 + 12.5334 \cdot \mu - 14.6137 \cdot \mu^2 + 5.8110 \cdot \mu^3) \end{aligned} \quad (13)$$

Where $\mu = c/a$ and $\lambda = c/t$, t being the thickness. The empirical formulas are claimed to be valid for $\nu = 0.3$, $0.125 \leq \mu \leq 0.1$ and $\lambda \leq 0.6$ and gives stress intensity values at the point 'C' with an estimated relative error less than 1%.

Results from 11-13 were compared with results for c small ($c \leq 1.0$ mm) and semi-elliptical single cracks obtained from database DB1. Detailed results will be given for a single crack located at $x = 9.24$ mm.

Table 11 shows calculated stresses ($p=6$ solution) σ_y in MPa at different distances z from the free surface in the I-beam, DB1. Table 11 shows that the maximum surface stress is 398.3 MPa and the average stress gradient in the z -direction is -23.6 MPa/mm close to the surface. Since the flange thickness is about 8 mm we will in the comparison with 11-13 consider an equivalent linear stress field $\sigma_T = 303.9$ MPa and $\sigma_B = 94.4$ MPa, in agreement with the calculated maximum stress and the stress gradient over an 8.0 mm thick plate. This is of course an approximation both with respect to the geometry and the stress state in the I-beam.

$Z(mm)$	0.0	0.5	1.0	2.0	3.0	4.0	5.0
$\sigma_y(MPa)$	398.3	385.7	374.7	355.8	338.7	321.0	299.9

Table 11 Stress at flange surface as function of distance z from free surface in crack row 1

The stress intensity factor at the deepest point was calculated from database DB1 for crack row 1 and from 11-13 for $a/c \geq 1.0$. Table 12 shows the relative difference in % in calculated stress intensity factor K_{IC} at point C obtained with the analytical expression and from database DB1. The table shows that the relative difference is about 1 % between the solutions for the quite large a/c range given. For the largest crack considered in Table 12, that is 16 mm long and 1 mm deep, i.e. $a=8.0$ mm and $c=1$ mm there is a considerable (compared to a relative error of 1% in the x -direction) stress variation with x .

Since the accuracy of the analytical expression 11-13 is claimed to be about 1% in reference [8] the conclusion is that data derived from DB1 and the software PROG is accurate in the a - and c -range where a comparison is meaningful ($c \leq 1.0$ mm due to the non-uniform stress distribution). This fact will be used in the fatigue module when deriving stress intensity factors for very small cracks. Note that the stress intensity factor increase for cracks located near the flange end (i.e. x small that is $1 \leq x/a \leq 2$) this explains the somewhat larger error observed for cracks with x/a close to 1.

	$c=0.1$	$c=0.2$	$c=0.3$	$C=0.4$	$c=0.5$	$c=0.6$	$C=0.8$	$C=1.0$
$a/c=1.0$								
$a/c=2.0$	1.4	1.3	1.3	1.3	1.3	1.3	1.3	1.2
$a/c=3.0$	1.1	1.0	-	1.1	-	1.1	1.1	1.2
$a/c=4.0$	1.0	0.9	0.9	0.9	0.9	1.0	-	0.8
$a/c=5.0$	0.9	0.9	-	0.9	-	1.0	1.0	1.5
$a/c=6.0$	1.0	0.9	0.9	1.0	1.1	-	-	1.5
$a/c=7.0$	-	1.1	-	-	1.0	-	-	1.7
$a/c=8.0$	1.2	1.2	1.2	-	1.1	-	-	1.9

Table 12 Relative difference in % in calculated stress intensity factor K_{IC} at deepest point C of semi-elliptical crack at location $x=9.24$ mm in crack row 1. The c -values given in the table are in mm.

Figure 64 compares stress intensity factors for $1/2$ -elliptical cracks from [8] with results from databases DB1 (crack row 1 and 0), DB2 (crack row 1), DB3 and DB4 respectively. The agreement is excellent for all small cracks ($a=c=0.1$ mm). The errors increase to up to 7% for larger cracks. The discrepancy is partly due to the accuracy of the solutions given in [8] and partly due to difference in geometries and complex stress distributions (Figure 50).

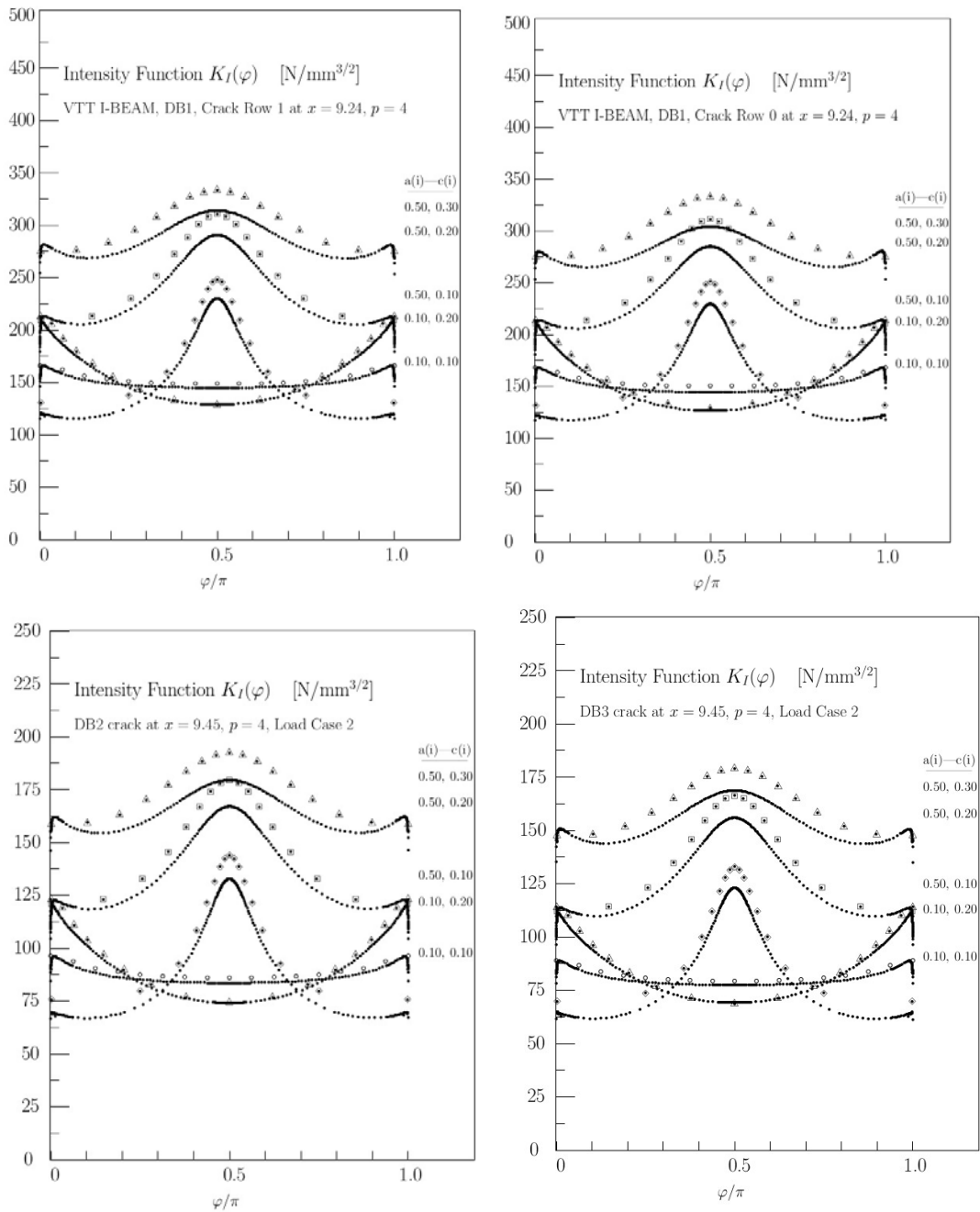


Figure 64 **a** Comparison of calculated $K_I(\varphi)$ with data in [8] for 1/2-crack in row 1 (Figure 67) in data.base DB1. **b** Comparison of calculated $K_I(\varphi)$ with data in [8] for 1/2-crack in row 0 (Figure 67) in database DB1. **c** Comparison of calculated $K_I(\varphi)$ with data in [8] for 1/2-crack in database DB2. **d** Comparison of calculated $K_I(\varphi)$ with data in [8] for 1/2-crack in database DB3

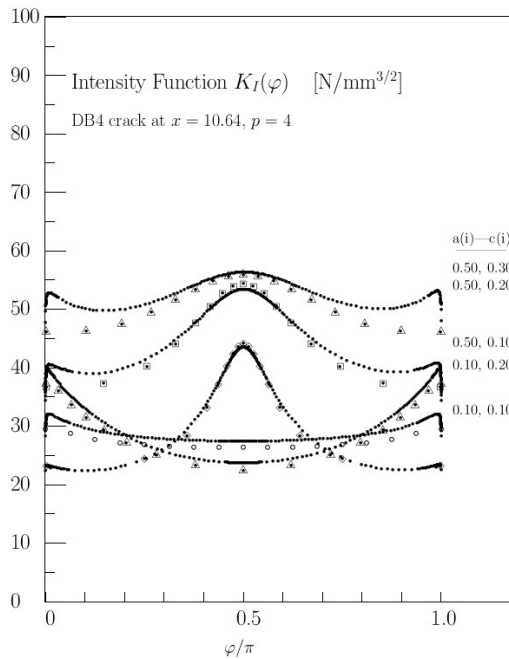


Figure 64e Comparison of calculated $K_I(\varphi)$ with data in [8] for 1/2-crack in database DB4

Another soundness test of data bases, which can be performed for $\frac{1}{2}$ elliptical cracks with little manual labour is to scale $K_I(\varphi)$ -distributions for smaller cracks with the local stress to get normalised distributions which can be easily compared. Figure 65 exemplify normalised $K_I(\varphi)$ -distributions for cracks in rows 1 and 0 in DB1, and row 1 in DB3 for cracks at various x -locations. Curves are plotted with a scale factor β where,

$$\beta = \sigma_Y(x = 9.24, z = 0) / \sigma_Y(x = x^*, z = 0) \quad (14)$$

for DB1 for example (see also figure captions in Figure 65).

Tables 13-15 shows the calculated local stress $\sigma_Y(x^*, z = 0)$ used to create the totally 120 graphs in figure 65.

The graphs show that the K_I -curves cluster well in groups, that is the $K_I(\varphi)$ -distributions are almost independent of the x -location (i.e. after proper scaling with the local maximum stress $\sigma_Y(x^*)$).

x^* -coord.	0.0	3.09	6.14	9.24	12.36	15.43
Row 0	379.8	406.2	406.5	407.2	408.6	410.9
Row 1	413.3	408.7	402.0	398.3	396.2	394.3
Row 2	379.3	405.9	406.2	406.9	408.4	410.7

Table 13 Calculated surface stress σ_Y [MPa] at 18 different locations in DB1

x^* -coord.	0.0	3.15	6.30	9.45	12.60	15.75
Row	209.8	222.9	225.7	227.5	228.6	228.1

Table 14 Calculated surface stress σ_Y [MPa] at different locations in DB2

x^* -coord.	0.0	3.24	6.49	9.73	12.97	16.21
Row	211.7	213.1	213.3	212.6	210.9	208.6

Table 15 Calculated surface stress σ_Y [MPa] at different locations in DB3

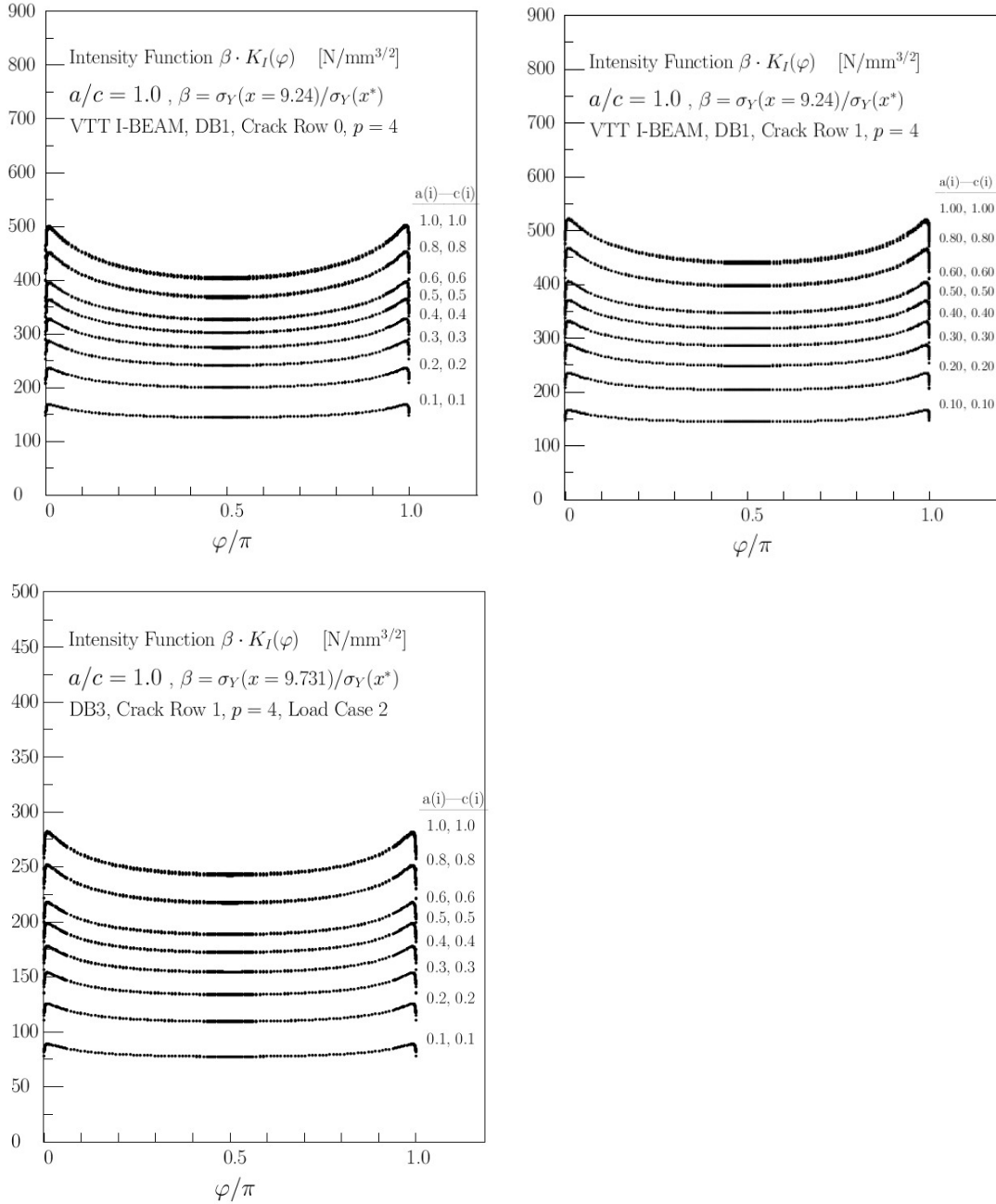


Figure 65 **a** Calculated $K_I(\varphi)$ -distributions for small cracks in row 1 scaled with factor $\sigma_Y(x = 9.24, z = 0)/\sigma_Y(x^*, z = 0)$ for $a/c = 1.0$ and for all semi-elliptical cracks in crack row 1 having $c \leq 1.0$ mm. **b** Calculated $K_I(\varphi)$ -distributions scaled with factor $\sigma_Y(x = 9.24)/\sigma_Y(x^*)$ for $a/c = 1.0$ and for all semi-elliptical cracks in crack row 0 for $c \leq 1.0$ mm. **c** Calculated $K_I(\varphi)$ -distributions scaled with factor $\sigma_Y(x = 9.731)/\sigma_Y(x^*)$ for $a/c = 1.0$ and for all semi-elliptical cracks in crack row 1 for $c \leq 1.0$ mm. Totally 40 graphs are shown in each of the three figures.

To this end, the verification of 10^{35} .multiple-site site fracture mechanics solutions is a challenging task. The six-step scheme use to verify the solution accuracy has briefly been reviewed above although the review of the

work performed is far from exhaustive. The state of the art methods used, ie *hp*-FEM and the splitting scheme is critical parts in obtaining very high accuracy and negligible computer cost per stress intensity factor solution.

3.4.4 Validation of Multiple-site Fatigue Crack Growth Analysis Method

Simplified validation procedures are executed below for the crack growth method based on the advanced fatigue crack growth model and the high accuracy stress intensity factor solutions for MSD problems when several fatigue cracks are initiated at critical areas close to each other. The experimental data used are those reported in [4] and references therein. There are promising indications that the method can reliably simulate fatigue crack growth behaviors in complex MSD scenario.

The fatigue crack growth prediction method presented and the accurate stress intensity factor solutions presented are validated based on the experiments performed using a laboratory specimen, a so-called I-Beam specimen, see figure 67, [4]. The validation shows a general good agreement between the MSD fatigue crack growth analyses and the experimental data.

In addition, the MSD analyses discussed below uncover a number of serious issues that can be easily ignored in the fatigue tests.

The measured strains are compared to the finite element computations in figure 66 [4]. Generally, the finite element results are in good agreement with the measured values, with the maximum difference within a few percent. Geometrically non-linear analyses give an even better agreement to the measured values.

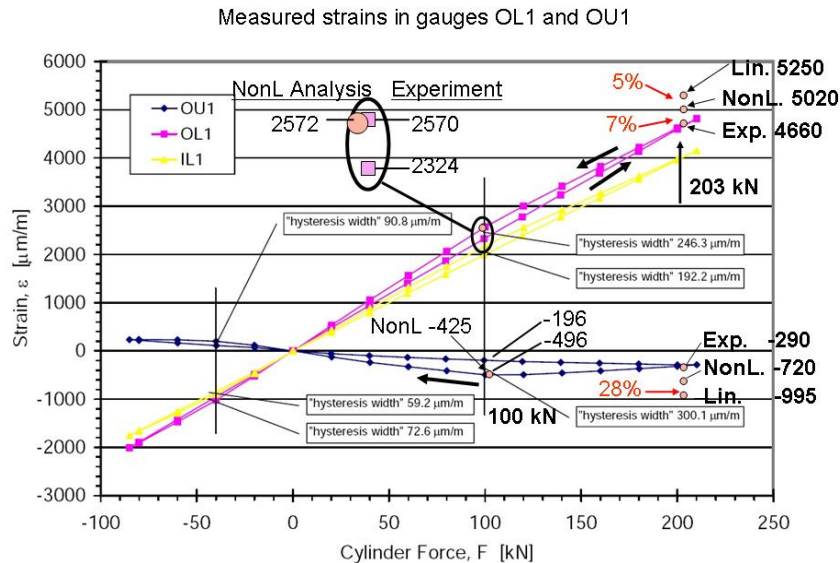


Figure 66: Comparison of strain results to the finite element result, see [4] and references therein

The good agreement between the finite element results and the strain gauge measurements gives a good confidence in using the finite element mesh and the boundary conditions to create the stress intensity factor data base for analyses of the multiple crack initiation and propagation. The finite element stress analyses show that the stresses near the toe of the stiffeners and on the bottom surface of the stiffener are rather close to each other as the result in figure 67 shows. The solution has been obtained with the *p*-version of the finite element method for polynomial order $p=4$ and can be considered to be the exact mathematical solution. In large areas along the toe of the stiffener and on the bottom of the stiffener, the stress is almost uniformly distributed. Such condition gives a high multiple site crack initiation probability. In this case, it will be necessary to consider the effect of multiple site fatigue crack initiation and propagation.

Accordingly, a database has been created using the highly accurate *hp*-version of finite element solution [4] for multiple cracks located on three sections along the stress concentration locations at the toe of the stiffeners and the bottom of the stiffener, see the illustration as shown in figure 67. On each section, stress intensity factor

solutions for up to as many as six cracks are considered, see the right hand side of figure 67. It is considered, according to the fatigue test results, these crack number will cover most of the application ranges.

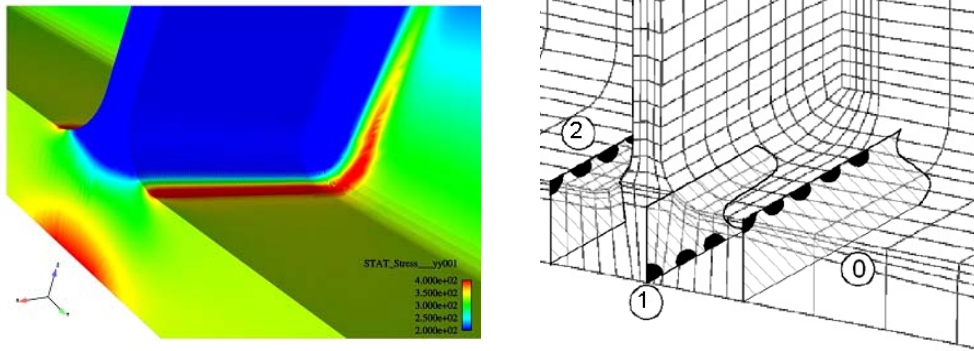


Figure 67. Locations of the multiple cracks in the data base of I-Beam

The validation will start with the analysis of the MSD growth behaviour, compared to the single crack behaviour. The first case as shown in insert of figure 68 will be considered in details [4]. This test results in a fracture surface MSD pattern as shown in figure 68. According to the dimensions as defined in figure 68, predictions of fatigue crack growth are performed. With some trial-and-try, the initial crack sizes of $a_0 = 53\mu\text{m}$ and $c_0 = 52\mu\text{m}$ for the first crack, $a_0 = 45\mu\text{m}$ and $c_0 = 45\mu\text{m}$ for the second crack, and $a_0 = 35.1\mu\text{m}$ and $c_0 = 35.05\mu\text{m}$ for the third crack, see the illustration as shown in figure 63, give the closest match for the crack pattern as observed in the experiment (see [4] and references therein). The crack pattern and the corresponding fatigue crack growth for each crack are shown in the figure.

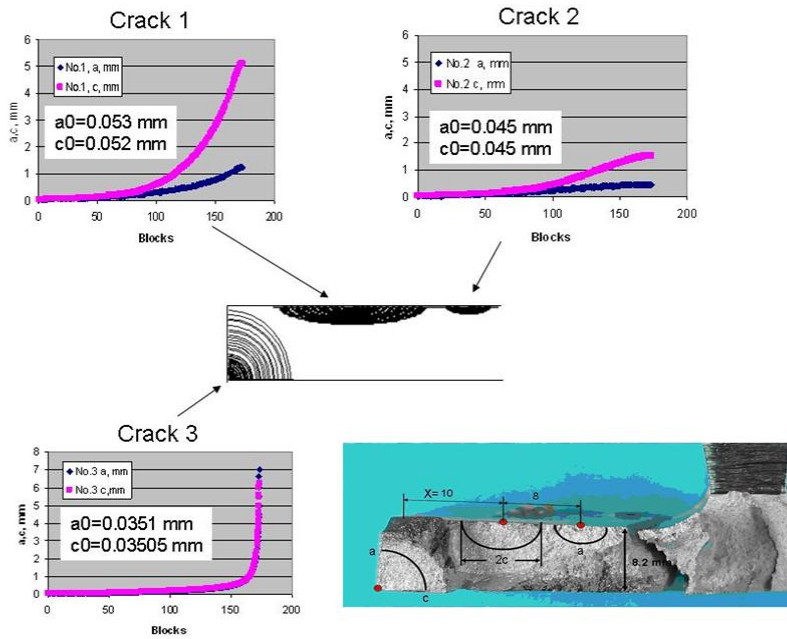


Figure 68: MSD fatigue crack growth prediction according to the present model.

In order to achieve an even better agreement with the test results other initial crack sizes are tried. After some trial-and-try, it is found that initial crack sizes of $a_0 = 95\mu\text{m}$ and $c_0 = 90\mu\text{m}$ for Crack 1, $a_0 = 92\mu\text{m}$ and

$c_0 = 91\mu m$ for Crack 2, and $a_0 = 60\mu m$ and $c_0 = 61\mu m$ for Crack 3 will result in better predictions of the fatigue crack growth for I-Beams. These initial crack sizes will give a perfect match to the experimental data.

The linear prediction according to the new initial crack sizes is shown in figure 69 for the size of the cracks as a function of the load blocks. After a 10% reduction in the fatigue life according to the full strip yield analysis to account for both the small crack and load interaction effect, the prediction will result in similar fatigue life as the experimental data.

This prediction gives 25% shorter fatigue life with an increase in the crack size of 3 times for Crack 1, 4 times for Crack 2, and 2.9 times for Crack 3. In MSD case, the pattern of the crack seems to be very much more important than the size of the initial crack.

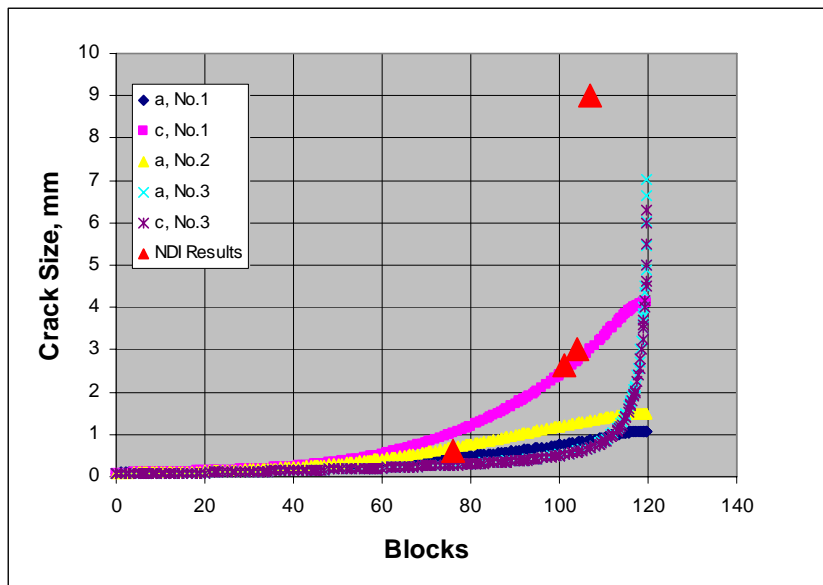


Figure 69: Predicted fatigue crack growth with increased initial crack sizes.

Since the pattern of MSD may affect predictions of the fatigue crack growth, the other experimental results are investigated for the purpose of validation of the crack growth prediction software and to better understand these observed behaviours

For the second fatigue test [4], the fracture surface is shown in figure 70. For this test, two surface cracks are initiated on both inside of the central beam. The limitation in the database DB1 allows only 1-6 cracks on either side of the vertical flange to be considered. Due to the undamaged vertical flange, the fatigue crack will have minimal effect on each other and the crack growth may be analysed independent of each other. In this case, only the largest crack on the left hand side as shown in figure 70 is considered.

Based on the output of the maximum crack size and the stress intensity factor from the prediction, the linear and closure analysis are compared and the results are compared on the right hand side in figure 70. Again in this case, the closure analysis shows slower crack growth rate than the linear analysis. The initial crack growth is faster. For this particular crack pattern, the closure analysis shows however longer fatigue life when the crack size becomes larger than 2.5 mm. This may be due to the surface type of single crack which usually induces higher general crack closure effect which may overcome the detrimental acceleration effect of the spectrum loading.

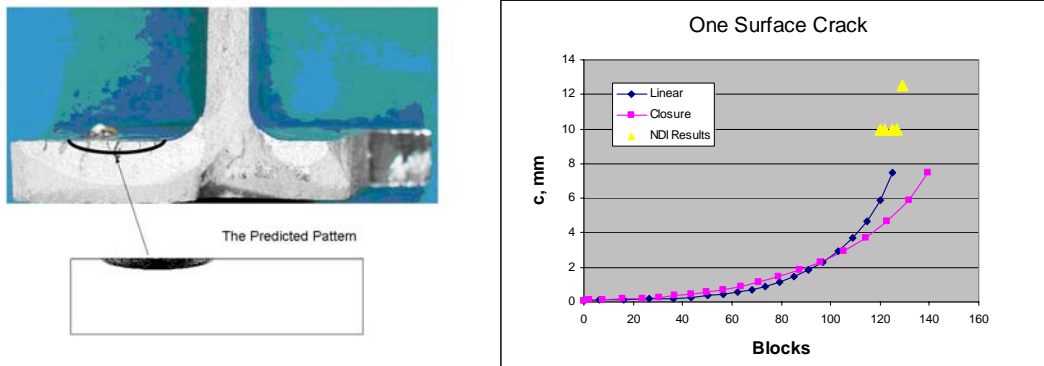


Figure 70: comparison MSD pattern and crack growth results of Test 2 (see [4] and references therein)

For fatigue Test 3, [4], the close-up of fracture MSD pattern is shown in figure 71. In this case, two initial major surface cracks can be identified as shown in the figure. One of the surface cracks is rather close to the edge of specimen. It gradually grows into a shallow corner crack in the later stage of fatigue life.

Again, the prediction is performed using the assumed initial cracks for $a_0 = 95\mu\text{m}$ and $c_0 = 95\mu\text{m}$ for Crack 1 and $a_0 = 95\mu\text{m}$ and $c_0 = 945\mu\text{m}$ for Crack 2, located at 7 mm and 15 mm respectively from the edge. The predicted pattern of MSD is shown in the bottom of figure 71, indicating some immigration of the surface crack into a corner crack in the prediction.

The predicted fatigue crack growth as a function of the load blocks is shown on the right hand side in figure 71. In this result, there is a jump for Crack 1 that is caused by the change of surface crack to the corner crack by definition. The surface crack has a surface size of $2c$ while the corner crack has a surface size of c .

As for the case of single surface crack for Test 2, the crack growth belongs to the slow crack growth type while the increase in crack size is gradual both along the surface and in the thickness direction, even though the crack growth on the surface is much faster than the crack growth in the thickness direction, perhaps due to the large stress gradient in the thickness direction. A slightly increased crack growth rate may be observed when the surface crack becomes a corner crack.

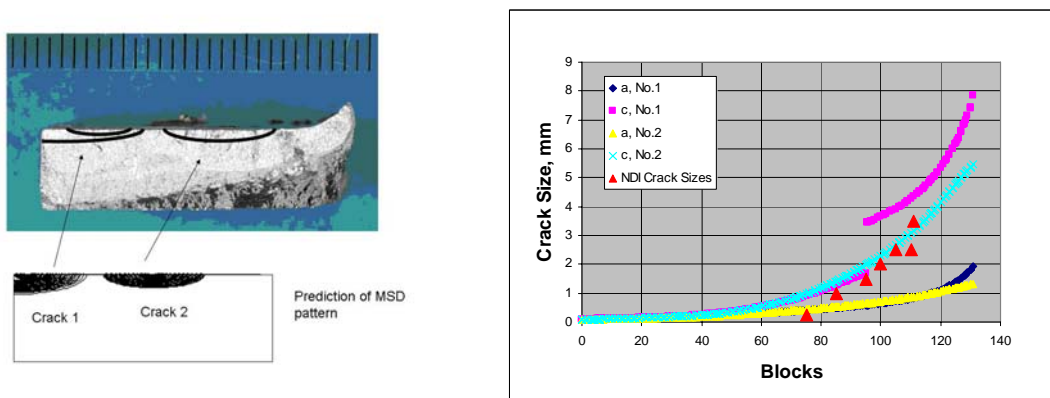


Figure 71: comparison MSD pattern and crack growth results of Test 3 (see [4] and references therein)

For Test 3 as shown in figure 72 left side, there are actually many more cracks involved than the two analysed above. It is therefore of interest to perform an analysis where all cracks are considered. In figure 72, the general test MSD pattern is shown [4]. In this case, three layers of cracks may be considered according to the stress intensity factor database as shown in figure 62.

Accordingly, cracks are defined in the three layers as shown in figure 62 with various definitions of crack numbers. For all the cracks, the initial size is assumed to be $a_0 = 95\mu\text{m}$ and $c_0 = 95\mu\text{m}$ for crack No.1, $a_0 = 95\mu\text{m}$ and $c_0 = 95\mu\text{m}$ for crack No.2, $a_0 = 55.3\mu\text{m}$ and $c_0 = 55.3\mu\text{m}$ for crack No.3, and $a_0 = 95\mu\text{m}$ and $c_0 = 95\mu\text{m}$ for crack No.4. These initial crack sizes are similar to those used in all the test cases.

The predicted crack growth is shown on the right hand side in figure 72 for all the cracks involved in the computation. In this prediction, crack No.2, a surface crack, becomes the fastest growing crack on the surface of I-Beam specimen. The predicted pattern is shown on the left hand side in figure 72.

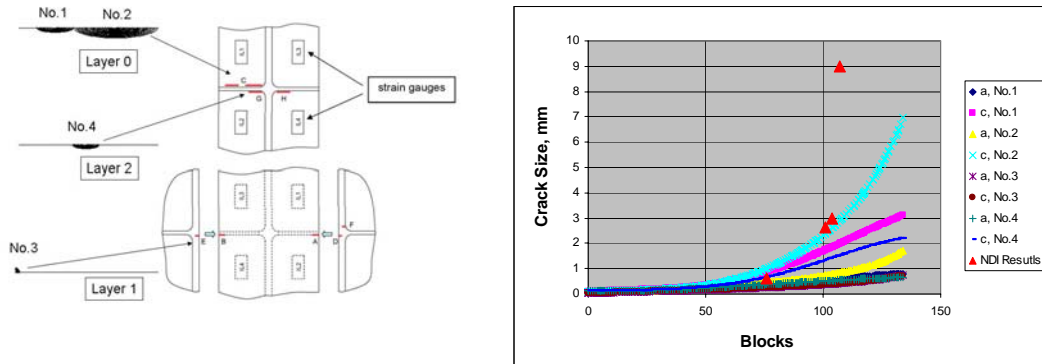


Figure 72: comparison MSD pattern and crack growth results (see [4] and results therein)

For MSD patterns observed for all the three test I-Beam items [4], the predicted fatigue lives are compared at a point when the maximum stress intensity factor is $20\text{MPa}\sqrt{\text{m}}$. At this stress intensity, more than 95% of fatigue life has been consumed. A comparison of all the MSD patterns has been made. As for the experimental results, the predictions show small scatter between the patterns when initial flaw size in the order of $95\mu\text{m}$ on the surface and $50 \sim 60\mu\text{m}$ on the critical corner are considered. The average of the fatigue lives indicates a life of around 125 blocks that is slightly longer than the test results. This overestimation of fatigue life may be partly compensated by considering the full crack closure solution which shows generally about 10% less fatigue life. The modification gives an average life of 115 blocks which is close to the experimental results.

The simulations of MSD reveal several alarming issues about the behavior of the MSD. Among them, the important ones are listed below.

- 1 Fractographic inspections of fracture surface may indicate SLOWER crack growth rate in some critical cases, that could lead to catastrophic service inspection intervals when the inspection is based on such fractographic results
- 2 Large cracks fatigue cracks that are initiated during the service may not be the critical ones. Much smaller cracks that are located at more critical area can outrun the larger cracks and lead to structural failure
- 3 Fatigue is not as sensitive to the absolute size of individual flaw as could be expected according to conventional methods. The location of initial flaws, on the other hand, may be more critical.
- 4 The developed MSD crack growth analysis package in the project seems tentatively be capable to account for many of the crack growth behaviours observed and with good confidence.

To conclude, it seems necessary to carry out true MSD analysis for critical structural details so that correct decisions can be made in order to evaluate the remaining life of a structural part and to define proper inspection strategies.

It is however important to point out that the tentative conclusions above are based on a rather limited test campaign for one type of specimen [4].

3.4.5 Multiple Site Fatigue Crack Growth Analysis of a few Sample Domains

Based on development of a fatigue crack growth analysis model, the high accuracy MSD stress intensity factor solutions, the simplified validations performed above, the methodology is below applied to a few sample domains (Figure 50) in order to try to quantify effects of multi-site damage. Loads are calculated from simple boundary conditions which are assumed to give realistic stress distributions for fuselage structures of complex geometry. Loads magnitudes are selected such that maximum stresses are of order 200-400 MPa (see Tables 13-15).

In this chapter the methods briefly reviewed above are used for crack growth predictions. A generic fighter load spectra have been used when analysing various MSD-scenario in the various sample parts. Consider first the model domain shown in Figure 73. Accurate stress distributions obtained using the *hp*-version of the finite element method reveal that there are many regions of high and uniform stresses extending over long distances. One critical area is located at the fillet between the flange and the stiffener. The other critical area is on the surface inside the fuselage etc etc. The first area investigated is named after DB2 for MSD stress intensity factor database, and the second area is named DB3. These areas are shown in figure 73. Additional areas require an analysis but is left out here.

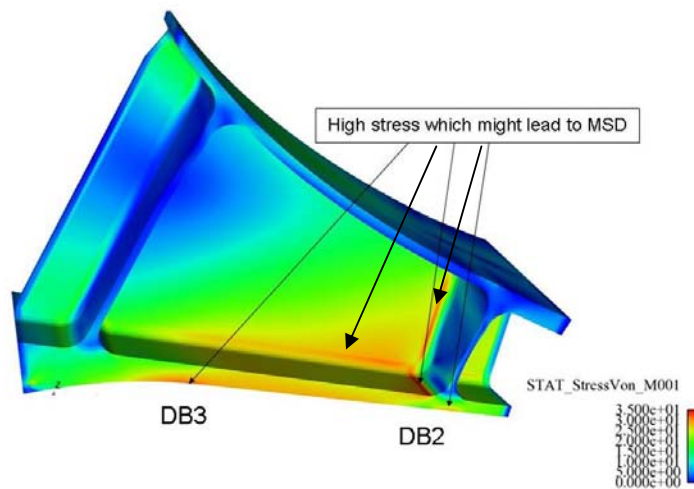


Figure 73: High accuracy finite element results showing the calculated maximum principle stress distributions

Load spectrum: To retrieve useful fatigue load data from the generic fighter load spectrum used which contains huge amounts of original data, the fatigue and fracture mechanics aspects are considered. To this end a concept of intrinsic fatigue crack growth threshold is applied. The intrinsic fatigue crack growth threshold is the crack growth threshold when the crack closure effect is considered. The intrinsic threshold value is the fatigue test threshold value for high stress ratio tests under which the crack closure effect is negligible. According to the fatigue crack growth parameter, an intrinsic threshold value of $K_T = 0.89 \text{ MPa}\sqrt{m}$ can be obtained. This is the threshold value for high stress ratio used. A filter was designed to ignore all the strain cycles in the spectrum that will create stress intensity factor range less than the intrinsic fatigue crack growth threshold. This filter is dependent on the strain level, the material property, and the crack sizes in the MSD scenario.

Using this filter technique on the original spectrum data, new load spectra are created for the fatigue crack growth analysis. For example, for the original generic spectrum consisted of over a million turning points. The simplified spectrum contains only a few hundred turning points for the filter for a threshold crack size of 0.1 mm. Even for a larger threshold crack size of 0.5 mm, the number of turning points is still rather moderate, to be a few thousand. The new spectra after the filtering is shown in figure 74 in blue color for the filter with maximum crack size of 0.1 mm and with purple color the one for the maximum crack size of 0.5 mm

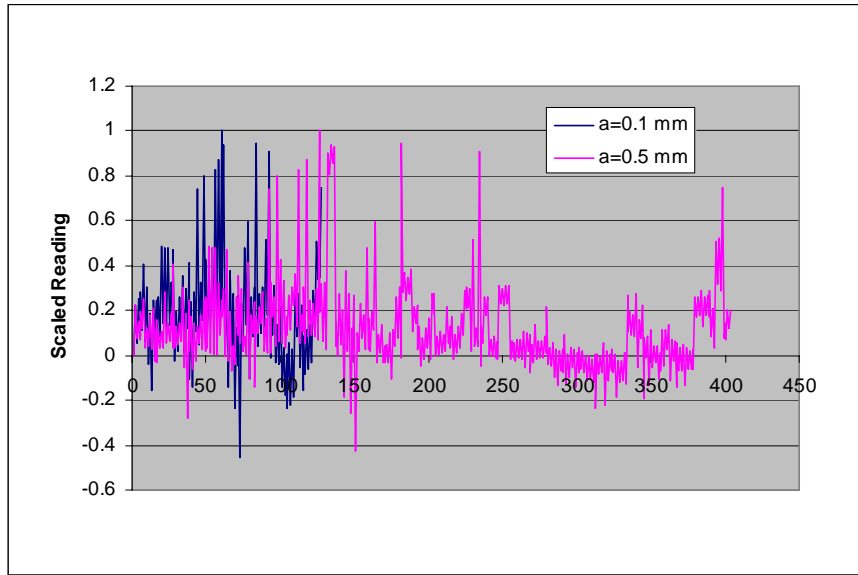


Figure 74: Comparison of filtered generic fighter load spectrum with filter being 0.1 mm maximum crack size (blue) and 0.5 mm maximum crack size (purple), respectively.

The simple manoeuvre shown in figure 75, efforts is used to generalise the solution and to expand the databases into load cases that are not included in the basic solutions so that the average single load spectrum used for the I-Beam tests may be used for the predictions of MSD issues for the samples DB2-DB4.

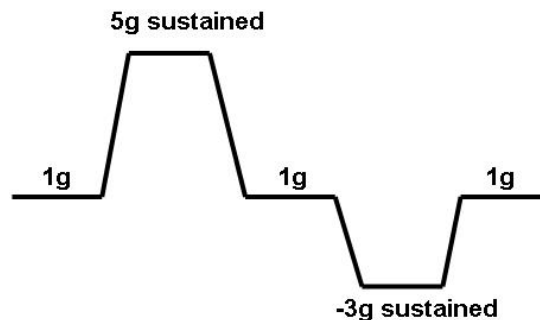


Figure 75: Demonstration example of mission segment

The mission segment shown in figure 75 consists of a normal 1g flight followed by a 5g sustained pull. The pull is recovered to the normal 1g flight before a -3g sustained pushdown is performed. The flight is then recovered to the normal 1g flight. The purpose for the prediction is to find out how many of such flights may be performed before the fatigue crack at the critical locations becomes detectable.

Data Base DB2: The sample bulkhead shown in figure 76 (and 73) reveals several stress critical locations. One of the locations, the high stress area at the fillet forms the so-called DB2 database (sections $y0$ and $y1$), for multiple site fatigue cracks. For database DB2, a row of multiple cracks are considered along the high stressed area $y1$ (the x direction). This database DB2 is implemented with a single corner crack too ($y0$) considered at the bottom of the flange.

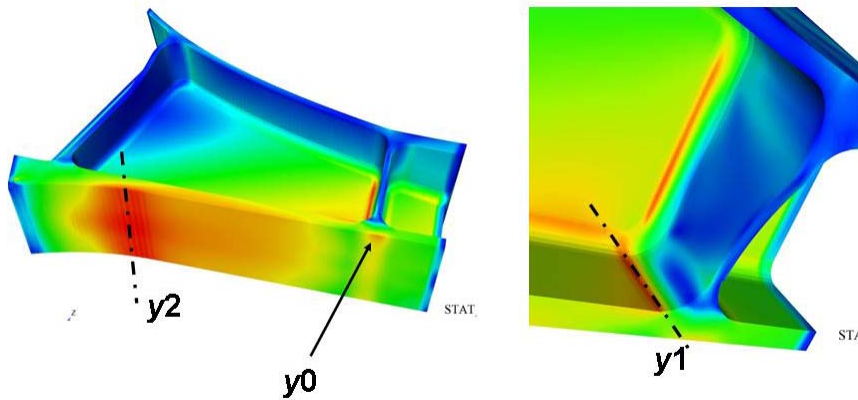


Figure 76: Critical areas with location y_0 and y_1 for DB2, and y_2 for DB3

In the fatigue crack growth prediction program, each load case has its own fatigue load spectrum channel so that fatigue load systems can be applied independent of each other. The fatigue load may be applied for each load case with different phases and frequencies. The analyses can be performed for a wide range of combination of frequencies for all the load channels. For each load case, the spectrum may be introduced in-phase or out-of-phase, or with certain phase shift.

The fatigue sequence in this multiple channel consists of a few hundred filtered fatigue cycles, including the load cases for 1g, 5g, and -3g sustained manoeuvre. With all these inputs, the MSD fatigue crack growth is analysed at first according to the linear approximation solution for the prediction of crack growth. The predicted results are shown in figure 77 for the crack growth on the surface (c dimension). The prediction of fatigue crack growth showed that, in this case, the growth of the first corner crack is very slow. The result of the first corner crack, Crack 1, is omitted in this figure.

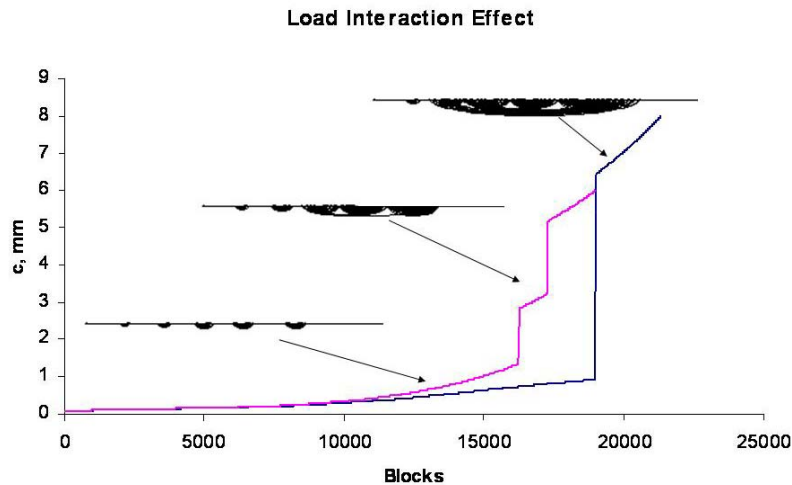


Figure 77: The prediction of MSD development under the example manoeuvre sequence. The first link-up of the crack is expected after load blocks 16000.

Data Base DB3: Another critical area is shown in figure 76 at the location along y_2 . In this area, the stress level at the manoeuvre load cases is very close to the stress level for DB2 (Tables 14-15). An MSD database is created for this area. This database is called DB3.

Again, the same distribution of the initial cracks ($x = 0, 3, 6, 9, 12, 16 \text{ mm}$) and sizes ($a_0 = c_0 = 95 \mu\text{m}$) as those used for DB2 are used for prediction of fatigue crack growth for DB3. The linear MSD prediction of fatigue crack growth is performed at first using the simple manoeuvre mission segment as shown in figure 75. The prediction result is shown for the case as indicated with a large corner crack in figure 78. The linear prediction based on MSD model shows that the corner crack becomes rather critical. In this prediction, a single, dominant crack will be initiated at the edge of the frame. This crack behaves as a typical corner crack with its slow growth at the beginning when the crack size is small before a rapid increase of crack growth rate occurs. The prediction in figure 78 shows that this behaviour is rather similar to the I-Beam test results [6] and represents the worst scenario for the fatigue crack initiation and propagation at this location.

As discussed in the validation phase for the I-Beam test results, there is a rather small probability that the worst initial flaw may be presented at the edge of the frame, a smaller crack size, obtained during the validation of I-Beam tests, is used in the new prediction of the MSD crack growth. For this case, the corner crack is assumed to be $a_0 = c_0 = 61 \mu\text{m}$, similar to that in the I-Beam validation, located at the flange edge. A new linear MSD prediction is made and the results are shown in figure 78 as the crack growth for Crack 1 to 6.

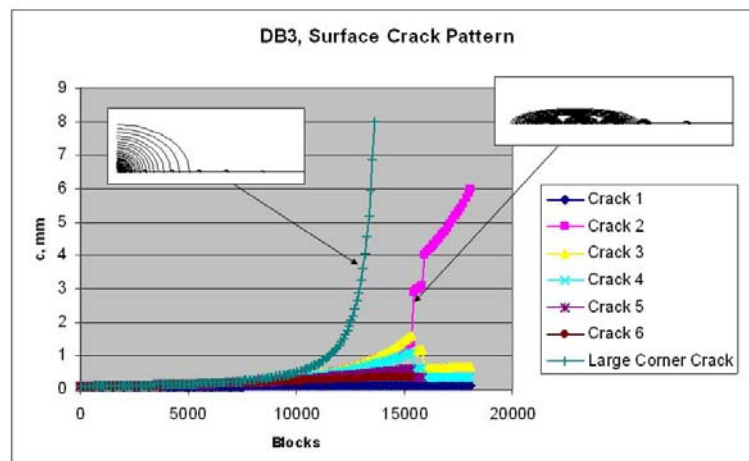


Figure 78: Comparison of linear MSD predictions of fatigue crack growth for DB3.

Data base DB4: The sub structure considered is shown in figure 79. A calculated high accuracy stress distribution is also shown. DB4 is used for the fatigue crack growth analyses of all the three manoeuvres.

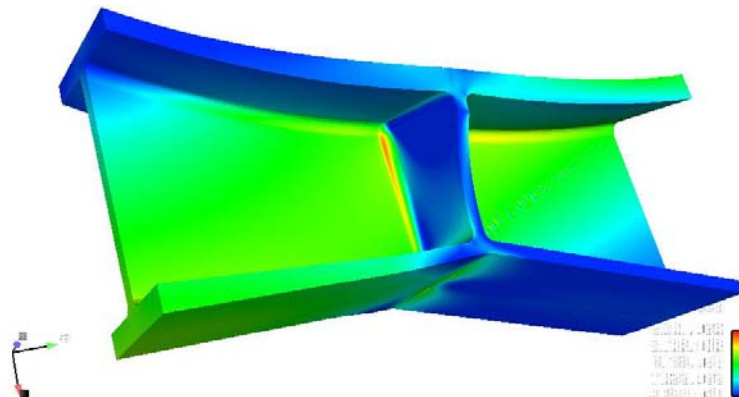


Figure 79: Finite element sub-model for MSD solutions and the critical location for DB4

Based on the finite element model, a stress intensity factor database is created as DB4. The input instruction and definition of fatigue cracks is shown in figure 80 and Table 15.

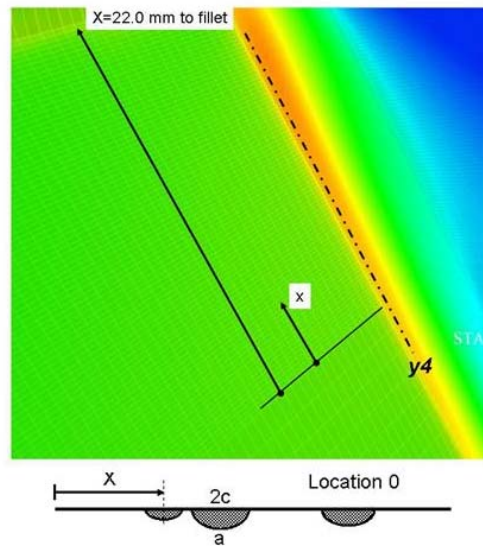


Figure 80: Critical location, cracks definition for DB4

Similarly to DB2 and DB3, the basic manoeuvre shown in figure 73 is considered for the purposes of demonstrating the solution and to identify severity of crack initiation and growth behaviour at this location compared to the other locations (DB2 and DB3). Then, the I-Beam load spectrum is considered.

The linear MSD crack growth prediction is shown in figure 81 for the surface crack size as a function of the load blocks. The predicted fatigue life for DB4 is substantially longer than those of DB2 and DB3, obviously due to the much lower stress level. The fatigue life in the term of the manoeuvre blocks as shown in figure 81 is more than 22 times of those for DB2 and DB3.

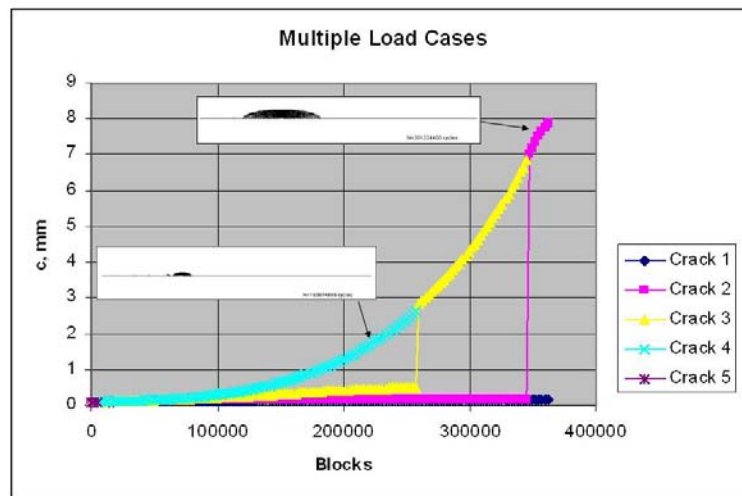


Figure 81: Predicted fatigue crack growth for DB4 the example spectrum

In summary, the methodology for prediction of MSD in critical details was briefly reviewed in sections 3.4.1–3.4.4 by analysing a few sample domains (Figure 50). The methods used were based on novel fracture mechanics principles with the accurate solutions for stress intensity factor and the non-linear elastic-plastic crack closure model for prediction of fatigue crack growth in MSD scenario with multiple load channels.

3.4.6 Fatigue Modeling of Materials at High Temperature

For Atlas (Aerodynamic and Thermal Load Interactions with Lightweight Advanced Materials for High Speed Flight) concept [10, 11], the vehicle is required to fly as common airliners with acceptable maintenance requirement. Rather high temperature is expected at all the leading edges, noses, and engine nozzles at the high speed up to Mach 6, see the left hand side of figure 82. One structural concept is to use a conventional sandwich solution as shown in the right hand side of figure 82. The structure will depend heavily on the stability of some new ceramic composite materials at high temperature as the heat shielding layer.

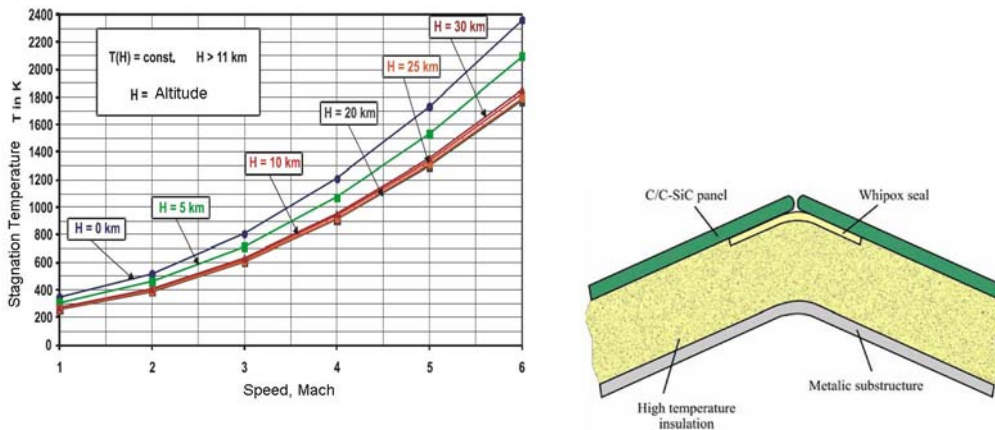


Figure 82: Stagnation temperature as a function of the air speed and ceramic sandwich structure.

An insulation layer is considered using hollow nickel based metal spheres with diameter around 3 mm sintered together, see figure 83. There is a high percentage of air trapped in the spheres as a good insulation media. It is expected that the insulation layer could act even as a good acoustic insulation layer to reduce the overall hypersonic booms during the commercial flight of the vehicle to reduce environmental disturbs when the vehicle is flying over populated areas. The insulation material is produced with HSP (Hollow sphere packing) technique developed at DLR using nickel metal based hollow balls.

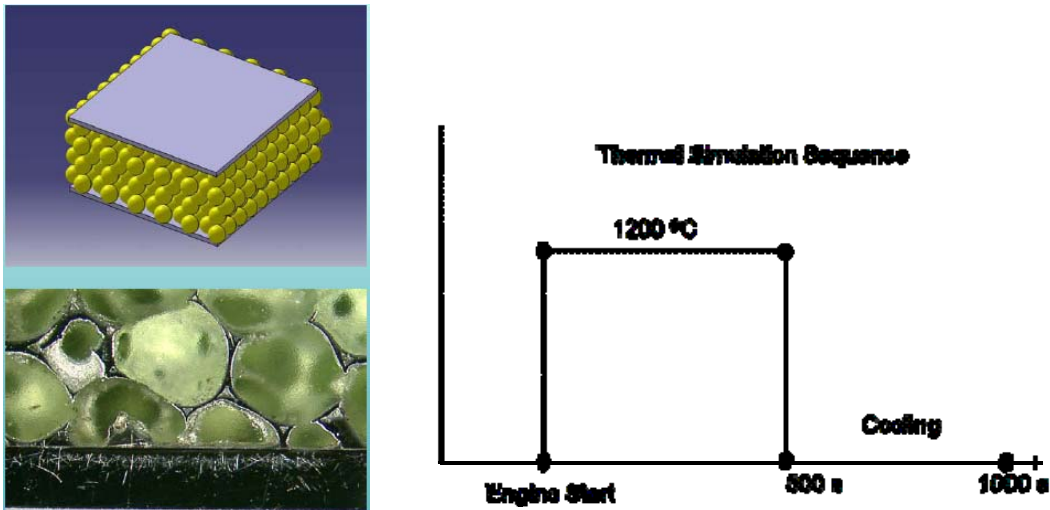


Figure 83: Hollow nickel based metal insulation layer and the engine shut down fatigue temperature profile.

Ideally, the construction should sustain a temperature as high as 1200 Celsius during the acceleration and cruising phase of the vehicle for a certain number of flights without major over hauls. The strength and fatigue capability of such a structure will be a major concern. Unlike most of the single use rocket vehicles, the transport vehicles should have economical fatigue life.

To evaluate the fatigue process, the high temperature property of material should be considered together with the usage as well as the structural solutions. In this concept stage, it is very important to understand possibility and develop methodology to deal with such a problem. A case study is provided here, together with some possible solutions.

Suppose the panel is located at the most unfavorable location, above the outlet of the main engine. Assume that the surface of the panel is experiencing a severe thermal cycle as the schematic in figure 83 shown. For this thermal cycle, the structure is assumed to be subjected to a thermal shock, starting suddenly at time zero to a temperature as high as 1200 Celsius to simulate an engine start. After a period of time, the engine is shutdown and a flow of cool air will blow on the surface to give the surface a cooling shock. The choice of 500s here is arbitrary, based on some previous computation which showed that distribution of temperature begins to stabilize for the structure solution after this period of time. The study here is to understand how severe the sandwich panel may be subjected at this extreme thermal cycle.

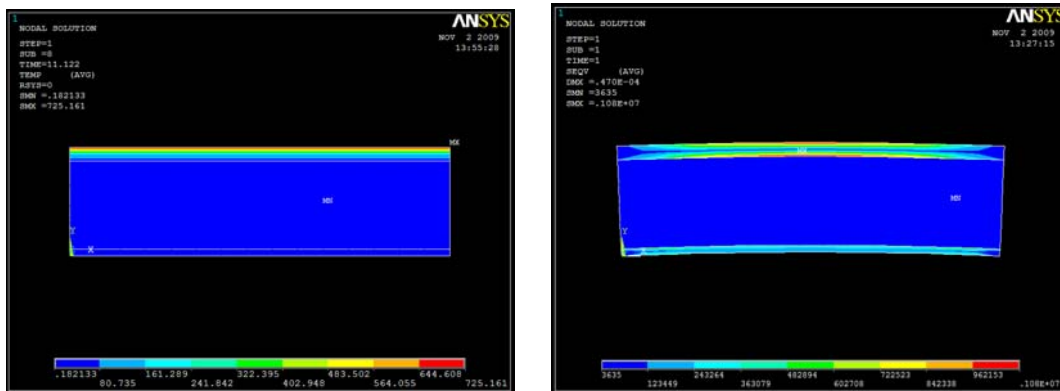


Figure 84: Example of temperature distribution, thermal stress and deformation due to the thermal shock.

All the pre-assumptions for the sandwich panel are made to develop methodology to deal with the thermal shock problems and to reveal problems involving in the structure solutions. Here the method is much more relevant than the results under the specific assumptions.

Arbitrarily, the heat shield is assumed to be made of WHIPOX (ref.1) with a thickness of 10 mm. Beneath the heat shield, there is a 50 mm thick insulation layer. The backing and load carrying panel is assumed to be a type of titanium alloy. A schematic of the construction is shown in figure 83.

Different analyses are compared to identify thermal problems in the construction. Stabilised thermal analyses have been performed as well as transient thermal analyses to reveal critical issues for the construction.

The analyses indicate severe thermal shock for such construction. For example under the assumed thermal cycle, the analyses show that the most severe stress occur about 11 s after start of the engine. According to the transient thermal analysis, the temperature distribution at this moment is shown in the following figure.

While most part of the sandwich panel is still in the room temperature after 11s, and the surface temperature is still far from the gas temperature of the engine. In this case with a maximum surface temperature of 725 Celsius, compared to the gas temperature of 1200 Celsius, maximum stress is created on the surface of the heat shield WHIPOX panel.

Von Mises thermal stress distribution for the composite panel at this moment indicates high stress on the surface of the thermal layer and the interface between the thermal layer and the insulation layer. The right hand side of figure 84 shows the stress and deformation results at this moment. The thermal expansion of surface layer will force the panel to buckle outward, indicating the need for further structural optimization so that the fluid/structure interaction between the panel and hot airflow may be under control. The stress results indicate that there are two critical areas that should be considered very carefully, the one area is the surface area that is in direct contact with the hot gas. Another, less obvious, area is the interface between the surface heat shield WHIPOX panel and the insulation layer. At this location, there is also rather high stress which may lead to separation of the bound between the surface panel and the insulation layer, resulting in delamination damage.

The high stress here is due to both the heat conducting and thermal expansion differences between the two materials. Obviously, in addition to a good thermal stability of heat layer and insulation layer, a good interface bounding is required so that structural integrity is not compromised.

For a general picture of the thermal shock process, the right hand side of figure 85 shows the distribution of temperature through the thickness during the heat-up period. In this figure the horizontal axe represent the distance from the backing layer.

As may be expected, the gradient of temperature becomes less severe with the time increases. The insulation layer is heated up gradually. A stabilized state may be achieved when the heating is sustained more than 500 seconds. Transient analyses give the following temperature distribution in the thickness of the structure.

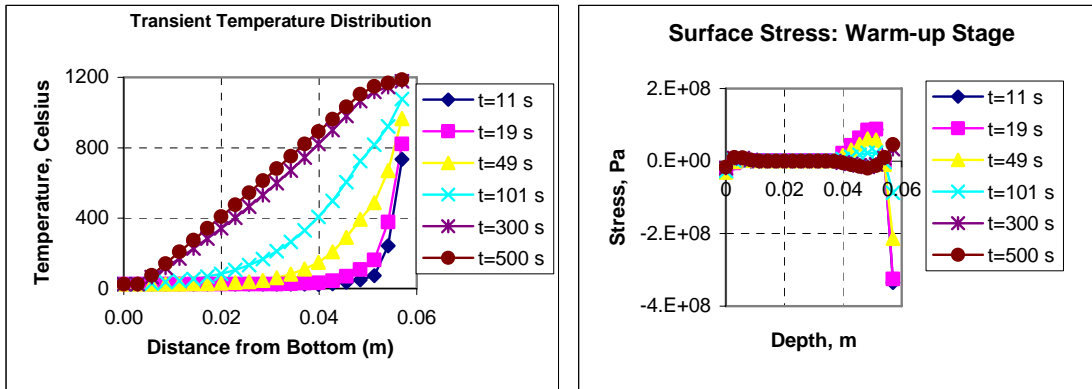


Figure 85: Temperature distribution and maximum principle stress during the thermal cycle

For the material strength point of view, it is much more relevant to consider the thermal stress during the heating process. Since during the warm-up process, stress distribution will be changing dramatically as a function of time. Similar to the temperature distribution, the stress is analysed as a function of time at the centre location of the sandwich panel.

The stress results indicate that the maximum stress is located on the surface directly in contact with the thermal flow, changing from the initial compressive state to a slight tensile state when the temperature is stabilized. In the initial heating, the thermal expand of the surface is obviously constrained by the insulation and backing layers. A compressive stress on the surface is understandable. When the temperature reaches the stabilised state, the stress on the surface will now depend on the temperature distribution in the structure and the thermal expansion of the surface layer, the insulation layer, and the backing layer. For the case study, the stress on the surface becomes tensile after the initial strong compressive stress.

To consider change of temperature on the gas/structure interface, the analyses give a solution for the surface temperature as shown in figure 86. The result shows that the temperature rises slowly until the flow temperature is approached. The most interesting point here is that the highest surface stress is not created at the highest surface temperature. The surface experiences the peak stress at the temperature between 700 and 800 Celsius at a value of more than -380 MPa. When the highest temperature is approach, the value of stress is dropped to tenth of the peak value, about 34 MPa with a different sign (tensile type).

It is critical to understand the stress changes during the heat cycle. The transient thermal analysis is performed for the whole thermal cycle and the resulting surface temperature is shown in the following figure. This is the temperature distribution on the gas/structure surface for both the heat up and cooling down period, indicating that there is another dramatic change of temperature immediately after the shut-down of engine.

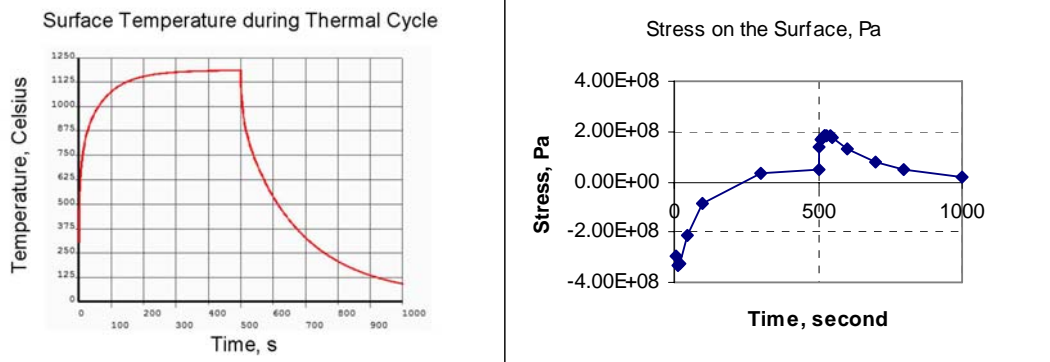


Figure 86: Temperature and stress on the heat surface as a function of time

On the most stress critical surface area, the change of stress is computed as a function of time. The resulting maximum stress is shown in figure 85. In this figure, it is shown that initially, high compressive stress is created during the heat up period, with a maximum value occurring at about 11 second after start of the engine. The stress is then reduced when the heat begins to spread inside the insulation layer and a stabilized state is approached when the heating time becomes longer than 500 seconds. At the stabilized condition, a surface stress at a value of about 30 MPa is created, compared to the extreme value of -380 MPa. The computation demonstrates that the stabilized thermal analyses, which are much simpler, will provide false information about stress state at this thermal shock condition.

Immediately after the shut-down of the engine, suppose the vehicle is still flying, cold air will flow over the heated surface to cool down the surface. This creates another shock for the material. The rapid cooling and shrinkage of surface layer will be prevented by the heated material below the surface. A tensile stress will be created. For the case study, the stress reaches then to about 200 MPa for the stabilized state of about 30 MPa.

During the heat cycle which may represent a ground-air-ground cycle for the transporter. Without any other mechanical stresses, the thermal stress will change dramatically from a compressive extreme of -380 MPa to a tensile extreme of nearly 200 MPa. The temperature and stress behaves differently since the highest temperature does not occur at the highest temperature. The fatigue damage during a thermal cycle should be considered for both stress and temperature, and the existing methodology to evaluate fatigue damage should be further extended to include the integrated effect of temperature, stress, creep and oxidation.

It is obvious from the thermal/stress couple analyses that:

- 1) Cooling on both the surface side and back side is needed for the sandwich structures even with the thermal insulation layer
- 2) Fatigue critical areas are located on the surface (CMC) with direct contact to the hot jet, and the interface between the surface layer and the insulation layer. Two failure modes should be considered: one for the surface cracking, and the other for the interface delamination.
- 3) Highest stress does not occur at the highest temperature. The fatigue damage evaluation should include multiple parameter damage model including effect of temperature as well as stress on the material property.
- 4) Interface between the surface panel and the insulation core may be a potential problem area when the interface bonding is not properly created.

3.4.7 Fatigue crack growth behaviour of Inconel 718 with high temperature hold times

Fatigue crack growth measurements have been made on center cracked tension specimens of Inconel 718, where the focus has been to observe the effect of high temperature hold times on the fatigue crack growth behaviour of the material, [12]. The material testing has been done at three different temperatures, 450°C, 550°C and 650°C. All testing were done in an isothermal fatigue crack growth context with a standard test method for measuring the crack growth rates.

Baseline test series were carried out with a load frequency of 0.5 Hz at the three different temperatures, 450°C, 550°C and 650°C. Two tests were done at each temperature. Furthermore hold time tests were carried out using a trapezoidal waveform with 1 s ramp up, hold at maximum load and 1 s ramp down. The hold time tests were done at the temperatures 550°C and 650°C for the hold time lengths of 90 s and 2160 s. One test was done for each case, except for the 550°C and 90 s hold time test, where two tests were done. All tests were done in laboratory air and at load ratio of $R=0.05$.

The baseline crack growth data (da/dN vs ΔK) are found in figure 87. As can be seen the growth rate increases with increasing temperature. The room temperature precrack of a test specimen were examined in a microscope. As can be seen, the fracture mode for the precrack was primarily trans-granular.

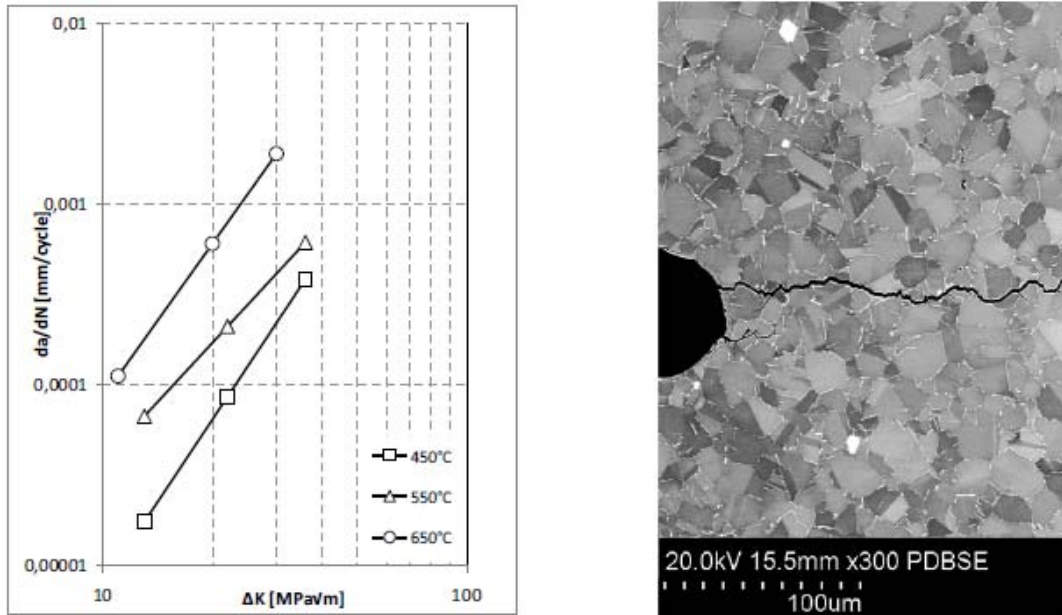


Figure 87. Baseline test results and microscope photo of the room temperature precrack

Furthermore one test specimen of each temperature of the baseline test was examined, and showed also a primarily trans-granular fracture mode. The crack appearance for the 650°C case is shown in figure 88.

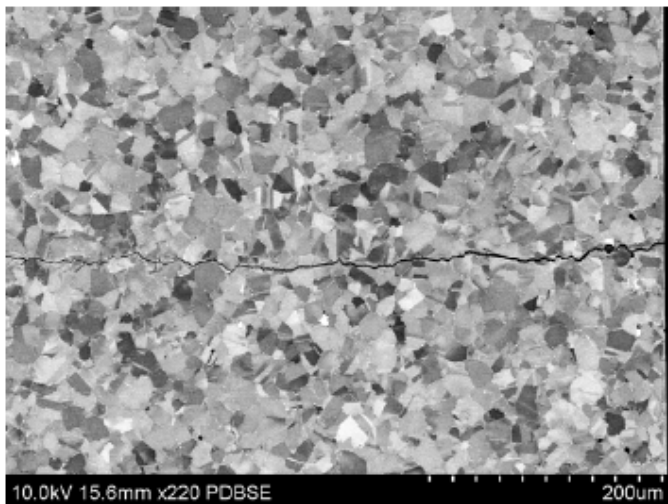


Figure 88. Baseline test crack at 650°C.

When a hold time of 90 s is applied, the crack growth rate increased dramatically, as can be seen in figure 89. Specimens tested at 550°C and 650°C, respectively, were also examined in microscope. A change of fracture

mode could be seen for both temperatures, when the 90 s hold time was applied. The crack of the 650°C 90 s hold time test specimen can be seen figure 89 also. As can be seen, the fracture mode is mainly intergranular.

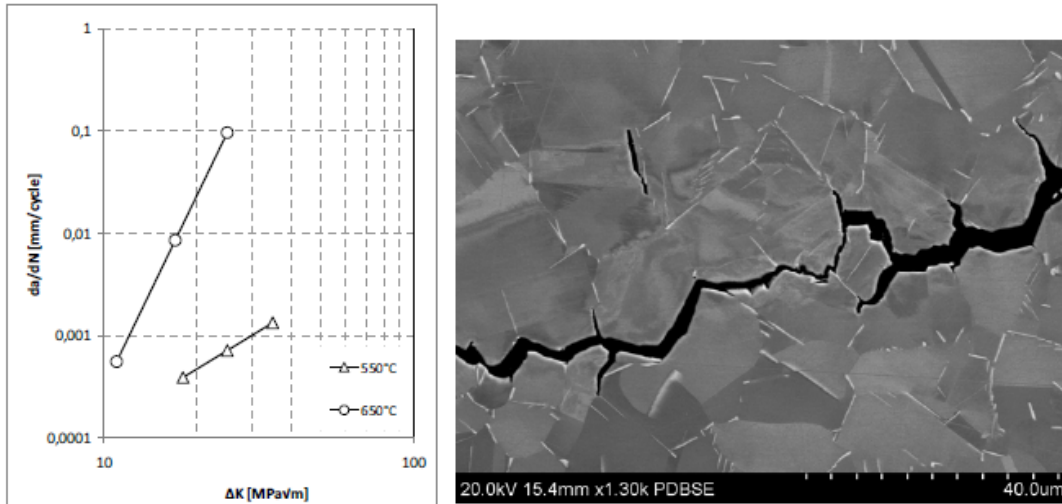


Figure 89. Crack growth rates for 90 s hold time tests and 650°C crack at 90 s hold time

When a hold time of 2160 s is applied, the crack growth rate is further increased, as can be seen in figure 90. Once again two test specimens, tested at 550°C and 650°C, respectively, were examined in microscope. The crack of the 650°C 2160 s hold time test specimen can be seen in figure 90 as well. The fracture mode is mainly intergranular.

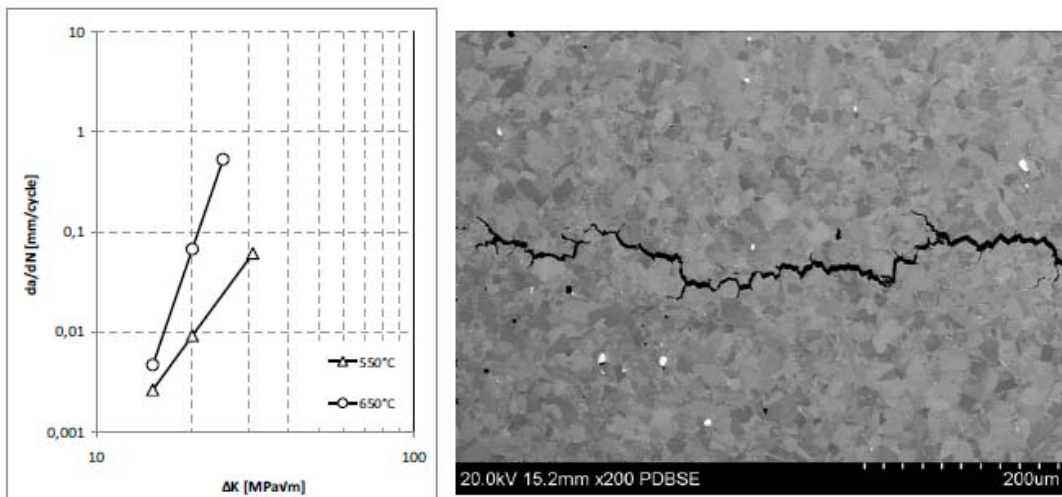


Figure 90. Crack growth rates for 2160 s hold time tests and 650°C crack at 2160 s hold time.

The experiments show two different regimes of active fracture mode. In the baseline testing it was shown that for all temperatures the active fracture mode was transgranular cracking with a lot of plastic deformation (slip bands) around the crack path, indicating that the dominating fracture mechanism in the baseline tests is cyclic plastic deformation around the crack tip.

The other fracture mode present in the testing can be seen when a hold time is applied. At both 90 s and 2160 s hold times and at both 550°C and 650°C the fracture mode is mainly intergranular with very few slip bands can be observed around the crack path for the hold time tests. This indicates that another fracture mechanism is dominant during these tests. The crack growth rate (da/dN) is also vastly increased when a hold time is applied. For 550°C the increase of crack growth rate from zero to 90 s hold time is, at a certain ΔK level approximately 3 times, and for 2160 s it is approximately 50 times. For 650°C there is a much greater increase; from zero to 90 s hold time we find approximately 50, and for 2160 s we get more than a 100 times higher crack growth rate. For comparison, the increase in crack growth rate from zero hold time at 450°C to 2160 s hold time at 650°C, an

increase of approximately 1000 times is found, figure 91, where the trendlines for all test cases are presented. The increase in crack growth rate along with the active fracture mode indicates that a time dependent fracture mechanism is active. In the literature, there seems to be a consensus, that this intergranular crack growth is due to oxygen.

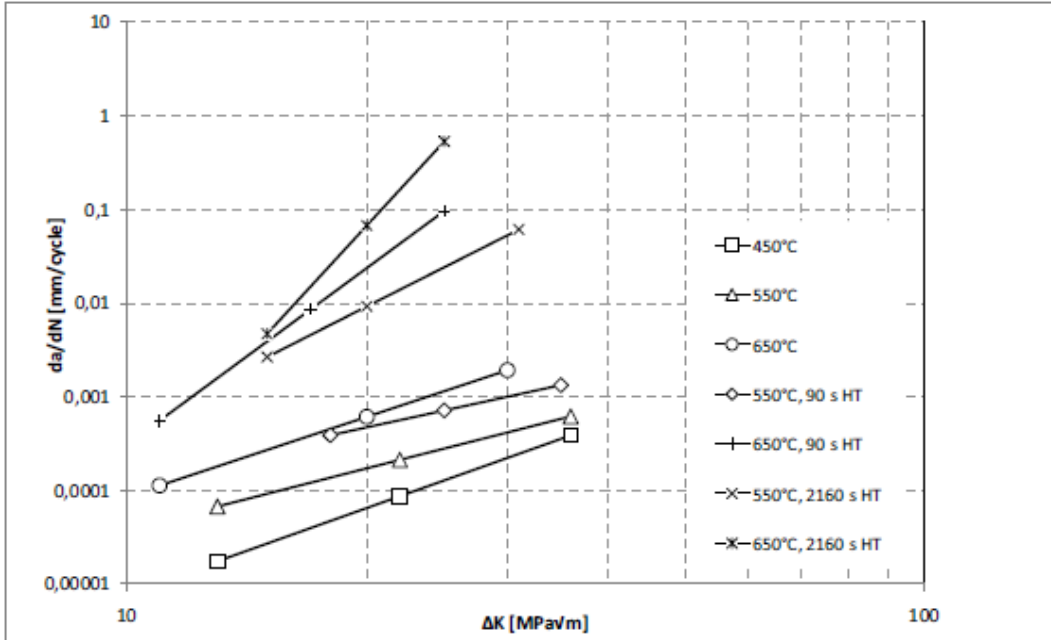


Figure 91. Crack growth rates for all tests.

3.5 COMPOSITE MATERIALS

3.5.1 Mechanical Testing of Battle-damaged Wing Boxes

Two large wing boxes, 3300x630x200 mm³, with nine cells have been tested. Wing box 1 with composite substructure and wing box 2 with aluminium substructure. The wing skin was in both cases made of composite. The wing boxes were mechanically loaded in four-point bending to 0.13 % strain and water filled when being shoot at, shoot 1, with a spherical 12.5 mm bullet. The bullets exit side was the compressive side of the wing box. There were some delaminations in the wing skin after shoot 1 but no major damage. For wing box 1 there was extensive damage to the composite substructure. For wing box 2 it was not possible to measure if plastic deformation had occurred of the substructure. Both wing boxes were loaded to limit load without failure after being shoot at.

The wing boxes were rotated such that shoot 2 exited on shoot 1's entrance side. Shoot 2 was done as shoot 1 but at another place and with a 12.7 mm API, armour piercing incendiary, ammunition. For both wing boxes there were extensive damage to the wing skin and it broke at fasteners connecting the wing skin with the substructure, see Fig. 92. The damage to the composite substructure was extensive for wing box 1 and skin had lost connection to the substructure next to where shoot 2 hit. For wing box 2 aluminium substructure flanges had bent upward permanently. During quasi-static loading wing box 1 broke at -0.14% strain and wing box 2 broke at -0.18% strain. In both cases the failure mode was buckling which caused the substructure to break, see figures 93 and 94.

The wing boxes were shoot a third time, shoot 3, with 12.7 mm API ammunition without any mechanical loading. This resulted in substantially less damage to the wing skin than for shoot 2, see figure 95. High speed filming and strain gauge measurements showed that the buckle from the bullet was much smaller when the skin was not loaded in compression. It can be argued that compressive loading causes the skin to buckle when shoots at and that this causes more damage to the skin.

Detailed dynamic strain measurements were done on the exit side of the wing box with strain gauges at different distances from the exit hole of the bullet. Measurements from shoot 1 on wing box 2 is shown in figure 96, where the strains are measured in the direction away from the bullet exit hole. The bullet enters the wing box at $t=0$ and the strain gauge at $r=0$ is where the bullet exits the wing box. The strain curves can be schematic explained with a buckle that propagates from the bullet hole and outwards. The strain gauge at $r=123$ mm is placed between fasteners connecting the wing skin with the substructure. The fasteners reduce the bending stiffness of the skin and this is the place where the skin would break first.



Figure 92. Damage on exit side of wing box 1 after shoot 2 with delaminations shown and damage to substructure.

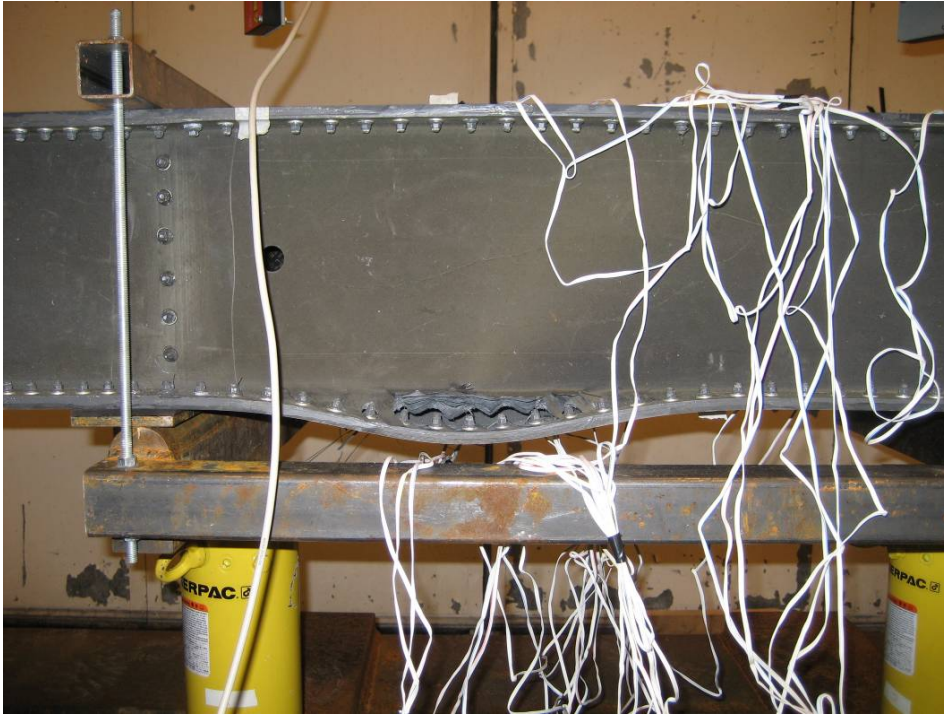


Figure 93. *Quasi-static failure of substructure of wing box 1 due to buckling of wing skin.*

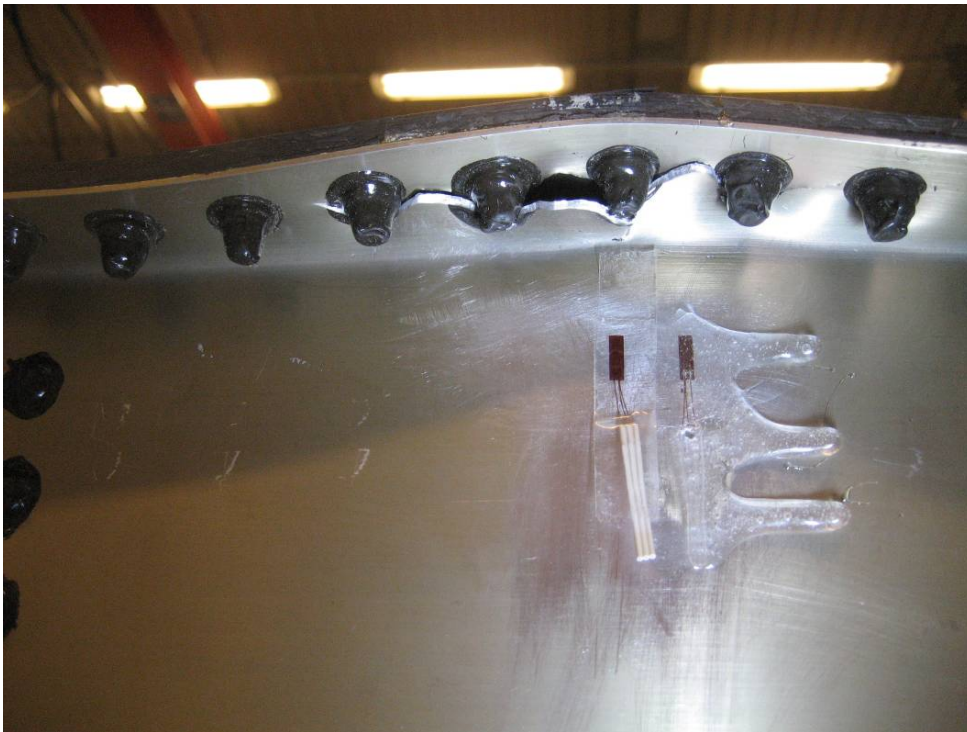


Figure 94. *Quasi-static failure of substructure of wing box 2 due to buckling of wing skin.*

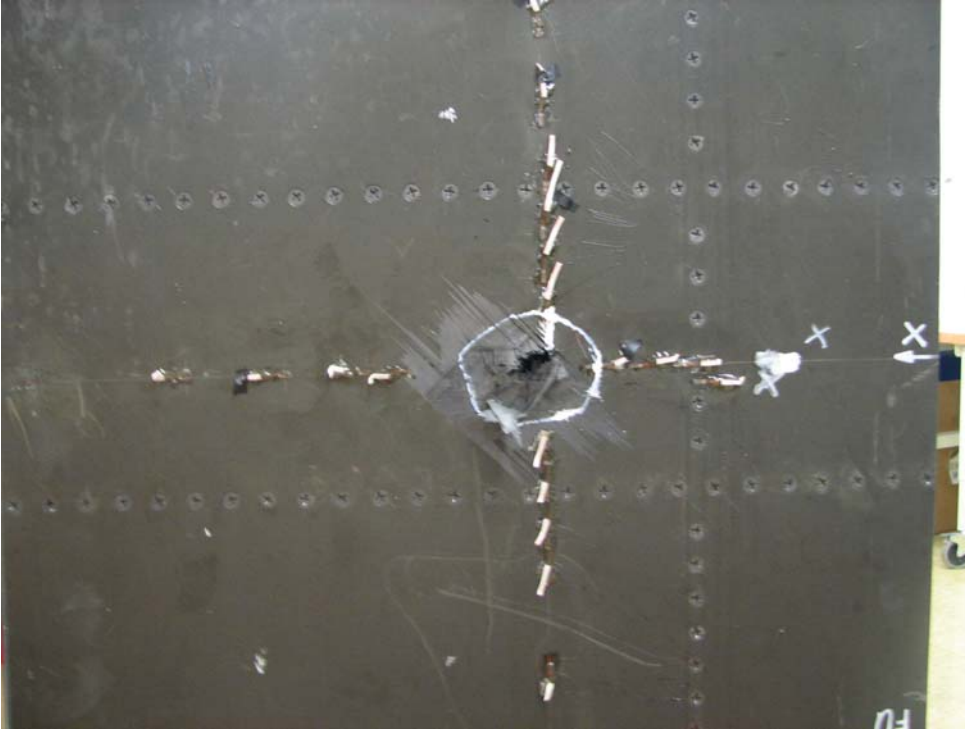


Figure 95. Damage at exit hole of unloaded wing box 2.

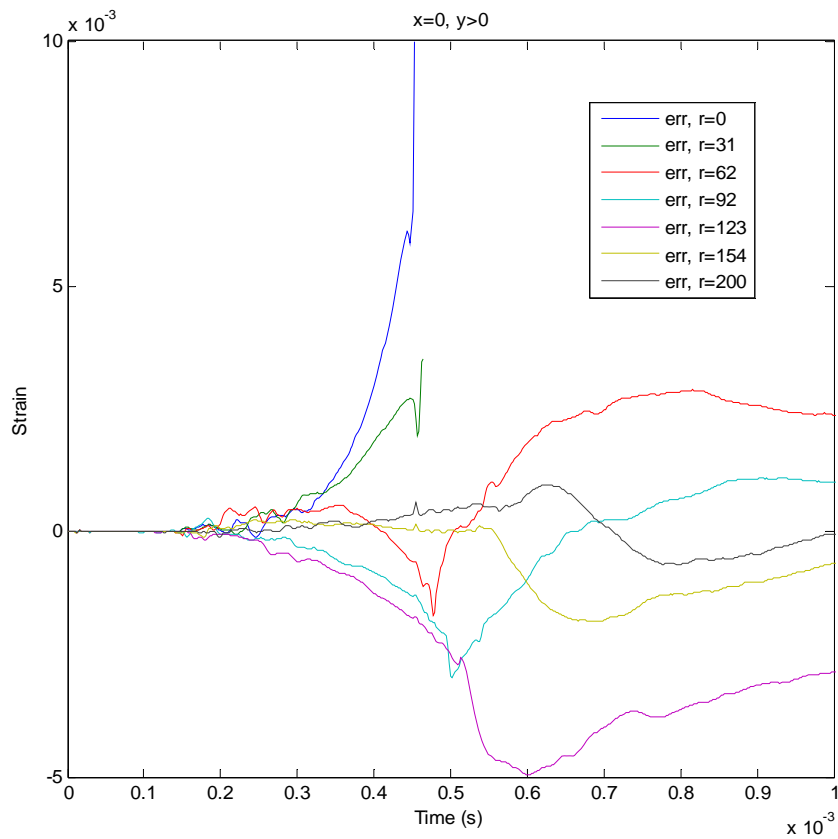


Figure 96. Dynamic strains on exit side of wing box 2 for shoot 1.

3.5.2 Shear Test of Impact Damaged Composite

Composite plates 300x450 mm² in size and approximately 4 mm thick have been impacted and then shear loaded to failure. Three impact energies have been used, 25 J, 35 J, and 50 J. During impact two sides were clamped and two sides were simply supported with a free length of 230 mm and 150 mm, respectively. The plates were c-scanned after impact, see figure 97 for an image of a specimen impacted at 35 J. The vertical damage is due to “splitting” of the surface ply. Specimens were tested in a shear loading frame and applied force was recorded and a digital speckle photography system was used. A specimen without impact damage and with strain gauges was used to relate applied load with shear strain. Preliminary analysis suggests the principal compressive strain at failure of shear loaded specimen is about the same as failure strain for traditional compression after impact test. After failure a tensile crack and a compressive crack is shown approximately perpendicular to each other as would be expected for shear loading, see figure 98.

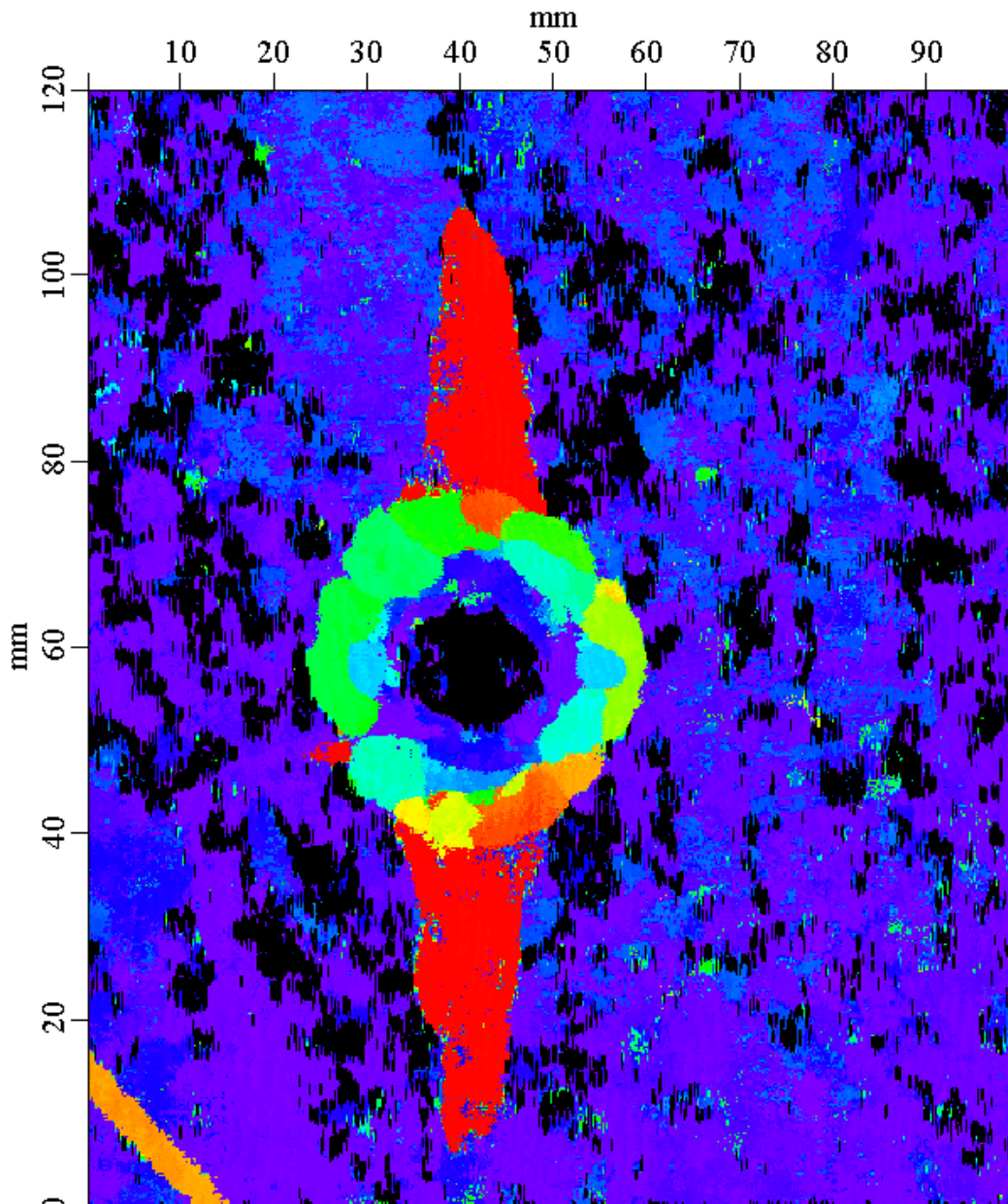


Figure 97. C-scan of specimen impacted at 35 J.

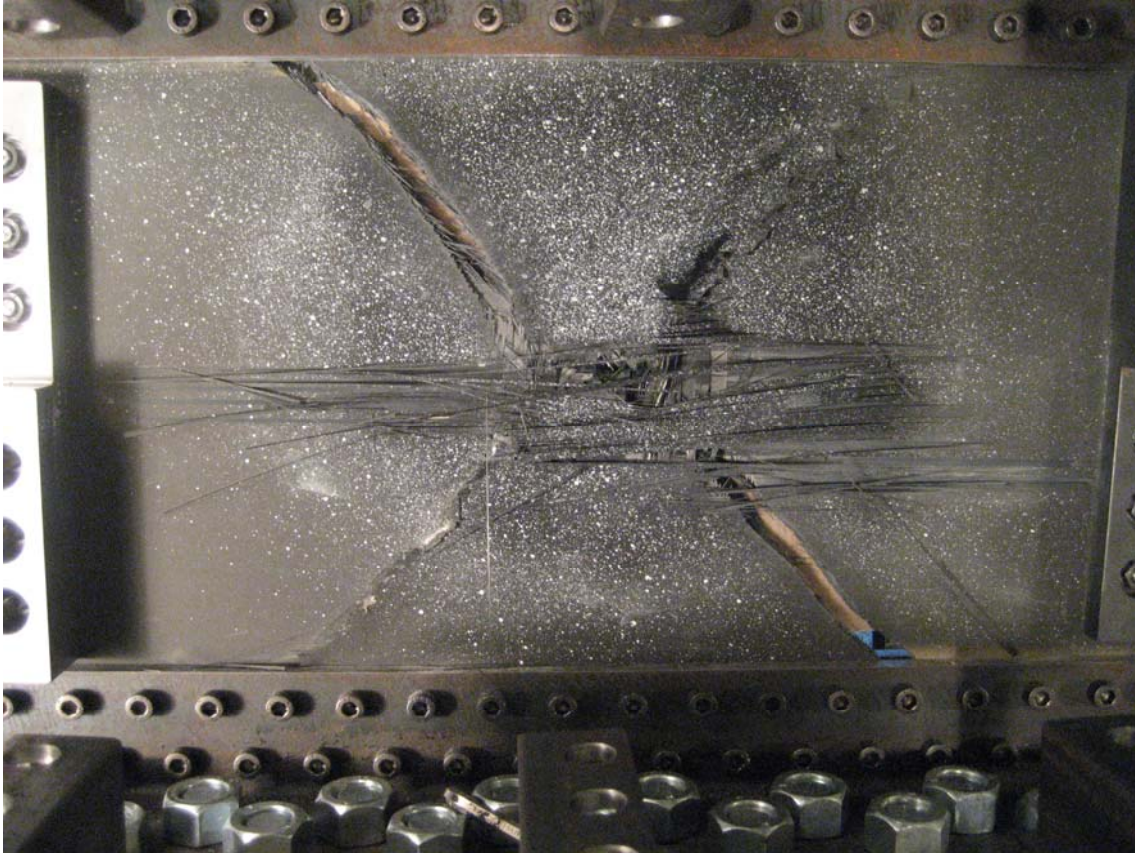


Figure 98. Shear loaded composite plate after failure.

3.5.3 More effective composite structures through improved sizing methodology

In order to more effectively employ composite materials in aircraft structures and to reduce manufacturing costs, more and more integrated structures are designed. There is also a trend towards thicker composite structures. As a consequence more areas with high interlaminar stresses, which traditional design methods can't handle, are designed. Above these problem areas there is a need to increase strain allowables to reduce the weight of composite structures. Presently, restrictions and conservatism in the design tools introduce more weight. The research work within this project has a focus on effective design with respect to interlaminar stresses in order to reduce the conservatism in the sizing of composite structures.

It is a joint project between Swerea SICOMP AB, the University of Skövde, Saab Aerostructures, funded by the VINNOVA – the Swedish Governmental Agency for Innovation Systems.

Swerea SICOMP AB develops techniques to design integrated T/L-joints used for joining wing-panels to the substructure. During the course of the work different FE-methodologies to analyze such joints are studied and both stress based and fracture mechanical based failure criteria are adopted. In an accompanying project also funded by VINNOVA methodology to predict residual stresses from manufacturing due to chemical shrink and temperature in such joint are being developed. Techniques to effectively and more accurately determine fracture mechanical properties are being developed at the University of Skövde and the developed cohesive laws are adopted in the FE-analyses in the project.

Specimens to be tested are produced by Saab Aerostructures, see figure 99, and will be tested by Swerea SICOMP AB. After tests, the specimens will be subjected to fractographic analyses in order to compare also the predicted failure mode with experimental results.

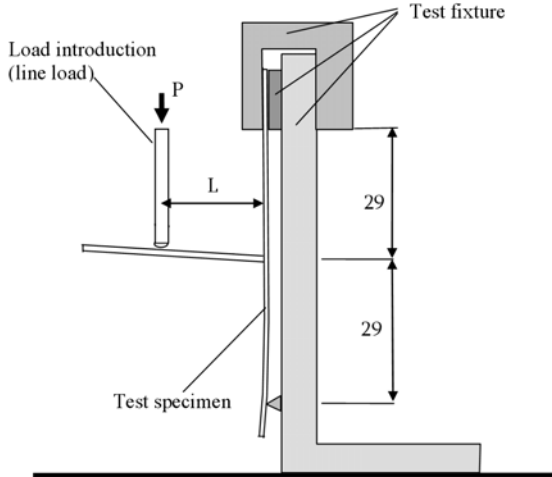


Figure 99. Test arrangement for T-joints

During FE-analyses cohesive laws developed in the project are adopted to predict failure initiation and growth. Cohesive elements are defined by a linear elastic response, a strength criteria and a damage evolution law based on energies. Damage initiates when a quadratic stress criterion is fulfilled ($\delta = \Delta^0$), see equation (1). The strength of the composite in the normal and shear directions are used as input data. The damage evolution is governed by a damage parameter which describes the rate of stiffness softening after damage initiation ($\delta = \Delta^0$). The damage propagation ($\delta = \Delta^f$) is studied in terms of energy release rate and fracture toughness. To accurately predict delamination growth for mode I and mode II loading condition [13], the Benzeggagh-Kenane criteria are used [14], as expressed in equation (2).

$$\left(\frac{\sigma_{33}}{\hat{\sigma}_{33}}\right)^2 + \left(\frac{\tau_{13}}{\hat{\tau}_{13}}\right)^2 + \left(\frac{\tau_{23}}{\hat{\tau}_{23}}\right)^2 = 1 \quad (1)$$

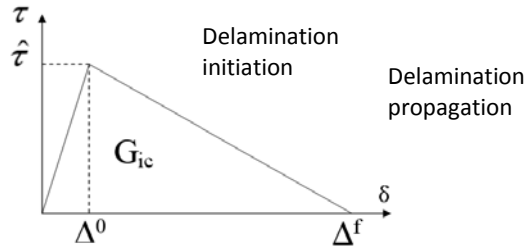


Figure 100. Principle for the bilinear traction separation law applied in the analyses.

$$G_{Ic} + (G_{IIc} - G_{Ic}) \left(\frac{\beta^2}{1 + 2\beta^2 - 2\beta} \right)^\eta = G_{mc} \quad , \quad \text{with } \beta = \frac{\Delta_{shear}}{\Delta_{peel} + \Delta_{shear}} \quad (2)$$

3.5.4 Residual stresses and 3D failure criteria for NCF-materials

The project ReFACT aims to develop methods to predict failure due to triaxial stresses and residual stresses in components manufactured by resin impregnation of dry fibre mats (so called NCF). ReFACT is a four year project (2009-2013) within the 5th National Aeronautical Research Program (NFFP5), which is funded by the Swedish Governmental Agency for Innovation Systems (VINNOVA). Project partners are Swerea SICOMP, the project leader Volvo Aero Corporation, and the associated partner Luleå University of Technology.

Details in aeroengines have a complex geometry and are manufactured in relatively large series. Resin impregnation of dry fibre mats allows for cost efficient manufacturing of complex geometries and is therefore

the main alternative for future engine details of composite materials. The manufacture causes, however, residual stresses and the complex geometries and loads cause multiaxial stress states. Methods must therefore be developed to calculate these stresses and when they cause failure. A specific problem that needs consideration is the inhomogeneous material structure with resin impregnated fibre bundles surrounded by pure resin pockets, figure 100.

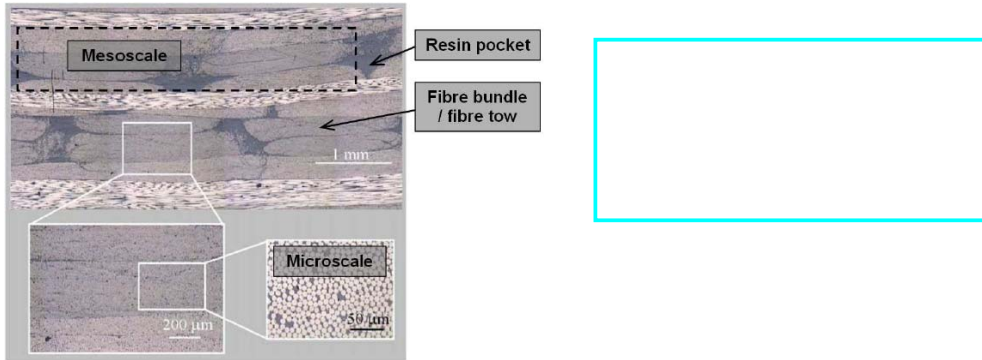


Figure 100: Tri-axial stress state caused by complex structural geometry and NCF meso-structure.

Within the project Swerea SICOMP is developing test methods and failure criteria for multiaxial loading of composites with an inhomogeneous microstructure, as well as methods to predict residual stresses in such materials. The failure criteria are based on combination of failure criteria for fibre bundles as well as pure resin zones under triaxial stress, and mesomechanical models which predict the stress state in bundles and pure resin under applied global stresses. The failure criteria will be validated by application to a loaded component. The general modelling approach is illustrated by figure 101.

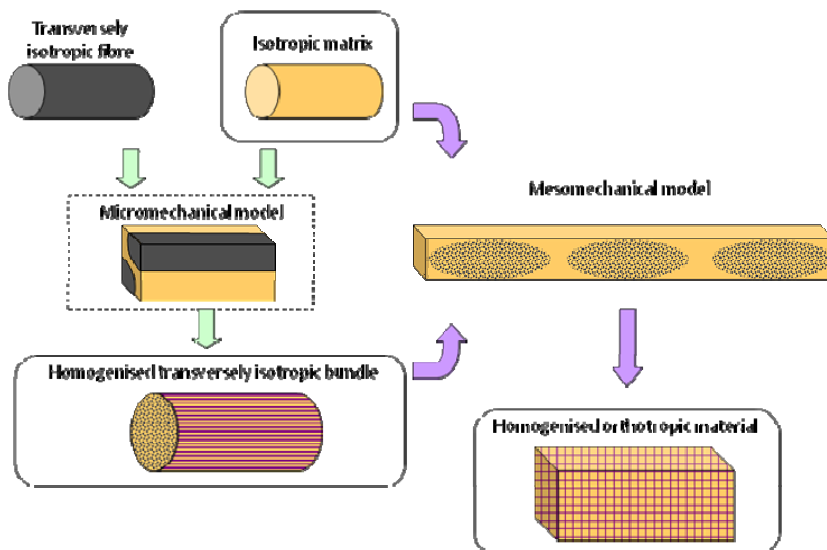


Figure 101: Hierarchic modelling approach for NCF composite material.

Initial work has included literature surveys of failure criteria of orthotropic and transversely isotropic materials under triaxial stress [15] and a survey of test methods for composite materials under multiaxial loading [16]. Ongoing work includes studies of the influence of geometrical and material parameters on the stress state in mesomechanical models, and studies of the strength of NCF bundle material under various uniaxial and multiaxial stress states.

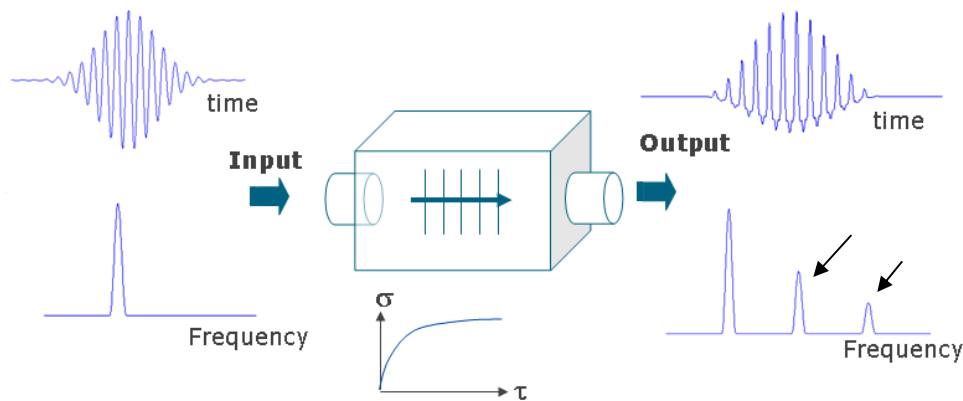
3.6 NDT TECHNOLOGY

3.6.1 Evaluation of Nonlinear Ultrasonics for early detection of fatigue damage and structural degradation in aerospace structure.

During the last decade, the use of nonlinear ultrasonic for detection and characterization of early fatigue damage has been reported and discussed in the NDT community [17]. The Nondestructive testing laboratory at Exova AB, Linköping, has under the last years been involved in the development and evaluation of some of the procedures based on nonlinear ultrasonic for early detection of fatigue damage. The objective of the work was to identify and evaluate measurement schemes that present the best potential for inspection of CFRP composite laminate and bonded structures.

The origin of ultrasonic nonlinearities due to small-scale microcracking has been reported and discussed for several types of materials (metals [18], plastic and polymer [19], composite [20], etc...). Early fatigue damage leads to microscopic degradations that produce local nonlinearity levels that are significantly higher than the intrinsic material nonlinearity. The excess ultrasonic nonlinearity linked to fatigue damage has been shown to occur much before the effect of degradation can be detected with classical NDT techniques and can potentially be used to detect and localize the initiation of fatigue.

“Linear” ultrasonic techniques are mainly based on the measurement of amplitude variations of an ultrasonic pulse generated and propagating in the structure under investigation. Nonlinear techniques rely on the measurement of signal characteristics that only can be explained by nonlinear propagation such as for example the appearance of harmonics in the ultrasonic signal as shown in figure 102. In a first step, an evaluation of the technique sensitivity was performed using an immersion scanning system modified in order to generate imaging of the harmonic amplitude (or of the ratio of the harmonic amplitude over the fundamental). In a second step, evaluation of procedure based on a manual, hand-held device were made.



Nonlinear relationship between strain and stress

Figure 102: The effect of nonlinearity on the propagation of a narrowband pulse. The appearance of harmonics in the frequency spectrum are used to determine the nonlinearity of the material

Nonlinearity in CFRP laminate

An evaluation of the performance of Harmonic Imaging was performed for CFRP samples. The samples used for the study are 32 plies AS4/8552 laminate with a $[(0,90,-45,+45)_4]_{s32}$ lay-up. The size of the sample was 130mm*13mm*4mm. Fatigue cycling was performed using a four-point bending system. A picture of the experimental set-up for fatigue cycling of composite is shown in figure 103. This type of loading introduces shear and bending stresses in the laminate. Shear stress is expected to induce microdelaminations between plies and bending stress induces mainly matrix cracks running through the outer plies. A critical aspect of the fatigue procedure was to stop the cycling before delamination onset in the sample for evaluation of the harmonic imaging technique. In order to monitor the fatigue damage acoustic emission monitoring was used.

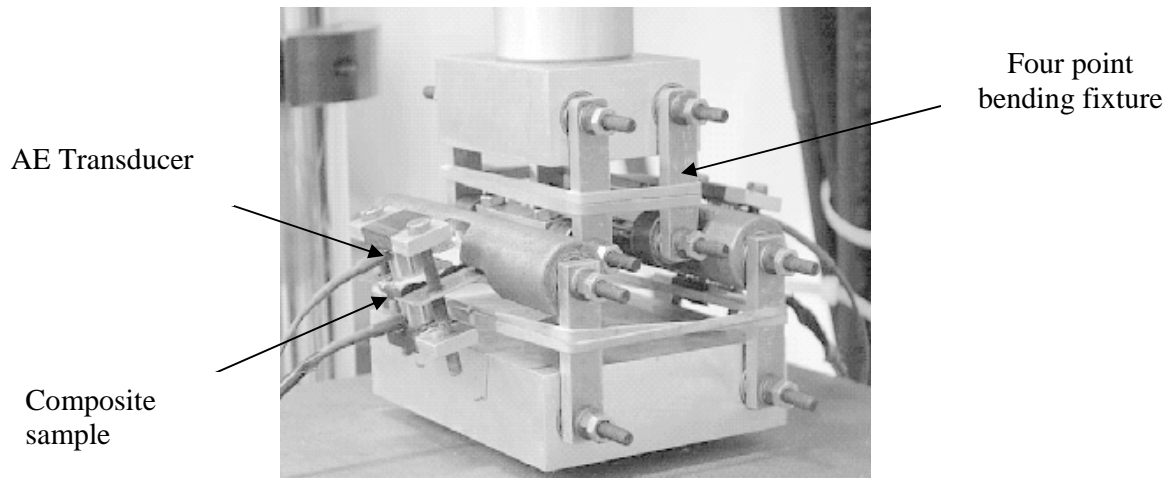


Figure 103: 4 point bending holder and AE emission sensors used cycling and monitoring of the fatigue damage

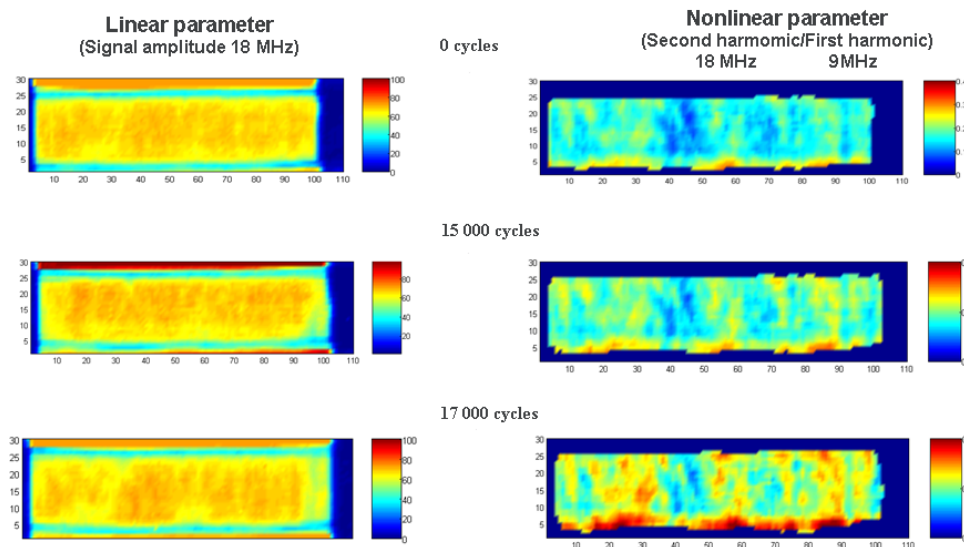


Figure 104: Conventional amplitude C-scans (on the left) and harmonic amplitude scans for a CFRP sample at different cycles of 4 point bending test

Conventional amplitude C-scans and harmonic imaging were performed on the pristine samples and at different stage of the fatigue cycling allowing a comparison of the sensitivity of the methods. At each stage the samples were unmounted from the fatigue holder and scanned in an immersion tank. The same experimental conditions were maintained for each scan. Figure 104 shows the results obtained for the same sample before cycling, at 15000 cycles and 17 000 cycles. At this stage acoustic emission have been recorded but no sign of delamination is found yet. This is confirmed by the amplitude C-scan (left side in figure 104) that shows no clear discontinuities or high increase in attenuation at the three fatigue stages. On the right hand side in figure 104, Harmonic Imaging shows an increase of the nonlinear parameter (amplitude of the first harmonic normalized by the fundamental) with fatigue cycling. The 17 000 cycles Harmonic image shows high harmonic generation near the edges of the sample. Variations from 0.1 to 0.3 for the non-linear parameter are recorded over the sample area (i.e. a 300% relative contrast).

After 17000 cycles, fatigue cycling was terminated and the sample was cut and polished in two cross-sections along the length of the sample. Microdelaminations mainly near the edge and matrix cracks in the center of the sample were clearly observed with an optical microscope. Figure 105 shows two micrographs of typical damage found in sample. Microdelaminations were running mainly between the +90 and +45 plies, up to 20 mm long and 10 μ m to 20 μ m open. Matrix cracks were found in the outer layers as expected with bending loads. Crack opening is also estimated between 10 and 20 μ m. A good correlation between regions with high crack density and high nonlinearities was found.

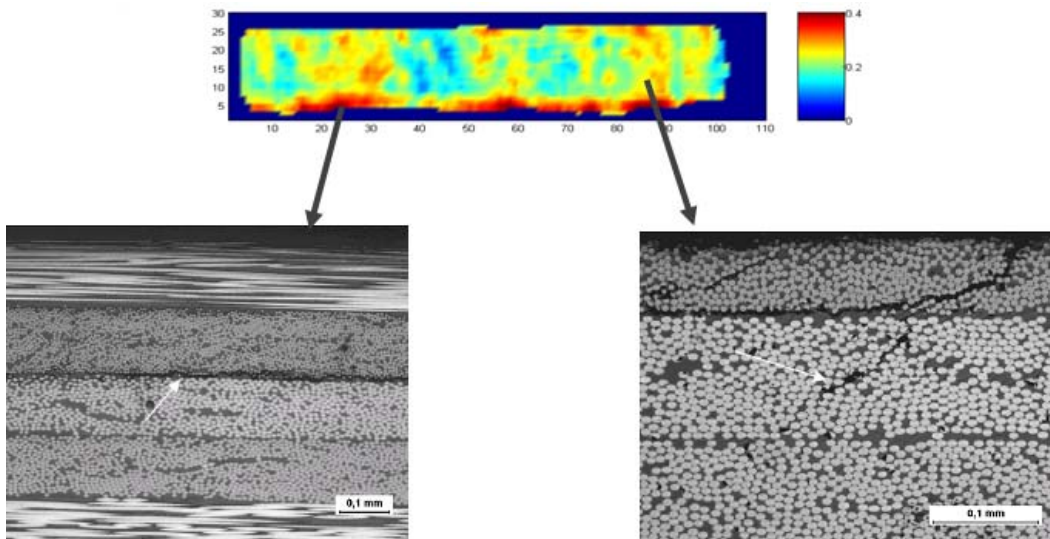


Figure 105: Micrographs of fatigue damage in CFRP laminate in areas with high nonlinear parameter

Nonlinearity in adhesive bonds

A similar imaging technique was used for the evaluation of nonlinearity in aluminium adhesive bonds. The objective was to investigate if a correlation between ultrasonic nonlinearity and shear strength could be established. Samples were manufactured using Cytec FM73 adhesive film and tested according to SAAB standard [5]. In order to affect shear strength, the samples were contaminated using a dry layer of silicone between the adherent and the adhesive reducing the adhesion strength in proportion with the quantity of silicone introduced. Figure 106 shows the failure surface for a sample without contamination (cohesive failure) and a highly contaminated sample (adhesive failure). The nonlinear parameter was imaged for seven samples with varying levels of contamination. Figure 107 shows the scan images representing the variation of the nonlinear parameter over the bond area. The samples were then mechanically tested and the bond strength were determined. An averaged nonlinear parameter was calculated from the scans for each bondline and figure 108 shows the correlation between mechanically determined bond strength and averaged nonlinear parameter. A clear increase of the non linear parameter was observed for the bond with lower strength.

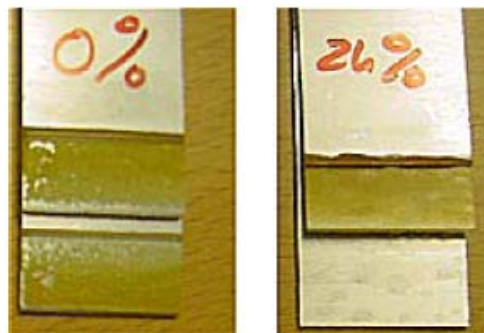


Figure 106: Failure surface of pristine bond (left) and silicon contaminated bond (right) in shear lap samples

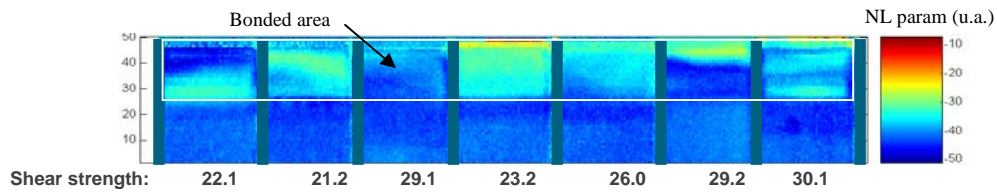


Figure 107: Harmonic imaging of seven samples with different contamination level and their respective strength measured from mechanical testing after nonlinear imaging scanning

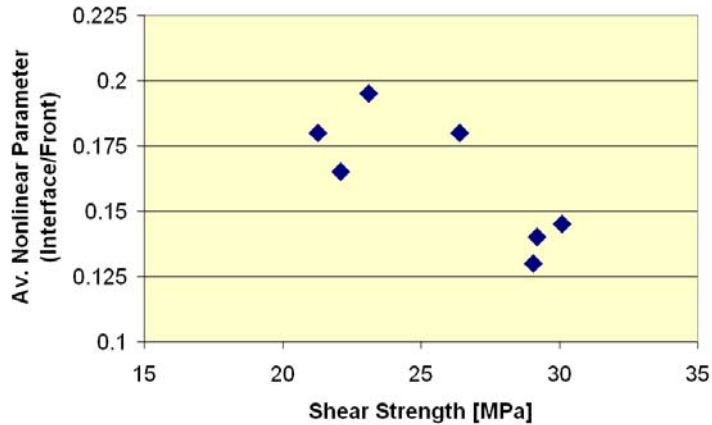


Figure 108: Normalised nonlinear parameter extracted from harmonic imaging scans as a function of shear strength.

Potential use of the nonlinear techniques for field inspections.

The results obtained on both composite laminates and adhesive bonds lead to the investigation of the feasibility of using the nonlinear effect for the characterization aerospace structure. Inspection procedures for field inspection require the development of dedicated portable equipment, robust measurement scheme and reference samples in order to be qualified as a potential tool for field inspection. Several approaches were investigated during the EU FP6 AERONEWS project [22] in which EXOVA took an active part and some encouraging results were obtained on metallic and composite structures. However two main limitations of the technique were identified:

- Although nonlinear techniques show a very high sensitivity to early damage, the amplitude of the effect is quite low and requires thorough calibration procedures in order to evaluate all potential sources of nonlinearity. As such intrinsic nonlinearity of the sensors and electronic should be carefully determined and checked. In particular the nonlinearity of the mechanical contact between the probe and the object under investigation is difficult to control and is in our opinion the main limitation for using existing manual inspection procedure.
- The origin and characteristics of damage induced nonlinearity is dependent on the material and on type of degradation mechanism at stakes. As the origin of damage induced nonlinearity is taking place at the meso-scale, it is often very difficult to manufacture reference samples that can be used to calibrate a procedure. No equivalent of the Flat Bottom Hole (FBH) commonly used in the NDT community exists yet for nonlinear techniques.

Alternatively, nonlinear techniques have shown to be very useable in the context of Structural Health Monitoring where the system is monitoring the variations in time of a structure under loading. SHM systems, if stable in time, take advantage of the time evolution of the structure under investigation and do not depend as strongly as classical NDT on reference samples.

3.7 SERVICE LOADS MONITORING

3.7.1 Service life monitoring of Gripen weapon pylons

Weapon pylons are life limited parts of the aircraft system and can be switched between different aircraft. In order to optimize the use of these pylons, a life monitoring procedure has been developed. The procedure includes the calculation of the true loading of the critical areas depending on actual flight manoeuvres and store loads. Also the aerodynamic induced interactions between stores on adjacent pylons are included. The loads model makes use of flight parameters recorded during flight and on other configuration parameters and are mainly based on wind tunnel test results. In figure 109 is the loads model schematically described. The load sequence generated from this model is subsequently handled in the same way as other airframe load sequences included in the Gripen life monitoring system i.e. identification of rain-flow cycles and fatigue severity calculation for the mission considered.

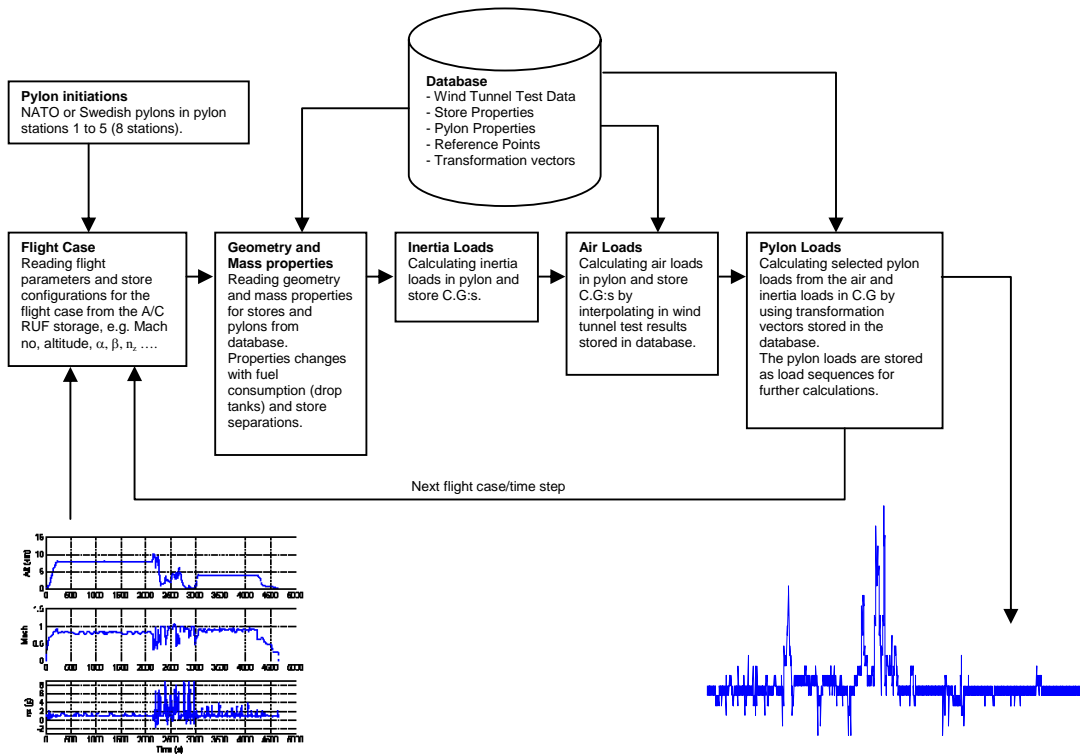


Figure 109. The principles for weapon pylon loads calculations in the service life monitoring system

The fatigue significant load components defined for the fuselage mounted pylon 5 shown as an example in figure 110. All selected significant loads follow the individual pylon through its operational life. The fatigue consumption and remaining life (or time to maintenance action) for the specific pylon is governed by the load component with the shortest remaining life.

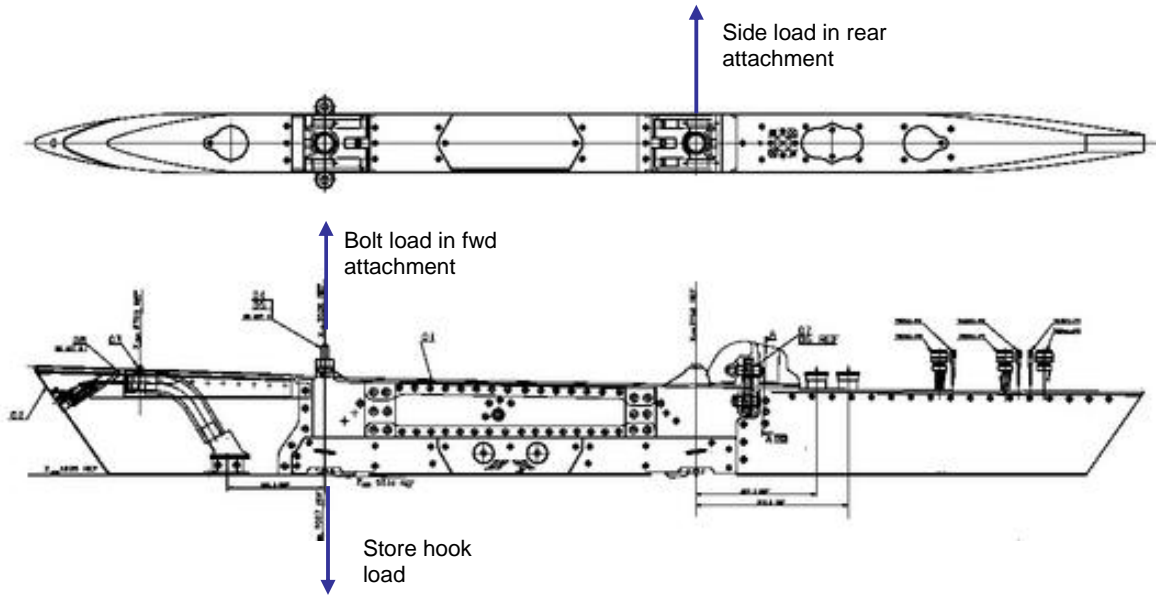


Figure 110. Example of selected load components for fuselage pylon no 5.

REFERENCES

- [1] ICAF Doc.No 2411. A review of aeronautical fatigue investigations in Sweden during the period June 2005 to April 2007. Edited by Ansell, H. Presented at the 30th Conference of the International Committee on Aeronautical Fatigue (ICAF), Naples, Italy, 14-15 May 2007.
- [2] ICAF Doc.No 2419. A review of aeronautical fatigue investigations in Sweden during the period May 2007 to April 2009. Edited by Ansell, H. Presented at the 31th Conference of the International Committee on Aeronautical Fatigue (ICAF), Rotterdam, The Netherlands, 24-25 May 2009.
- [3] SHK Report RL 2010:01e. Accident to aircraft SE-IVF at the northern basin of Falsterbo canal, Skåne County, on 26 October 2006. Case L-27/06. February 22, 2010. The report is available on web site: www.havkom.se
- [4] B. Andersson, A.F. Blom, U. Falk, G.S. Wang, K.Koski, A. Siljander, J. Linna, A. Miettinen, K Vaaraniemi and R Lahtinen, "A Case Study of Multiple-Site Fatigue Crack Growth in the F18 Hornet Bulkhead", 25'th ICAF Symposium-Rotterdam, May 27-29, 2009, pp 707-741
- [5] Andersson B, Falk U, Babuska I and Petersdorff T v, "Reliable stress and fracture mechanics analysis of complex components using a *hp*-version of FEM", Int. J. Num. Meth. Eng., Vol 38, 1995, pp 2135-2163
- [6] Babuska I., Andersson B., "The Splitting method as a tool for multiple damage analysis", SIAM J Sci Comp, Vol 26, No 4, 2003, pp 1114-1145
- [7] Fawaz, S. A. and Börje Andersson. "Accurate Stress Intensity Factor Solutions for Corner Cracks at a Hole." Engineering Fracture Mechanics 71 (2004):1235-1254.
- [8] Y. Murakami et al., "Stress Intensity Factors Handbook", Volume 2, Pergamon Press, 1987, pp 641-1454
- [9] G.S. Wang," Probabilistic Fatigue Crack Growth Analysis for Critical Structural Details", AIAA Journal, Vol. 38, No. 5, pp 882-892, May 2000
- [10] G. S. Wang, "Response modelling of materials at high temperature", EU FP6, Contract No. AST5-CT-2006-03072, ATLLAS, Deliverable D5.4.1, 2009.
- [11] M. Dalenbring, G. S. Wang, and H. Rabia, "Dynamic Stress and Strain Analysis at High Temperatures", EU FP6, Contract No. AST5-CT-2006-03072, ATLLAS, Deliverable D5.4.3, 2009.
- [12] D. Gustafsson. "Constitutive and Fatigue Crack Propagation Behaviour of Inconel 718". Linköping Studies in Science and Technology, Thesis No. 1461. LIU-TEK-LIC-2011:1 December 2010.
- [13] Camanho, P. P., and C. G. Davila, "Mixed-Mode Decohesion Finite Elements for the Simulation of Delamination in Composite Materials," NASA/TM-2002-211737, pp. 1-37, 2002.
- [14] Benzeggagh, M. L., and M. Kenane, "Measurement of Mixed-Mode Delamination Fracture Toughness of Unidirectional Glass/Epoxy Composites with Mixed-Mode Bending Apparatus," Composites Science and Technology, vol. 56, pp. 439-449, 1996.
- [15] Marklund E. Literature survey of 3D failure criteria. TR10-002. Swerea SICOMP, 2010.
- [16] Olsson R. A survey of test methods for multiaxial and out-of-plane strength of composite laminates Composites Science and Technology 2011; <http://dx.doi.org/10.1016/j.compscitech.2011.01.022>.
- [17] Universality of Nonclassical Nonlinearity. Applications to Non-destructive Evaluations and Ultrasonics. Delsanto Pier Paolo (Ed.), Springer, New-York, 2006.
- [18] Quantification of Fatigue using Nonlinear Ultrasound Measurements, V. Kommareddy et al., proceedings of the European conference on NDT, 2006.
- [19] Fatigue damage Assesment by nonlinear ultrasonic materials characterization, P. B. Nagy, Ultrasonics 36, 375-381, 1998.

- [20] Impact damage detection in composite laminates using nonlinear acoustics, F Aymerich et al., Composites: part A, (2010) 1084-1092.
- [21] Saab-Scania Standard STD 2694, based on AECMA prEN 2243-1, ed 1 August 1980. "Test methods structural adhesives single lap shear".
- [22] Health monitoring of aircraft by Nonlinear Elastic Wave Spectroscopy, AERONEWS, EC FP6, SPECIFIC TARGETED RESEARCH: AST-CT-2003-502927

ACKNOWLEDGEMENTS

This work was supported by Saab AB. The editor is also indebted to the following individuals who helped to write this review:

Börje Andersson	FOI	(Section: 3.4.1, 3.4.3)
Anders Bredberg	SAAB AB	(Section: 3.5.1, 3.5.2)
Göran Carlsson	SAAB AB	(Section: 3.3.1, 3.3.2, 3.3.3)
David Gustafsson	LiU	(Section: 3.4.7)
Zlatan Kapidzic	SAAB AB	(Section: 3.3.9)
Christophe Mattei	Exova AB	(Section: 3.6.1)
Sören Nilsson	Swerea SICOMP	(Section: 3.5.3)
Robin Olsson	Swerea SICOMP	(Section: 3.5.4)
Göran Rosvall	SHK	(Section: 3.2.1)
Joakin Schön	FOI	(Section: 3.5.1, 3.5.2)
Stefan Thuresson	SAAB AB	(Section: 3.2.2, 3.2.3, 3.3.1, 3.3.2, 3.3.3)
Geng-Sheng Wang	FOI	(Section: 3.4.2, 3.4.4, 3.4.5, 3.4.6)
Urban Wendt	SAAB AB	(Section: 3.3.7, 3.3.8)
Lars Östling	SAAB AB	(Section: 3.7.1)